UNIVERSITY OF SOUTHAMPTON

Vortex Shedding Analysis and Control Using Reduced Order Modelling and Viscous Cell Boundary Element Method

by Ravi Arkalgud

A thesis submitted for the degree of
Doctor of Philosophy

FACULTY OF ENGINEERING AND APPLIED SCIENCE
SCHOOL OF ENGINEERING SCIENCES
SHIP SCIENCE

2002

UNIVERSITY OF SOUTHAMPTON

ABSTRACT

FACULTY OF ENGINEERING AND APPLIED SCIENCE
SCHOOL OF ENGINEERING SCIENCES, SHIP SCIENCE

Doctor of Philosophy

Vortex Shedding Analysis and Control Using Reduced Order Modelling and Viscous Cell Boundary Element Method

by Ravi Arkalgud

The simulation and control of vortex shedding patterns are discussed using a viscous cell boundary element method, a proper orthogonal decomposition method, reduced order model techniques and trust-region framework modelling.

Vortex shedding characteristics are investigated numerically for steady flow past two stationary cylinders of equal diameter at a critical gap spacing of 0.9 to 1.10, in increments of 0.05 and the analysis is extended to the study of flows around rotating cylinders.

The Viscous Cell Boundary Element Method (VCBEM) developed by Tan et al. (1999) is modified to incorporate the study of rotating cylinder problems and this has proved successful in reproducing the detailed flow characteristics of experimental observations, correlation with theoretical predictions produced by other methods and experimental measurements of drag and lift coefficients over a range of Reynolds number. This has been achieved through a primitive variable formulation of the hybrid approach involving boundary element and finite element methods. The fluid domain is idealised by an unstructured mesh and the relevant boundary conditions for the rotating cylinder incorporated into the VCBEM code through development of suitable numerical schemes of study. Numerical predictions are presented for flow patterns involving different arrangements of twin rotating cylinders and the simulation results are discussed.

A brief overview is presented describing reduced order modelling techniques applicable to Navier-Stokes equations with particular focus on the proper orthogonal decomposition technique and its application to rotating cylinders. A control function approach is formulated for this class of problems and validation studies are conducted.

Trust-region augmented reduced order modelling techniques are adopted for optimal control of vortex shedding in the wake of a cylinder by imposing a time dependent angular velocity on the cylinder. The application of these techniques to design feedforward and feedback controllers is examined to achieve vortex suppression.

I would like to dedicate this work to

My Mother *The First Teacher*,

My Father *The Best Friend* and

The affectionate Sister *Avayya*.

Contents

List of Figures

List of Tables

Nomenclature

$(')$	Dimensional quantity
Ω	Spatial domain
Σ	Boundary of the spatial domain
D	Diameter of the cylinder
C_d	Drag coefficient
C_l	Lift coefficient
R_e	Reynolds number
$\mathbf{v}$	Velocity vector
$\mathbf{R}$	Traction vector
p	Pressure
v^*_{sj}, R^*_{sj}	Fundamental solution
g^*	Gap width between cylinders
γ	Rate of rotation
ϕ	Global basis vector
y	Time dependent amplitude vector
λ	Eigenvalue
h	Semi-width of the computational domain
$\mathbf{n}$	Unit normal vector
u_i	Velocity component
$\overline{u_i}$	Average velocity component
δ_{ij}	Kronecker delta function
ν	Kinematic viscosity
μ	Dynamic viscosity
ξ	Field point
ρ	Density
τ	Shear stress
$\tau_1, \tau_2, \tau_3, \tau_4$	Boundary conditions on the computational domain

τ_c	Boundary condition on the cylinder under rotation
∇	Gradient operator
$c_k(t)$	Control input
$f(c_k)$	Full order cost function
$m(c_k)$	Reduced order cost function

Acknowledgement

I would like to thank my supervisors Prof.W.G.Price and Dr.M.Tan for their constant support. I would like to thank Prof. Price for his patience and trust in me and timely discussions with Dr.M.Tan are very much appreciated. I am thankful for the valuable suggestions provided by Dr.M.J.Downie and Prof.E.Rogers in regard to the thesis.

I do thank Dr.P.B.Nair for being my collaborator and for his advice in control aspects. The long nights of discussion are cherished.The constant love and support from my family is always cherished.

Thanks to Dr.W.M.J.Batten for his support as a friend and his destructive comments leading for destructive/constructive works, a definite paradox which time only could answer. I would like to thank R.Pattenden for his concrete silent support and valuable discussions all the way.

Now I should thank Dr.I.G.Williamson for his friendship and support. Ian has enriched my knowledge as friend in lots of different ways in the areas of Theology, Philosophy and from Pre-natal to Post mortem of realtionships (sexual). My friend Elli's moral lessons are always cherished but never implemented. I thank her for her sincere effort to teach morals, which never exist as I see.

I would like to thank Dept. of Ship Science and CEDC for their co-operation during the tenure. Special thanks to Dr.Neil Bressloff for all the support and co-operation he extended during my studies. I would also like to thank Momadu, Ajay, Sachin, Berney, Patrick, Jomac, for their company and for my office mates who took the absolute risk of making me a football player. Result being obvious an absolute disaster. I appreciate the guts of CEDG-Eagles.

Finally, I would like to thank my friends Helen for her light heart comments (She's Blondie), Yelena, Sofia, Signe for deep psychological analysis (who ended in a autospin) and Noel for his destructive influence, which strangely had a creative effect on me.

I would especially like to thank Elisabete Garcia for her support and affection during the most needy times. I thank one and all who have been a part in my PhD.

Chapter 1

Introduction

1.1 A Brief Overview of Computational Fluid Dynamics (CFD)

Computational Fluid Dynamics (CFD) provides a good example of the many areas that a scientific computing project can touch on. Fluid flows are modelled by a set of partial differential equations, the Navier-Stokes equations and no closed-form solutions exist except for special cases. This fact was one of the motivations for the development of computational techniques.

Solving a particular problem using CFD model generally involves first discretizing the physical domain in which the flow occurs, such as the interior of a turbine engine or the radiator system of a car. This discretization is straightforward for very simple geometries such as rectangles or circles but it is a difficult problem for more complicated objects. Currently automatic 'mesh generators' are simply not adequate for arbitrary shapes, requiring extensive investment of time on the part of the scientist or engineer. This leads to problems in human-computer interfaces (HCI), as well as fundamental problems in graph theory, since the resulting discretization produces a mesh that is best dealt with as a graph as discussed by Kesselmann (1999), Bramley et al. (2000)

On the discretized mesh the Navier-Stokes equations take the form of a large system of nonlinear equations. Transferring from the continuum to the discrete set of equations is a problem that combines both understanding the mechanisms of the physical flow and numerical analysis. For example, it is important to maintain conservation of mass in the discrete equations. To each node in the mesh are associated very many variables such as pressure, three velocity components, density, temperature, etc. Gresho et al. (1980), Zienkiewicz et al. (1990), John (1995), Versteeg & Malalasekera (1998), Kesselmann (1999) to name but a few, have discussed in detail the implementa-

tion and incorporation of the degrees of freedom and the involved mesh discretization techniques and procedures. Furthermore, capturing physically important phenomena such as turbulence requires extremely fine meshes in regions of the physical domain. Currently meshes with 20 000 to 2 000 000 nodes are common, leading to systems with up to 40 000 000 unknowns (Kesselmann, 1999, Dutto et al., 1997).

The system of nonlinear equations is typically solved by an iterative method, which in turn requires solving a large, sparse system of equations at each step. Sparsity here means that the matrix of coefficients for the linear system consists mainly of zeros, with only a few nonzero entries. With 4×10^7 unknowns, clearly we cannot store the matrix as a 2D array with 16×10^{14} entries!. To store the coefficients needs development of efficient data structures which require little overhead storage but allow the necessary manipulations to be performed efficiently (Dutto et al., 1997).

Methods to solve large sparse systems of equations were always at the forefront of mathematics or computer science, since they are often the most time-consuming part of the program, and because the ability to solve them is often the principal limiting factor in the size of problem and complexity of the physics that can be handled (Chang & Song, 1990). Direct methods, which factor the matrices, require more computer storage than is permissible for all but small problems, hence limiting the application. Iterative methods use less storage but suffer from a lack of robustness: they often fail to converge. The solution is to premultiply the linear system by some matrix that makes it easier for the iterative method to converge (Bramley & Sameh, 1992, Meijerink & Van der Vorst, 1977, Dutto et al., 1997).

CFD problems are at the limits of computational power, so parallel programming methods are used. This introduces the research problem of how to partition the data to assign parts of it to different processors; usually domain decomposition methods are applied. Domain decomposition is often expressed as a graph partitioning problem, with roughly the same number of nodes in each partition set. An additional problem with parallel programming is that the better methods to solve the resultant linear systems often have inherently sequential characteristics, while parallel solution methods are not robust enough to tackle real world problems (Dutto et al., 1997, Kesselmann, 1999, Bramley et al., 2000).

Once the solution is found, analyzing, validating, and presenting the results calls into play visualization and graphic techniques. These techniques are useful for more than just viewing the computed flow field. Visualization can help with understanding the nature of the problem, the interaction of algorithms with the computer architecture, performance analysis of the code, and, most importantly, debugging!

This discussion of CFD indicates where computer science and mathematics come

into play: graph theory and algorithms, numerical analysis, parallel programming, graphics and visualization are all needed here.

The evolution of fluid dynamics dates back through past centuries. The foundations of experimental fluid dynamics have their origin in the 17th century. The 18th and 19th centuries saw the development of theoretical fluid dynamics. The historical perception of the evolution of fluid dynamics is presented in the works of Rouse et al. (1957), Tokaty & Foulis (1971), Kothari & Anderson Jr (1985). As a by-product of these developments, the 20th century saw fields of fluid dynamics through the growing maturity of, pure theoretical and pure experimental approaches.

CFD has a new *'third approach'* in the philosophical study and development of the whole discipline of fluid dynamics (John, 1995). CFD is a judicious blend of the two discrete approaches i.e pure theoretical and pure experimental. It synergistically complements the two approaches of fluid dynamics. CFD is the analysis of systems by means of computer simulation involving fluid flow, heat transfer and associated phenomena such as chemical reactions (Versteeg & Malalasekera, 1998).

CFD is used as a research tool to enhance the knowledge of physical phenomena and it is also used to interpret experimental data. The numerical experiments conducted by Kothari & Anderson Jr (1985) on the Wortmann airfoil for subsonic compressible flow helped to elucidate physical aspects of the flow field for the flow regime of $R_e = 10^5$. The numerical experiments showed a flow separation over both top and bottom surfaces of the airfoil with the turbulence model switched off, even though the angle of attack was zero. The investigation, comparing the wind tunnel observation with CFD results, concluded that flow over an airfoil in the wind tunnel experiment was turbulent as discussed by Kothari & Anderson Jr (1985), Pohlen & Mueller (1986). The advent of modern computers have enabled CFD to become an industrial tool in the analysis and design of structures. Using a finite volume explicit numerical scheme developed by Jameson et al. (1981), Bush et al. (1986) provided the detailed flow field and pressure distribution around a high-speed aircraft such as a Northrop F-20. This is of great value to engineers in designing the structure of the airframe to withstand expected aerodynamic loads.

A typical CFD code has three components such as preprocessor, solver and post processor. Preprocessor provides input to the flow problem, which is solved using various numerical schemes in the Solver and the output of solver is processed by the Post processor for presentation and graphic visualization. Post processors play a key role in communicating the large volume of CFD data and help to derive a physical interpretation of the processed data (Versteeg & Malalasekera, 1998)

1.2 Applications of CFD

CFD has a wide range of applications and is a multi-disciplinary activity in engineering and science (Bewley, 2001). Modern CFD cuts across all disciplines where the flow of a fluid is important (John, 1995). The applications include, aerospace engineering (Jameson et al., 1981, Kothari & Anderson Jr, 1985, Pohlen & Mueller, 1986, Bush et al., 1986, John, 1995), automobile design (Shaw, 1988, Matsunaga et al., 1992) and internal combustion engine applications (Griffin et al., 1978), casting techniques (Mampaey & Xu, 1992), manufacture of ceramic composite materials (Steijsiger et al., 1992), dredging operations (Toorman & Berlamont, 1992), air currents in buildings (Alamdari et al., 1991) etc.

CFD is a major tool in solving aerodynamic, hydrodynamic and fluid-structure interaction problems. It has its applications in marine engineering and naval architecture. CFD is used in the analysis and design of underwater structures, offshore platforms, ships, submarines etc. The varied applications of CFD are discussed in detail by many authors, for example, John (1995), Gad-el Hak (1996), Bramley et al. (2000), Versteeg & Malalasekera (1998) etc. to name but a few.

This thesis looks into the application of CFD as a research tool, investigating one of the many cases of fluid-structure interaction problems involving underwater structures.

1.3 Problem of Interest

The analysis and design of marine structures continues to be an interesting and challenging area of research. It is of prime importance to evaluate and predict fluid forces, structure and fluid interactions and the resulting responses of the fluid and the body. The fluid and body obey their respective laws of motion when analyzed separately, but the fluid-structure interaction causes significant changes in their behaviour. Such complex phenomena involve flow separation, vortex shedding, turbulence etc. which are explained by Duncan et al. (1970) in mechanics of fluids, Batchelor (1971) in describing principles of fluid dynamics, Barltrop & Adams (1991) for the dynamics of marine structures etc. Currently, the complete prediction of these phenomena is not practically feasible because of computational limitations (Homescu et al., 2002). Reduced order modelling technique based on proper orthogonal decomposition has been proposed and developed to analyse the structure and their interactions with the fluid, see for example, Deane et al. (1991), Berkooz et al. (1993), Dowell (1995), Graham et al. (1999), to name but a few.

In order to simplify the analysis the fluid is assumed isothermal, incompressible,

homogeneous and Newtonian. Even with these simplifications, the prediction of fluid behaviour is complicated, for the flows encountered range from low to high Reynolds number and the arbitrary shaped bodies can have low or high aspect ratios (eg. hydroplanes on submarine) or bluff, as in tubular structure of an off-shore platform (Morison et al., 1950, Sarpkaya & Isaacson, 1990, Hatton, 1999).

This domain of fluid problems is well beyond the established theoretical techniques of potential flow or boundary layer flow because these flows involve viscous phenomena such as separation, vortex shedding and turbulence. To overcome these theoretical difficulties experimental and empirical approaches were the only means to develop design procedures (Morison et al., 1950). For most practical cases, where gravity and unsteady effects are negligible, nondimensional Reynolds and Mach numbers need to be matched to consider two different flows to be similar. For many flows nondimensionalization of the Navier-Stokes equation leaves the Reynolds number as the only independent parameter involved. Equivalent results can be partially derived from experiments by using scaled models, when the body shape is known. Such experiments are of great value in design but most flows do require several dimensionless parameters for their specification and it is difficult to achieve in experimental studies. A possible implementation of the scaling principle is seen in water or wind-tunnel testing where the model scale differs from the actual flow conditions. For example, the testing of airplanes at a smaller scale (e.g.,1/5-th scale), results in increasing the airspeed or air density (e.g., by a factor of 5) to maintain the same Reynolds number. The increase in airspeed results in unreasonably high Mach number and the other alternative of reducing the kinematic viscosity ν by compressing the air is applicable only in a few wind tunnels (Josesh & Allen, 2001). Hence, in most cases matching both nondimensional Reynolds and Mach numbers is difficult if not impossible. The other possibility of changing of fluids in test conditions to scale the models are used in wind tunnel experiments of submarines. The kinematic viscosity ratio of 1:15 for water to air is used to develop a 1/15th-scale submarine model to test in a wind tunnel at true speed conditions (Josesh & Allen, 2001).

Booth & Bishop (1973) discuss the use of a planar motion mechanisms to determine experimentally slow motion manoeuvring derivatives associated with a submarine operating in a viscous fluid. Empirical approaches allow predictions of responses as in the case of vortex induced vibration occurring in oscillatory systems (see, for example, Blevins (1990)) or Morrison equation in the design of offshore structures (Morison et al., 1950).

The report of Sainsbury & King (1971) on building an oil terminal jetty from steel piles which was fraught with difficulties during the construction phase, gives us some

insight to the problems faced in marine construction.

During the construction phase, newly driven piles experienced a tidal current of 5 knots which resulted in vortex shedding of the piles and because of the low natural frequency of the submerged structures the phenomenon known as 'lock-in' was observed. Piles of great lengths broke at the sea bed unless restrained during construction. This vortex induced vibration affected any group of piles which were cantilevered to the flow. Strut stiffening was one of the practical solutions adopted to rectify the problem in the low tide case before evaluations were carried out for forces and the effect of currents on the new stiffened braces.

Research was initiated to give further insights to the problem. There were concerns about lock-in phenomenon even at low frequencies when concrete decks were placed on the piles to carry oil flow in pipelines. The project continued with all encountered difficulties and various problems were successfully sorted out. The difficulties faced during the construction are detailed in the study of Farrant (1998) into the dynamic interactive behaviour between groups of circular cylinders and viscous flows. Both Morison et al. (1950) and Sainsbury & King (1971) reported that their analysis was based on a single pile in isolation and considerable changes in dynamic behaviour are observed when pile groups or bracings are involved.

To assess the practical aspects of the real life problem as reported by Sainsbury & King (1971), the problem is simplified and idealized by examining through simulations of the dynamic behaviour of groups of cylinders. The current research is focused on the analysis and simulation of vortex shedding patterns from various arrangements of cylinders and the development of flow control strategies when imposed rotations are applied to the cylinders. A reduced order model is developed to analyse the system incorporating active control strategies and techniques to suppress the vortex shedding phenomena for a given Reynolds number flow range.

1.4 Numerical Methods in Fluid Flow Analysis

Closed form solutions to real engineering problems are not usually available except for simple systems. Nonlinearity in the system and arbitrary geometry are major impediments to derive analytical solutions. The advent of high speed computers has provided the means to solve problems using discrete numerical models consistent with continuous systems (Bramley et al., 2000). A number of distinct numerical methods have been developed containing a fully fledged framework of analysis and coding procedures. Some of the principal techniques are as follows:

- Finite difference method

- Finite volume method
- Finite element method (FEM)
- Boundary element method (BEM)

A general introduction to the Boundary Element Method (BEM) is described by Brebbia (1978), Brebbia & Walker (1980a,b) and a review of the other three, called 'domain methods' is given by Hirsch (1988).

The finite difference method was the first to appear with derivatives in the governing equations replaced by incremental differences using Taylor series expansions. This has a limitation in dealing with a complex geometry because of the division of the domain into a block structure.

The Finite Volume Method has evolved from the finite difference method. The formulation is based on finite control volumes in the integration of the governing equations. There are two forms of finite volume method as discussed by Hirsch (1988). That is,

- The structured mesh form has great similarity to the finite difference method and uses a block structure approach to mesh generation. Each block should have a quadrilateral topology when applied to a two-dimensional problem and a hexahedral topology in a three-dimensional problem.
- The unstructured form has the advantage of flexible mesh generation but has complications in aspects of coding.

The Finite Element Method (FEM) was developed by Argyris & Scharpf (1969) and Zienkiewicz (1977) to solve structural analysis problems and in general is used to solve field equations describing continuous media. FEM is widely used and perhaps the most able one to cope with arbitrary boundaries. Gresho et al. (1980) applied FEM in an incompressible viscous flow analysis. Later FEM was applied by Zienkiewicz et al. (1990), who developed an algorithm for compressible and incompressible fluid flow problems.

In FEM, the integral equation is formulated using the method of weighted residuals. The integral equation is then transformed to a set of algebraic equations by incorporating weighting functions and interpolation functions. The Galerkin method (Van de Vosse et al., 1986, Hirsch, 1988, Li et al., 1991) is a popular form of FEM used in fluid flow analysis and its main disadvantage lies in the computational cost to solve simultaneous equations having large bandwidth (Chang & Song, 1990). These three methods are classified as domain methods, in which the entire domain is discretized.

The Boundary Element Method (BEM) originates from the formation of a weighted residual integral equation, incorporating the linear differential equation to be solved (Brebbia, 1978, Brebbia & Walker, 1980a,b). The integral equation is integrated by parts to eliminate unknown derivatives from the original equation. This results in the differentiation of the weighting function. The selection of the impulse response function of the system as the weighting function (i.e. a fundamental solution) results in an expression involving boundary integrals only. This is achieved because of the analytical integration of the domain integral and the remaining equation is discretized to form a set of algebraic equations whose coefficients are determined by boundary integration. The advantage of this method lies in the reduction of dimensionality of the problem.

The extension of Boundary Element Method (BEM) to non-linear problems is a complicated mathematical process. Tosaka & Kakuda (1988) proposed a subdomain (cell) approach. The non-linear governing differential equation is linearized in the cell by applying BEM and the global domain is assembled using continuity equations valid in the subdomain. This subdomain form of BEM is referred to as a Cell BEM and details of the mathematical formulation are explained in the Chapter 2 of this thesis.

1.5 Reduction Methods and Flow Control

The development of efficient numerical schemes for optimal flow control is a topic that has attracted much attention in recent years. One major challenge in this area arises from the fact that, in practice, computationally expensive high-fidelity models are required to analyze the behaviour of controlled flows (Homescu et al., 2002). To overcome the computational obstacles to flow control, the idea of constructing computationally effective reduced order models has been pursued in many recent studies; see, for example, Deane et al. (1991), Ravindran & Ito (1998), Tan et al. (2000).

A popular model reduction technique which has been applied with some degree of success is the proper orthogonal decomposition (POD) method discussed by Sirovich (1987), Berkooz et al. (1993), Ravindran (1999). The reduced order models based on proper orthogonal decomposition approach are developed and used in lieu to computationally expensive high-fidelity models. On applying the proper orthogonal decomposition method to flow field data, dominant energy-containing structures can be extracted. A reduced order model (ROM), can then be constructed using these structures as basis functions.

Sirovich (1987), Deane et al. (1991), Berkooz et al. (1993), Graham et al. (1999) and many other researchers have applied proper orthogonal decomposition to fluid problems to investigate the behaviour of coherent structures in fluid flows. The reduced order model is constructed using basis functions computed by proper orthogonal decomposition, applied to the flow-field snapshots predicted by the full-order Navier Stokes (NS) equations for a baseline control input. Dominant structures contain most of the energy in the flow and therefore a limited number of dominant coherent structures are used in the proper orthogonal decomposition model construction. A proper orthogonal decomposition model based on a particular *baseline control input* might be ineffective when driven from the original state to an optimal state owing to the effects of control spillover which can potentially make the higher modes unstable. One way to circumvent control spillover is to interleave the full-order Navier-Stokes equations and the reduced order model during the optimization process.

Alexandrov et al. (1997) proposed a globally convergent trust-region framework to interleave exact and approximate objective function models in numerical optimization. The trust-region framework can be interpreted as an adaptive method to monitor a measure of optimization of the approximate model and by comparing the approximate model prediction with an exact value periodically, the information relating to accuracy of the reduced order model is obtained. This information can then be employed to decide the move limits (i.e. adaptive radius of trust region) to be enforced in the next

optimization iteration, as well to update the approximation model. More recently, Arian et al. (2000) showed that under some mild assumptions on the accuracy of the reduced order model, convergence to the high-fidelity optimal solution can be guaranteed. Recently, the trust region framework interleaving exact and approximate models has been successfully implemented for the suppression of vortex flow as discussed by Ravi et al. (2002).

1.6 Outline of Thesis

The simulation and control of vortex shedding patterns behind cylinders in a viscous fluid flow are described in this thesis using a viscous cell boundary element method and reduced order model techniques. Tan et al. (1999) developed a cell viscous boundary element method (VCBEM) to solve Navier-Stokes fluid flow problems and this has proved very successful in solving fluid-structure interaction problems involving multi-body configurations as discussed by Farrant (1998), Farrant et al. (2000, 2001) and Uzunoglu et al. (2001). The numerical scheme of study described is a hybrid approach combining boundary element and finite element methods. The boundary element is applied to fluid cells idealizing the fluid domain through an unstructured mesh and global equations are derived adopting finite element procedures.

Chapter 1 looks at CFD as a research tool to solve problems of fluid mechanics and poses practical aspects of a real life problem as reported by Sainsbury & King (1971) namely, the building of an oil terminal jetty from steel cylindrical piles which was fraught with many fluid-structure interaction difficulties during the construction phase. The problem is simplified and idealized by examining through simulations of the flow around cylinders.

A Viscous Cell Boundary Element Method (VCBEM) is applied as a CFD tool to investigate incompressible viscous, flow past two parallel stationary cylinders of equal diameter at a critical gap spacing g^* =0.90 to 1.10. At this critical gap, vortex patterns show dependence on the spacing factor which also relates to the interaction mechanism and vortex shedding frequency. Simulations of the flow past the two cylinders by using VCBEM are analyzed in Chapter 2. In this critical flow zone an interchange of in-phase and anti-phase wake flows is observed in an irregular manner. The switching mechanism between the states is investigated. Probability and power spectral analyses are presented to illustrate the statistical characteristics of the drag and lift flow parameters and vortex shedding patterns assessed through examination of their frequencies (Ravi et al., Under review).

The analysis is extended to study flow around twin rotating cylinders of equal diam-

eter in Chapter 3. The Viscous Cell Boundary Element Method (VCBEM) developed by Tan et al. (1999) is modified herein to study rotating cylinder problems. This has proved successful in reproducing the detailed flow characteristics of experimental observations and theoretical predictions produced by other methods, over a range of Reynolds number. This success has been achieved through a primitive variable formulation of the hybrid approach involving boundary element and finite element methods. The fluid domain is idealized by an unstructured mesh and the relevant boundary conditions for the rotating cylinder are incorporated in the VCBEM code with the development of suitable numerical schemes of study. The presented computed unsteady flow simulations provide verification and validation of the proposed approach as measured against other theoretical findings and experimental observations. The confidence developed in the proposed VCBEM approach after validation studies has led to its extension to the study of twin cylinders in side-by-side or tandem formations. Time-dependent boundary conditions are implemented on the cylinder and integrated into the VCBEM code. The effects of key flow parameters, characteristics of drag and lift flow parameters and vortex shedding patterns are discussed.

In order to control the vortex shedding from the rotating cylinders reduced order models are developed which are amenable to the development of a control strategy. Reduced order models (ROM) are investigated and discussed in Chapter 4 by applying a proper orthogonal decomposition (POD) method and also the different methods for reduced order modelling applicable to the unsteady flow model are described. A proper orthogonal decomposition (POD) method is used to investigate the surrogate reduced order models (ROM) of the vortex shedding wake exhibited behind the rotating circular cylinders. The method is found to be very effective in deriving coherent structures of reduced order model to describe vortex shedding processes.

A control function method based on proper orthogonal decomposition was adopted for the analysis and a procedure developed to validate the reduced order model. This approach is used to develop an optimal control strategy of vortex shedding through adoption of trust-region augmented reduced-order modelling techniques as described in Chapter 5. The model problem under investigation involves suppressing Karman vortex shedding in the wake of a circular cylinder by imparting time-dependent angular velocity to the body. The application of trust-region methods integrated with reduced order models based on proper orthogonal decomposition is demonstrated through the design of feedforward and feedback controllers to achieve vortex suppression. In this chapter validation of the proposed trust region approach is carried out for the domain of applicability and different Reynolds number flow regimes. Chapter 5 also addresses aspects of control application for the wake of a circular cylinder with an overview of

flow control. A brief summary of objectives achieved and conclusions derived from current research are presented in Chapter 6 with the paradigm of future research.

Chapter 2

Analysis of Stationary Cylinders at Critical Gap Spacing

2.1 Introduction

Viscous fluid flows around cylinders exhibit a plethora of fluid mechanics phenomena including flow separation, vortex shedding, turbulence, etc. They are of significance in predicting the loads on structures subject to fluid motion as discussed by Hatton (1999) for the design of deep water floating oil production systems involving risers, tension leg platforms, fixed jacket structures, etc. For such configurations a two-dimensional analysis flow around cylinders is considered sufficient for the evaluation of the forces acting on these cylindrical offshore structures since the vertical component of velocity is neglected as discussed by Zhou & Graham (2000).

Vortex interactions with foils, blades or cylinders can result in significant changes in the velocity field, vortex shedding from the body surface and damage to the structure. For example, vortex shedding and interaction cause distortion to the local heat transfer mechanism as in the case of turbine blades. Rockwell (1998) reviews the challenging problems arising from the interaction of vortices in three-dimensional flow and the resultant local loading.

Direct Numerical Simulation (DNS) of the Navier-Stokes equations to analyze the vortex dynamics of fluid-structure interaction is limited to moderately low Reynolds number ($R_e < 10000$) unless sub-grid scale turbulence models are used as discussed by Cheng & Armfield (1994). This technique complements previous approaches to examine vortex shedding and wakes by Mair & Maull (1971), Bearman & Graham (1980), Ortel (1990), to name but a few.

In general, a shear layer in a flow is convectively unstable and pertubations intro-

duced by the presence of various bodies result in resonance when sustainable oscillations are reached as evidenced by Ortel (1990). The location of shedding frequency due to hydrodynamic resonance is the point of transition from absolute to convective instability as discussed by Koch (1985, 1986). The wake tone is a function of the distance of separation between the bodies in the flow field and this forms the basis for three-dimensional disturbances in a near-wake region, vortex control and vortex shedding frequency selection. The drag and lift loading components are a function of the amplitude of oscillation which, when above a threshold level, causes the onset of vortex shedding during the oscillation cycle. The range of vortex modes formed are a function of a non-dimensional amplitude parameter referred to as the Keulegan-Carpenter number $K_c = 2\pi a/d$, see, for example Barltrop & Adams (1991), Lin (1996), where a denotes the amplitude of oscillation and d the diameter of the cylinder. Stocks et al. (1996) characterized and mapped the three-dimensional spatio-temporal structures encountered in the wake of a circular cylinder of finite aspect ratio in terms of the temporal development of the near wake region, i.e from vortex shedding frequency to flow Reynolds number.

For side-by-side stationary cylinder arrangements, the vortex formation in the flow exhibits cross-coupling between the wakes evolved from the neighbouring cylinders and their interaction. Such mechanisms cause alteration to the pressure distribution in the fluid domain, a predominant vortex frequency value and forces acting on the cylinders. The investigations of Mahir & Rockwell (1996) show that the lock-on response frequency range is of the same order as occurs for an equivalent single cylinder with a shift to higher frequencies and to lower amplitudes. The experimental studies of Williamson (1985) clearly illustrate the formation of two parallel vortex streets. When shedding is in anti-phase, two distinct vortex streets are visible and when shedding occurs in-phase, a single large scale *binary vortex* wake is formed created by the superposition of neighbouring wakes.

Even though the flow exhibits many anomalies and distortions in the transitional or turbulent flow regime, the evidence presented shows a close analogy to the observed flow in the lower Reynolds number flow regime in its macroscopic characteristics. This has encouraged many numerical studies in the low Reynolds number flow regime see, for example, Persillon et al. (1995), Zhang & Zhang (1997), to name but a few.

Ng & Ko (1995) concluded that the flow around equal diameter cylinders placed side by side, with a separation gap g^* =0.75 to 1.25, exhibits chaotic and bistable characteristics through a little understood irregular switching mechanism. The present numerical study focuses on this unstable zone of flow and investigations are performed for gap width g^* =0.90 to 1.10 in increments of 0.05. Details of the flow characteristics

in this critical zone together with statistical measures are presented in both time and space and although the flows exhibit irregular behaviour an ordered process is observed as discussed by Ravi et al. (Under review).

2.2 Mathematical Model

Tan et al. (1999) developed a cell viscous boundary element method to solve Navier-Stokes fluid flow problems. This has proved very successful in solving fluid-structure interaction problems involving multi-body configurations as discussed by Farrant (1998), Farrant et al. (2000, 2001) and Uzunoglu et al. (2001). For these reasons details of the numerical approach are omitted and only a brief description of the method is included herein. The numerical scheme of study is a hybrid approach combining boundary element and finite element methods. The boundary element is applied to fluid cells idealizing the fluid domain through an unstructured mesh and global equations are obtained by finite element procedures.

Figure 2.1 illustrates a discretised fluid domain adopting an unstructured mesh involving a number of cell elements.

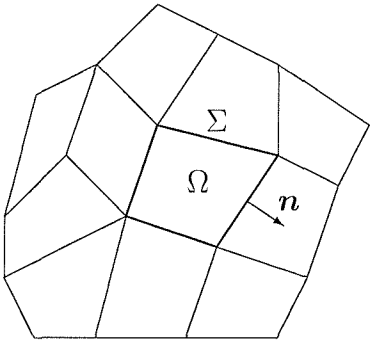

Figure 2.1: Discretisation of the fluid domain by an unstructured mesh involving a typical cell Ω bounded by surface Σ and outward normal $\boldsymbol{n}$.

A typical cell Ω is shown bounded by surface Σ with outward normal $\boldsymbol{n}$. The fluid is assumed incompressible and the governing equation of the flow in terms of a non-dimensional velocity field $v_k(t)$, relative velocity between body $\tilde{v}_k(t)$ and fluid i.e $U_k = \tilde{v}_k(t) - v_k(t)$ and the pressure p is given by

$$\begin{aligned} \dot{v}_j \; + \; (v_j U_k)_{,k} \; + \; p_{,j} \; - \; [\nu_e(v_{j,k} + v_{k,j})]_{,k} &= 0 \; , \\ v_{j,j} &= 0 \; . \end{aligned} \tag{2.1}$$

where $\nu_e(= 1/R_e)$ represents the inverse of the Reynolds number. The subscript index j=1, 2 or j=1, 2, 3 denotes two-dimensional and three-dimensional body-fluid interaction problems respectively.

An integral equation can be formulated from these equations following the methodology of the boundary element method proposed by Tan et al. (1999) who showed that the relevant cell integral equation for incompressible fluid flow may be written in the form,

$$\begin{aligned} C(\boldsymbol{\xi})v_s(\boldsymbol{\xi},t) + \sum_{l=1}^{4} v_j^{(l)} \int_{(l)} (\boldsymbol{un}v_{sj}^* + R_{sj}^*)d\Sigma \\ = \sum_{l=1}^{4} R_j^{(l)} \int_{(l)} v_{sj}^* d\Sigma - \int_{\Omega} h_j v_{sj}^* d\Sigma \end{aligned} \tag{2.2}$$

Here $C(\boldsymbol{\xi})$ is a constant of value 0, 0.5 or 1 depending on the location of the fluid point $\boldsymbol{\xi}$. The weighting functions v_{sj}^* and R_{sj}^* denote the fundamental solution and the related function respectively. $R_j^{(l)}$ represents the traction force on the cell boundary and h_j is the resultant term derived from the acceleration $\dot{v}_j$ after a second order time marching procedure is introduced into the finite difference scheme to resolve the non-linear convective term in equation 2.1. Such a scheme has been shown to be beneficial both analytically and for enhanced computational efficiency.

The application of equation 2.2 to each cell in the idealized fluid domain generates a set of algebraic equations describing the fluid dynamics in the cell. That is, if the superscript e denotes the e^{th} cell, the e^{th} algebraic equations are expressed in the form

$$A_{\mathrm{v}}^{(e)} V^{(e)} = A_{\mathrm{r}}^{(e)} R^{(e)} + b^{(e)} . \tag{2.3}$$

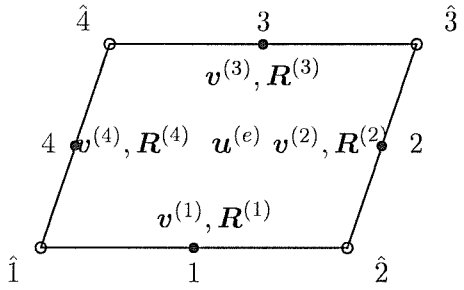

Figure 2.2: A typical quadrilateral cell with ordered notation.

Here,

$$V^{(e)} = \left\{ \begin{array}{c} \boldsymbol{v}^{(1)} \\ \boldsymbol{v}^{(2)} \\ \boldsymbol{v}^{(3)} \\ \boldsymbol{v}^{(4)} \end{array} \right\} , \qquad R^{(e)} = \left\{ \begin{array}{c} \boldsymbol{R}^{(1)} \\ \boldsymbol{R}^{(2)} \\ \boldsymbol{R}^{(3)} \\ \boldsymbol{R}^{(4)} \end{array} \right\}$$

are single column arrays constructed from the velocity $\boldsymbol{v}^{(l)}$ and traction $\boldsymbol{R}^{(l)}$ values at the centre of each edge $(l = 1, 2, 3, 4)$of the cell as shown in Figure 2.2.

Tan et al. (1999) define the coefficients

$$A_{\mathrm{v}}^{(e)} = [\tfrac{1}{2}\delta_{sj} + \int_{(l)} (\boldsymbol{u}\boldsymbol{n} v_{sj}^{*} + R_{sj}^{*}) d\Sigma + \tfrac{3}{8\Delta t} \int_{\Omega} v_{sj}^{*} d\Omega], \tag{2.4}$$

$$A_{\mathrm{r}}^{(e)} = [\int_{(l)} v_{sj}^{*} d\Sigma] \ , \qquad b^{(e)} = \{ \tfrac{(4\bar{v}_j^{(n)} - \bar{v}_j^{(n-1)})}{2\Delta t} \int_{\Omega} v_{sj}^{*} d\Omega \}. \tag{2.5}$$

Their forms relate to the second order time marching procedure chosen, and the evaluations of the respective integrals involve the velocity and boundary integrals containing the values of the surface traction force at the collocation points. The single column array $b^{(e)}$ contains entries evaluated from the domain integral incorporating the contribution of the velocity from the last time step $v_j^{(n)}$ averaged across the cell i.e $\bar{v}_j^{(n)}$. The application of continuity conditions to fluid velocity and surface traction forces at cell interfaces allows a global system of algebraic equations to be derived in the form

$$DV = F \tag{2.6}$$

where V is the array of velocity values on the collocation points in the assigned global order, D is constructed from combination of the coefficients $A_{\mathrm{v}}^{(e)}$ and $A_{\mathrm{r}}^{(e)}$ and F represents the contributions from $b^{(e)}$ arising from the global assembly.

The specification of boundary conditions on the global domain, i.e either velocity V or traction force R, allows solution of the fluid problem as demonstrated by Tan et al. (1999). This cell viscous boundary element method features a high degree of dependence on analytical solutions (i.e fundamental solutions v_{sj}^{*}, R_{sj}^{*} and integrations) in the mathematical model, allowing retention of accuracy of the solution within the numerical scheme of study. It incorporates a primitive-variable formulation and applies to both structured and unstructured meshes. Furthermore the use of velocity and surface traction force as the basic unknowns provides a convenient way of expressing boundary conditions.

The computational domain and the boundary conditions are as shown in Figure 2.5. In the computations conducted, the semi-width of the computational domain $h = 10d$ and the domain upstream is $10d$ whereas the downstream domain is $50d$. An extensive and detailed numerical validation of the method was undertaken by Farrant (1998), Farrant et al. (2000, 2001) for various arrangement of cylinders i.e single, multiple cylinders in tandem, side-by-side, staggered and combination of circular and elliptical cylinders. The influence of mesh refinement, various boundary conditions and domain sizes, time stepping intervals, etc. in the numerical scheme of study were previously investigated through comparisons of predicted values of Strouhal number S (given by $S = fd/U$, where f is the shedding frequency, d is the diameter of the cylinder and U is the free stream velocity), lift coefficient, drag coefficient, flow field pattern, etc. against other predictions using different theoretical approaches and against the experimental evidence provided by Williamson (1985). Such studies are not reproduced here but their findings are incorporated into the present investigation involving a Reynolds number flows R_e=100, 200 and a second order time stepping procedure using time step interval t=0.10 which was shown previously to ensure convergence of solution.

2.3 Numerical Predictions

2.3.1 VCBEM flow field plot for In-phase and Anti-phase shedding.

A selection of results from the research works of Farrant (1998), Farrant et al. (2000, 2001) are briefly listed in Table 2.1 for two cylinders in side-by-side arrangement at R_e=100 and $g^{*} = 3.0$. In case of two cylinders each shedding its own vortex street,

the type of behaviour observed is dependent on both the size of the cylinders and the distance between them. When this distance gets to a few cylinder diameters (to roughly 3 diameters) they start to interact sporadically, sometimes locking in-phase, sometimes slipping by each other. The different modes of shedding are present at R_e=100 and $g^* = 3.0$. An in-phase vortex shedding pattern is seen when the vortex streets lock on and anti-phase shedding pattern is observed when they lock into a pattern of vortex shedding 180 degrees out of phase so that the two streets are a mirror image of one another.

The flow patterns of VCBEM are compared with experiments of Williamson (1985), which show the shedding patterns for anti-phase (Fig 2.3) and in-phase (Fig 2.4).

$Sheddingmode$	C_{dmean}	C_{lmean}	S
$Anti-phase$	1.45	−0.50	0.173
$In-phase$	1.44	−0.40	0.172

Table 2.1: Mean drag(C_d) and mean lift(C_l) coefficients for gap $g^* = 3.0$ between cylinders in different shedding modes at $R_e = 100$.

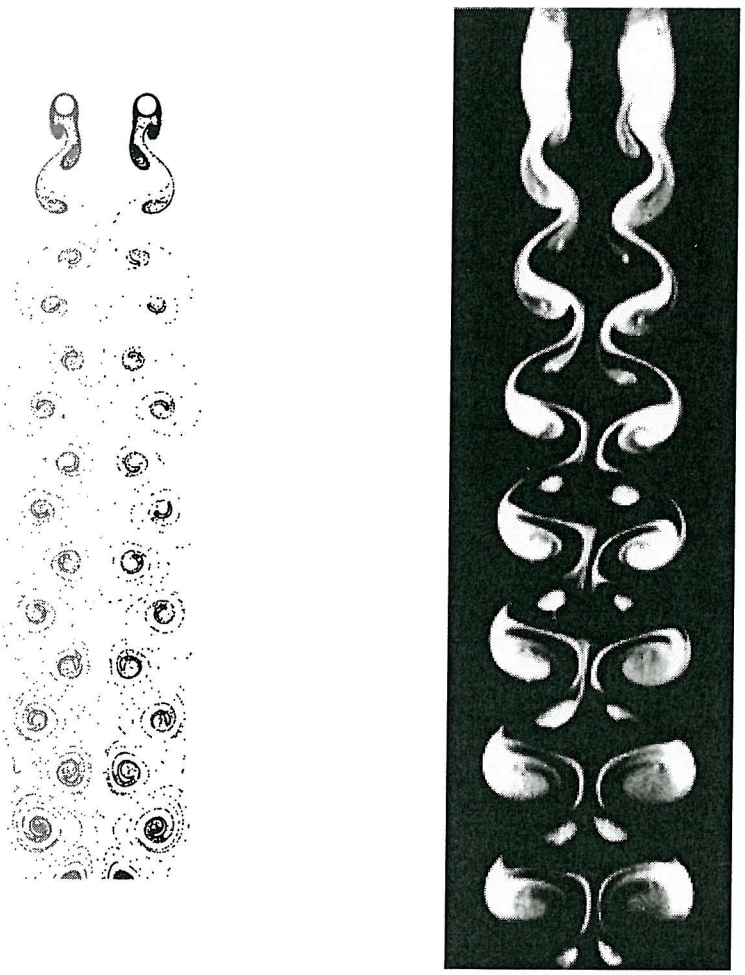

(a) VCBEM (b) Experiment

Figure 2.3: Comparison of VCBEM shedding patterns with experiments of Williamson(1985) for anti-phase vortex shedding at Reynolds number $R_e = 100$ and $g^* = 3.0$.

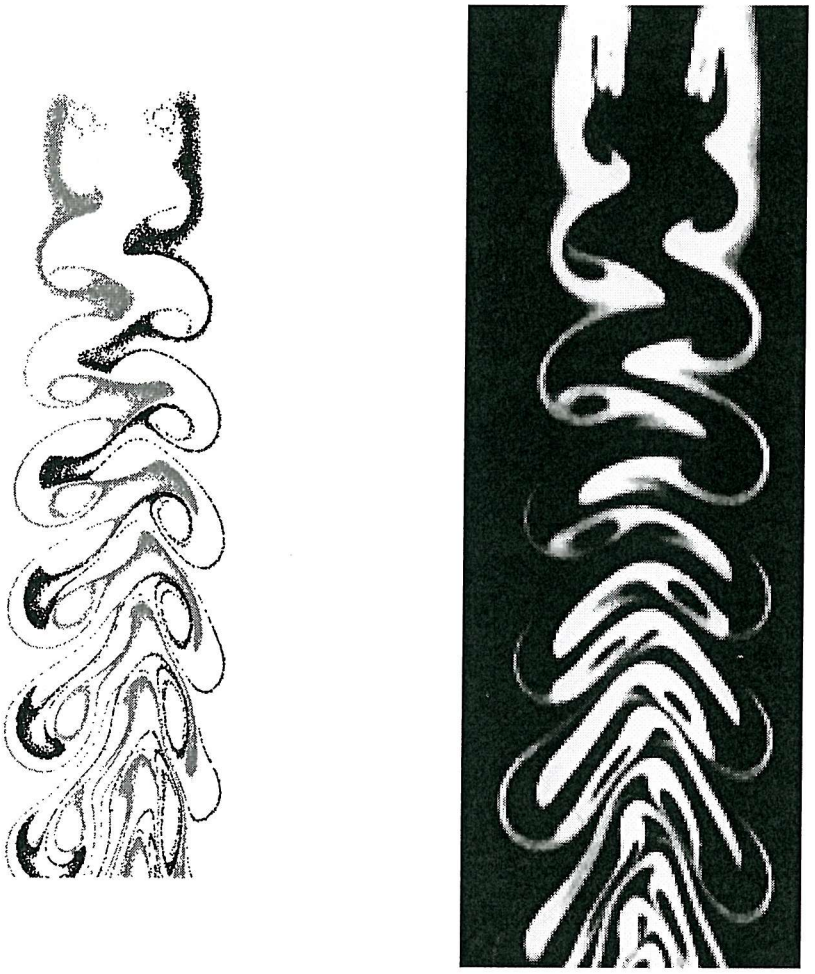

(a) VCBEM (b) Experiment

Figure 2.4: Comparison of VCBEM shedding patterns with experiments of Williamson(1985) for in-phase vortex shedding at Reynolds number $R_e = 100$ and $g^* = 3.0$.

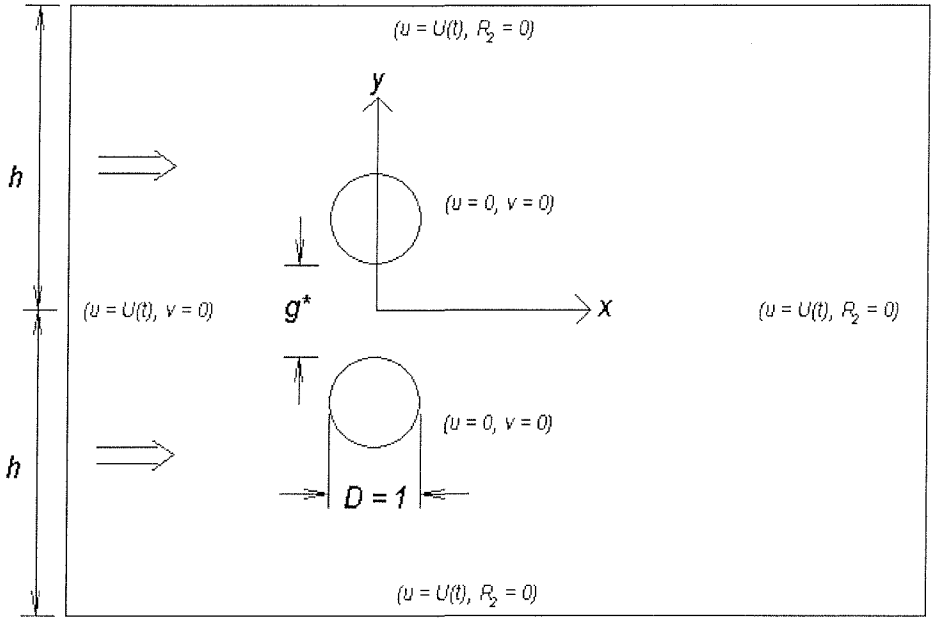

Figure 2.5: Computational domain for twin cylinders

2.3.2 Time simulations.

Adopting the flow doping procedure described by Tan et al. (1999), Figures 2.6, 2.7 and 2.8 illustrate the vortex wake patterns developed behind the cylinder for gap separations g^* =0.95, 1.0 and 1.05 respectively. These records extend approximately 50 cylinder diameters downstream producing a simulation length of 2500 time steps. If required, these records may be extended but the lengths presented illustrate typical patterns. Farrant et al. (2000) previously showed that the wake developed behind side-by-side cylinders at different spacing simulates closely the experimental evidence observed by Williamson (1985).

These wakes show distinctively different patterns resulting from the shedding and interaction between the shed vortices. Namely there is a tendency for in-phase vortex shedding at g^* =0.95 and for anti-phase vortex shedding at g^* =1.05 as described by Farrant et al. (2001). The former pattern indicates strong mixing and the wake generated is more spread and diffuse whereas the latter shows less mixing with the vortices merging to create a tighter spatial wake. During simulations it was noted that switching of in-phase and anti-phase shedding with time was possible in both cases. In some senses, the pattern displayed for g^* =1.0 exhibits a transition phase where thorough mixing and vortex merging occurs. At this separation switching between phases is more likely to arise and a less structured wake pattern is observed but as further evidence is presented there remains an underlying structure to the flow as

indicated by statistical data.

Figures 2.10, 2.11 and 2.12 illustrate the typical time records of predicted lift coefficient, C_l, and drag coefficient, C_d, experienced by the *lower cylinder* for gap separation g^* =1.0. These records extend to over 2000 time step intervals and display distinct patterns. The lift coefficient record clearly shows a beat characteristic about a mean value $C_l = -0.26$. The negative sign signifies a repulsive force. The drag coefficient signal shows less amplitude variation but a more spiky pattern about a mean value $C_d = 1.74$. Figure 2.12 shows a comparison of both signals reflecting the marked differences in these record characteristics. In this investigation, wake vortex patterns were generated for a wide range of different simulation lengths and the selected data presented are typical of the extensive data base created.

2.3.3 Statistical measures.

From the presented time records, statistical measures (i.e mean values, probability density functions, spectral densities) were deduced to provide insights into the mechanisms and behaviour characteristics occurring in the observed complex fluid-structure interaction.

Figures 2.13 and 2.14 illustrate the variation of the probability density functions for lift and drag respectively with different simulated record lengths for g^* =1.0. In each case slight variations between curves are observed for the chosen record length but each set of data demonstrates the same distinctive trends. In subsequent analyses, the 2500 step interval records are used for comparison purposes.

Table 2.2 shows data derived from the various simulation lengths T_s at each separation gap g^* and their sensitivity to these control variables. The mean drag coefficient values indicate little variation with g^* and T_s displaying a very slightly increased value at g^* =1.0. The mean lift coefficient values demonstrate more variation with different gap size and simulation length. It is observed that a maximum value occurs at g^* =0.90 which decreases as g^* increases in value. At each gap size and varying T_s value the maximum drag coefficient C_{dmax} and lift coefficient C_{lmax} remain constant displaying invariance to T_s value. Variation in these parameters is observed with changing value of g^* with C_{dmax} showing a decreasing trend apart from the range $0.90 \leq g^* \leq 0.95$ and C_{lmax} displaying an increasing trend as g^* value increases. The largest variation in this data set is illustrated in the changing value of Strouhal number with g^* which reaches a maximum value at g^* =0.95.

Figures 2.15 and 2.16 display the variation of the probability density functions for lift and drag respectively for different gap separation g^*. Although the maximum

g^*	T_s	C_{dmean}	C_{lmean}	C_{dmax}	C_{lmax}	S
	1800	1.73	−0.28	2.08	0.24	
0.90	2100	1.73	−0.29	2.08	0.24	0.195
	2500	1.73	−0.29	2.08	0.24	
	1800	1.73	−0.27	2.09	0.26	
0.95	2100	1.73	−0.27	2.09	0.26	0.215
	2500	1.73	−0.27	2.09	0.26	
	1800	1.75	−0.26	2.04	0.34	
1.00	2100	1.75	−0.26	2.04	0.34	0.195
	2500	1.74	−0.26	2.04	0.34	
	1800	1.74	−0.25	2.04	0.34	
1.05	2100	1.74	−0.25	2.04	0.34	0.176
	2500	1.73	−0.26	2.04	0.34	
	1800	1.74	−0.24	2.03	0.38	
1.10	2100	1.73	−0.24	2.03	0.38	0.176
	2500	1.73	−0.24	2.03	0.38	

Table 2.2: Relative comparison of drag(C_d) and lift(C_l) coefficients for different gaps g^* between cylinders and different simulation lengths T_s for $R_e = 100$.

values of the probability density functions for lift show variation the overall shape of the five curves demonstrates similarity. Figure 2.15 shows that as the separation gap increases from g^* =0.90 the more pronounced probability density function peak feature observed at g^* =0.90 decreases to a relatively flat parabolic curve at g^* =1.10. The features displayed in Figure 2.16 for the drag probability density function show a measure of similarity with a more pronounced peak structure at g^* =0.95, 1.0 and 1.05.

Typical lift and drag power spectra curves are displayed in Figures 2.17 and 2.18 for g^* =0.90. The lift coefficient spectral density with its dominant low frequency content displays a maximum value at the Strouhal frequency. The lower frequency peak observed in the power spectra curves is of value comparable to the envelope frequency of the C_l curve illustrated in Figure 2.12. A similar pattern is observed in the drag coefficient spectral density curve but in the low frequency region, three shedding frequencys are seen for the Strouhal frequency which contrasts to the dominant shedding frequency displayed in the lift coefficient case. As seen, the third peak is insignificant compared with the other two.

The wake patterns developed behind the cylinder are as shown in Figures 2.6, 2.7 and 2.8. Figure 2.9 summarises the wake patterns generated for different gaps g^*.

Figure 2.6: Wake patterns generated behind side-by-side cylinders of equal diameter for $g^* = 0.95$

Figure 2.7: Wake patterns generated behind side-by-side cylinders of equal diameter for $g^* = 1.00$

Figure 2.8: Wake patterns generated behind side-by-side cylinders of equal diameter for $g^* = 1.05$

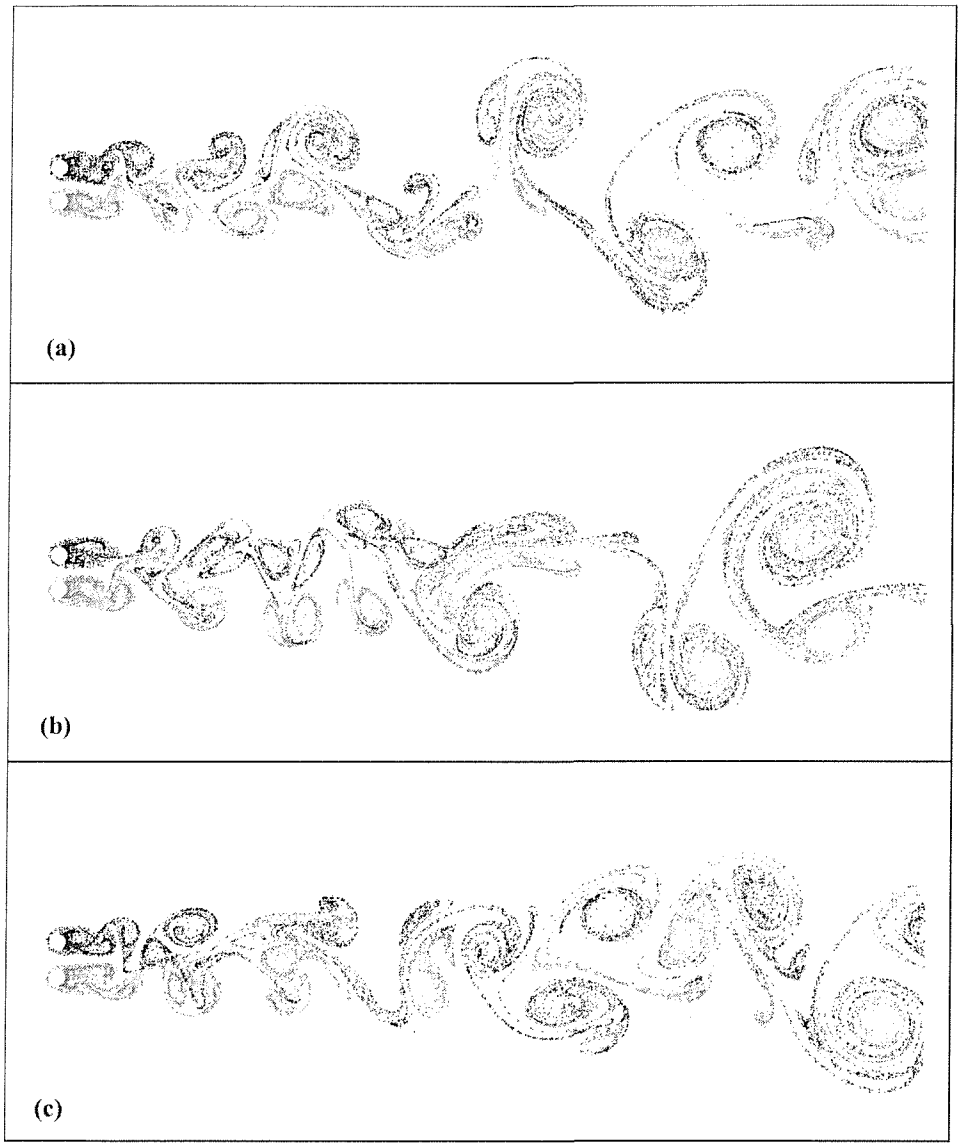

Figure 2.9: Wake patterns generated behind side-by-side cylinders of equal diameter for different gaps (a) $g^* = 0.95$ (b)$g^* = 1.00$ (c)$g^* = 1.05$

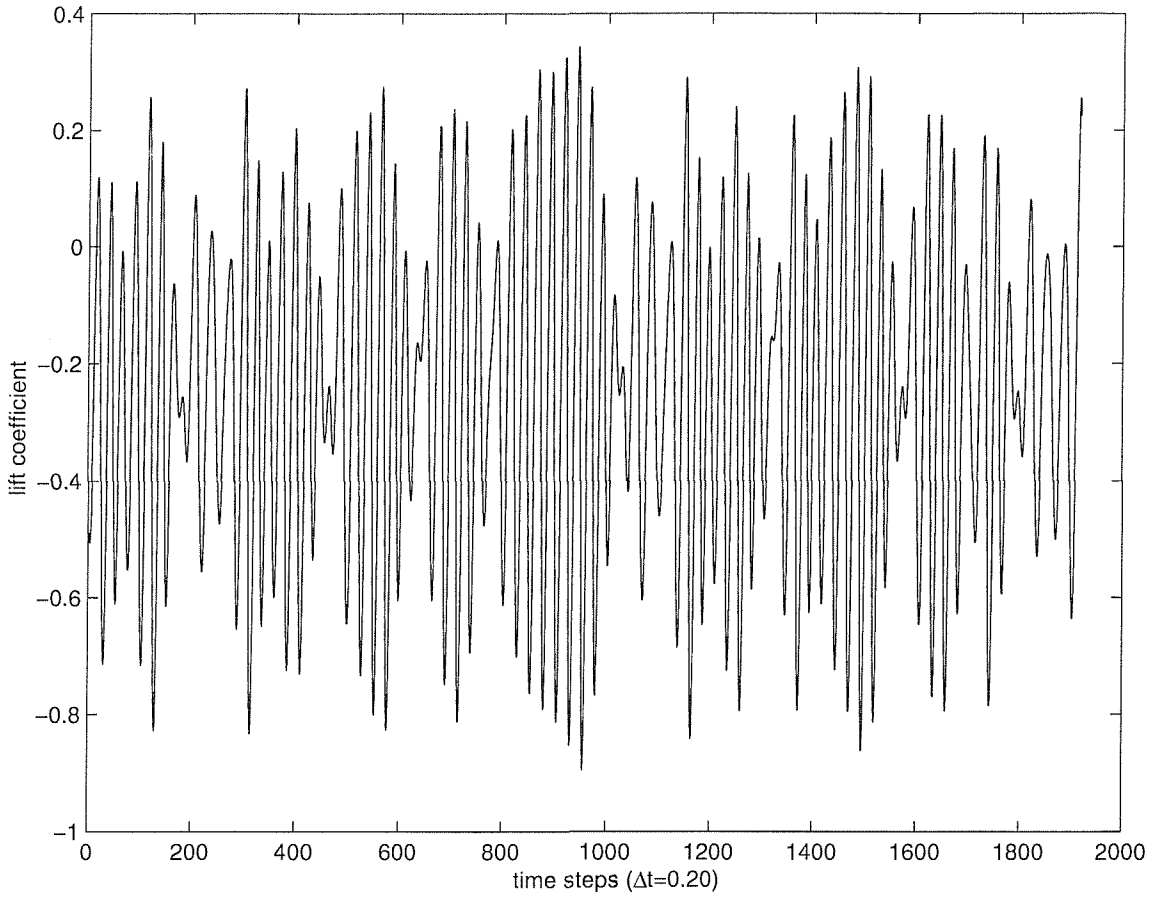

Figure 2.10: Variation of lift coefficient C_l with time for $g^* = 1.00$

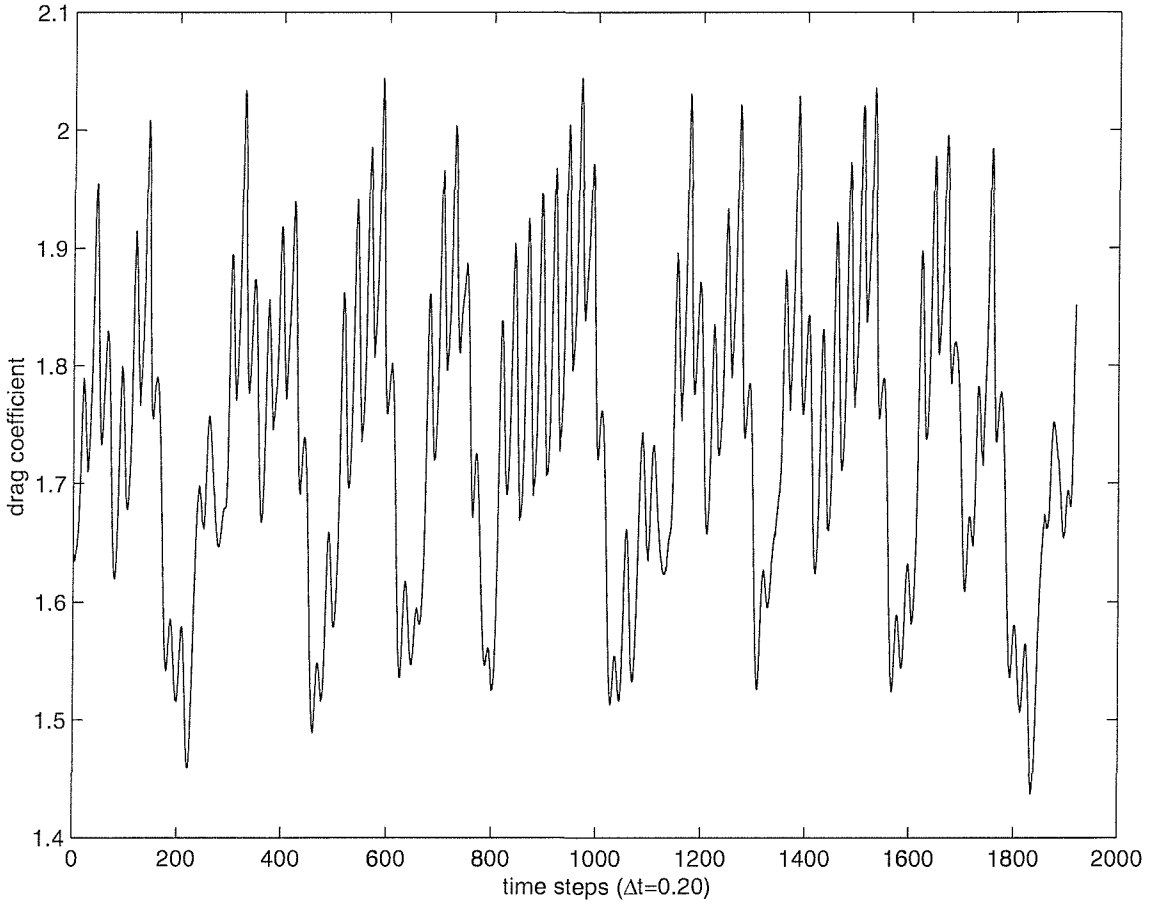

Figure 2.11: Variation of drag coefficient C_d with time for $g^* = 1.00$

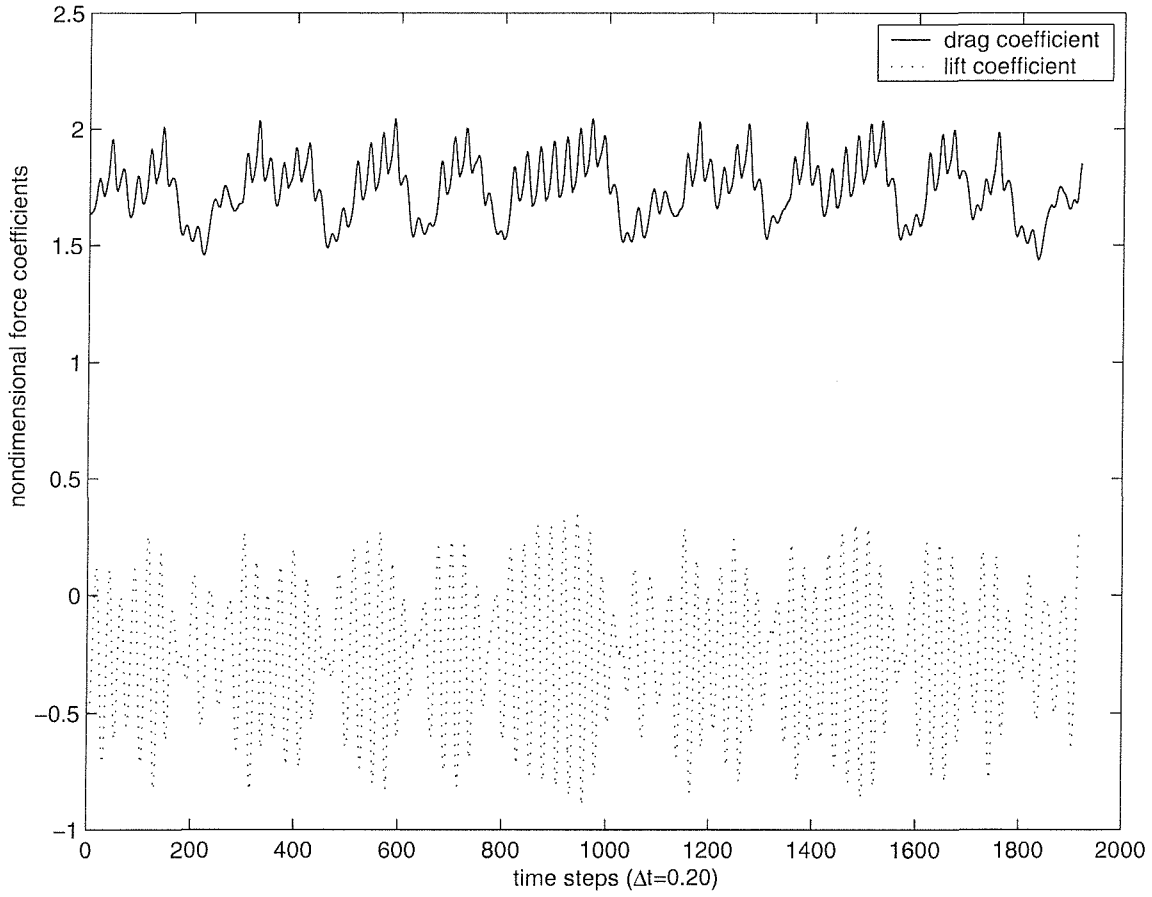

Figure 2.12: Superposition of C_l and C_d records with time illustrating the different characteristics for $g^* = 1.00$

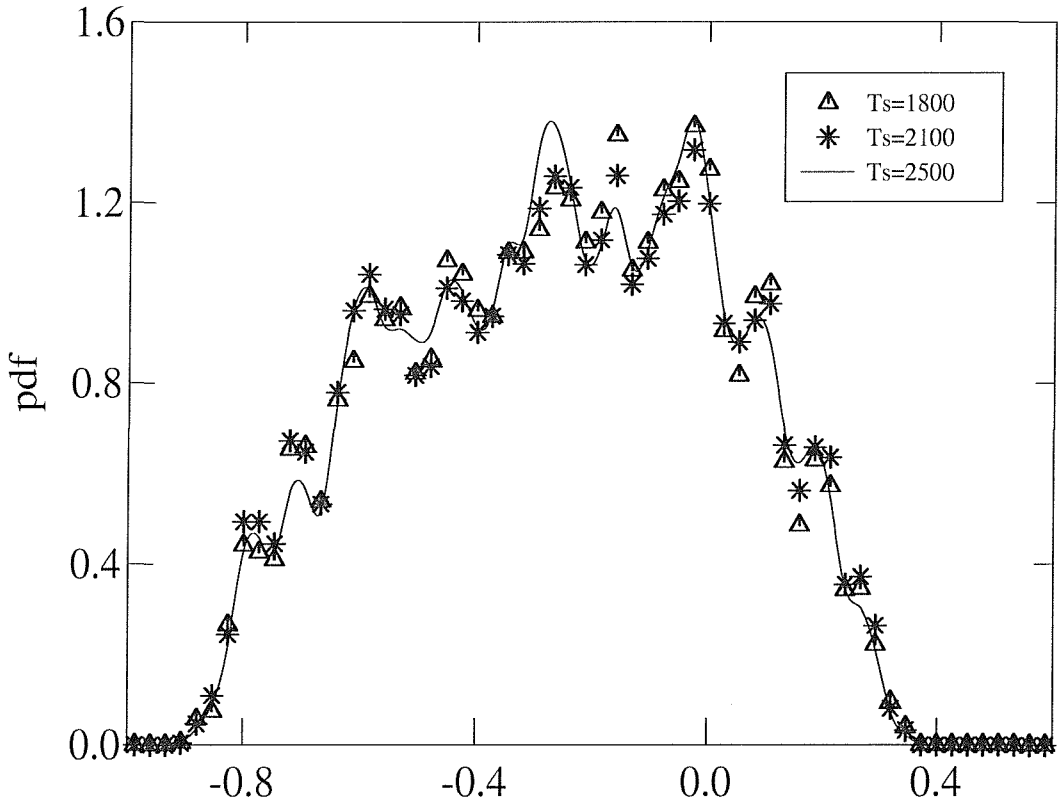

Figure 2.13: Variation of probability density function for lift C_l at $g^* = 1.00$ for different intervals of simulated record length $T_s = 1800, 2100, 2500$ step intervals.

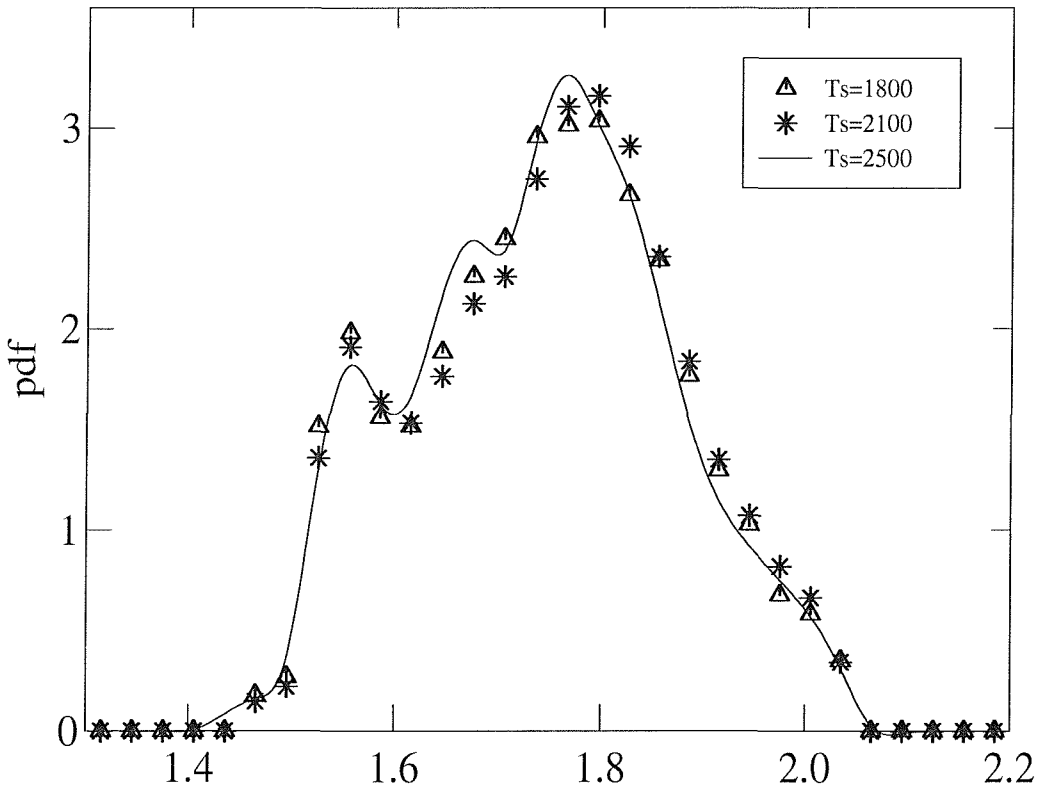

Figure 2.14: Variation of probability density function for drag C_d at $g^* = 1.00$ for different intervals of simulated record length $T_s = 1800, 2100, 2500$ step intervals.

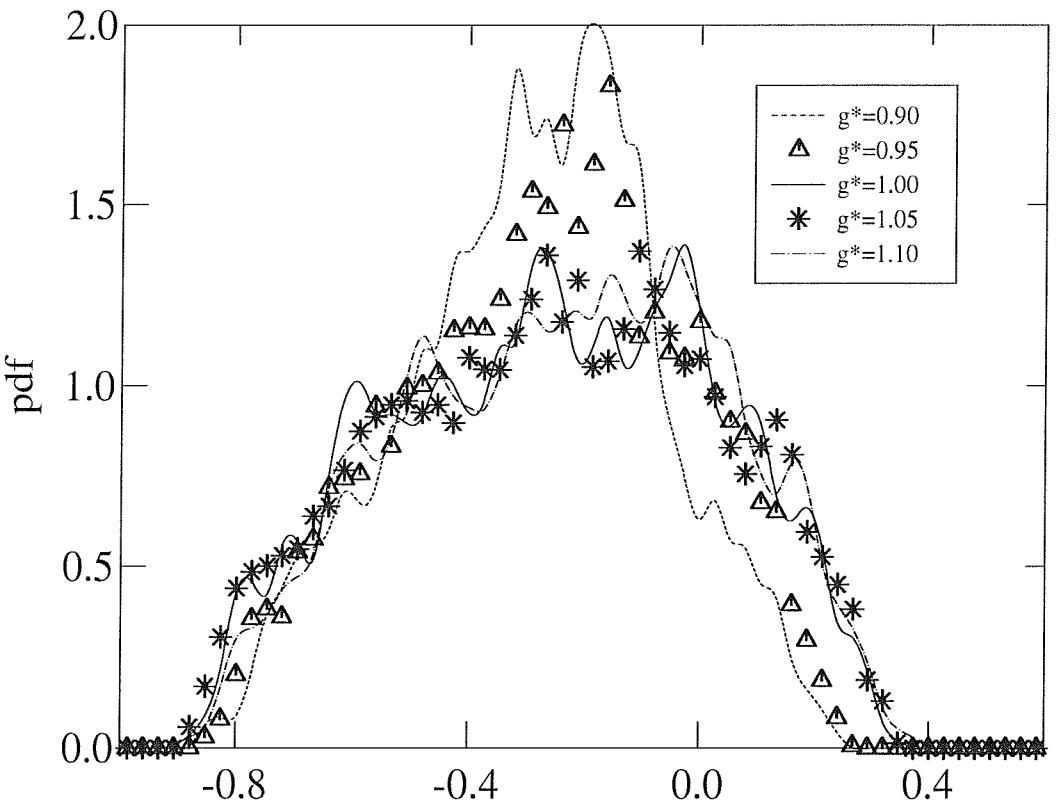

Figure 2.15: Variation of probability density function for lift C_l for simulated record length of 2500 step intervals for separation gap $g^* = 0.90, 0.95, 1.00, 1.05, 1.10$.

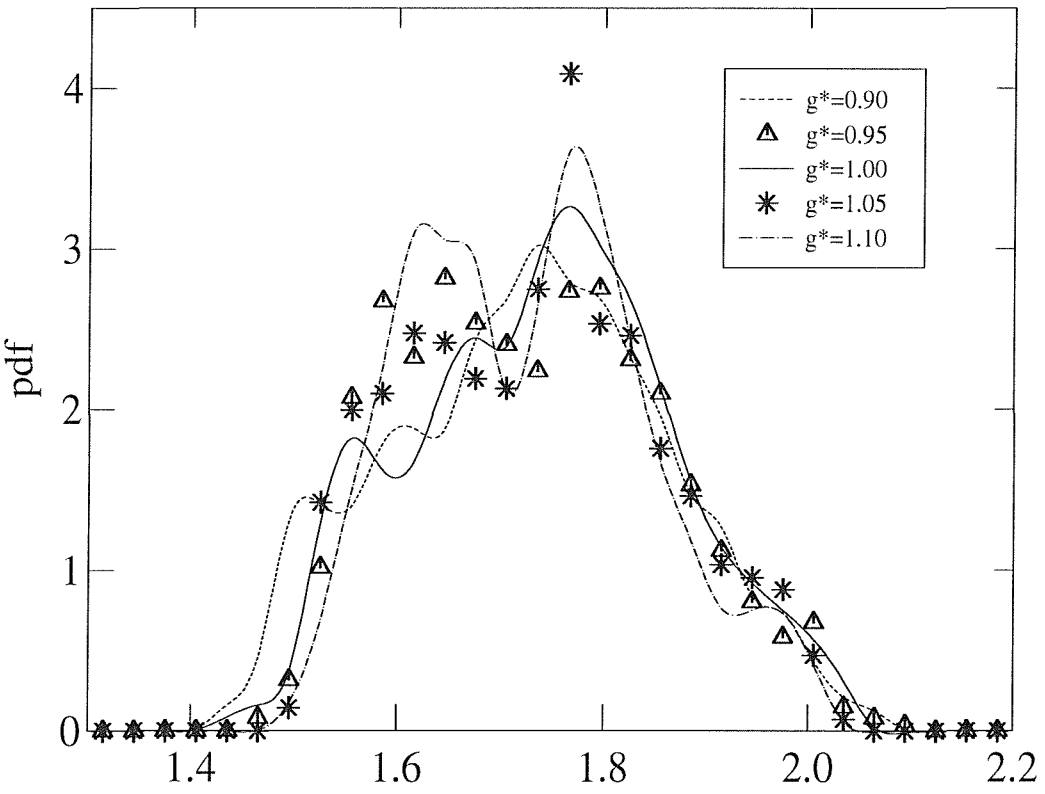

Figure 2.16: Variation of probability density function for drag C_d for simulated record length of 2500 step intervals for separation gap $g^* = 0.90, 0.95, 1.00, 1.05, 1.10$.

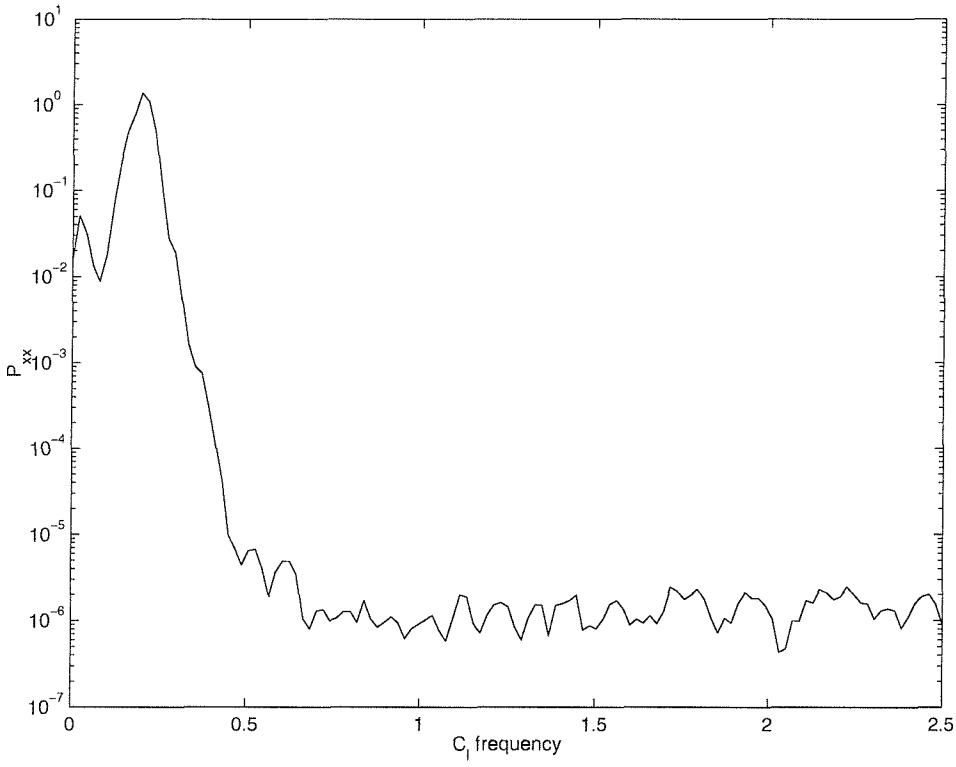

Figure 2.17: Typical variation of power spectral density for lift coefficient C_l (Dominant peak frequency value: 0.1953)

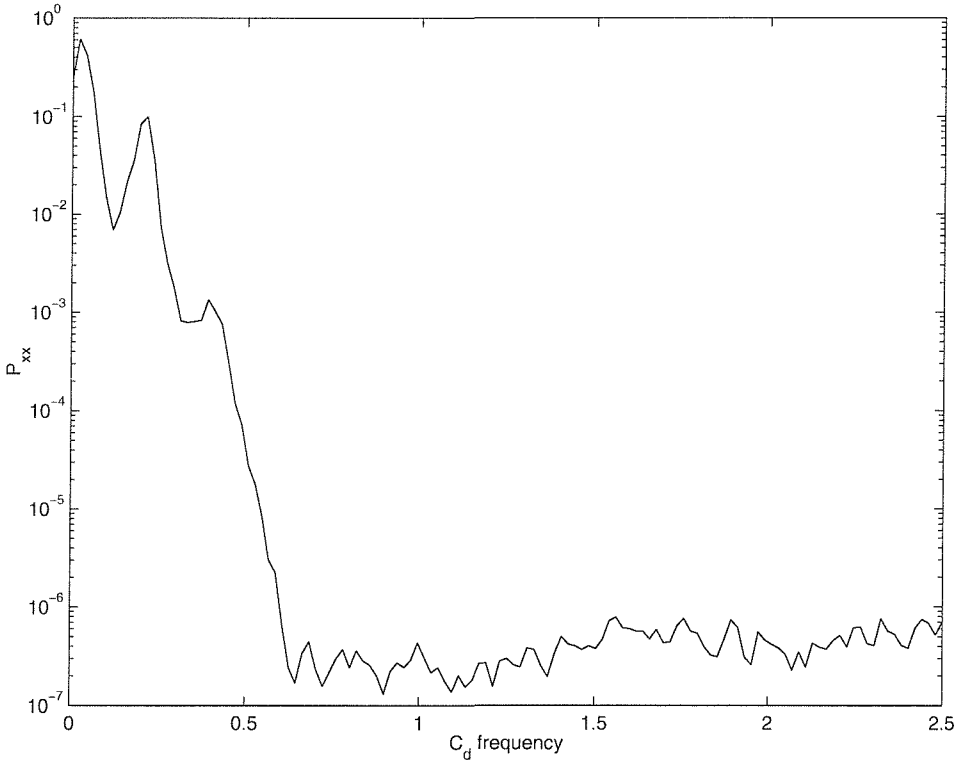

Figure 2.18: Typical variation of power spectral density for drag coefficient C_d (Dominant peak frequency values: 0.0173, 0.1953, 0.3859)

2.4 Conclusions

For parallel stationary cylinders, with spacing g^* =0.95 to 1.05, placed in a uniform viscous flow ($R_e = 100$) the predicted vortex patterns show dependence on the spacing factor which also relates to the interaction mechanism and vortex shedding frequency. Namely, for g^* =0.95, as shown in Figure 2.6, an in-phase vortex shedding pattern occurs with strong vortex mixing, a diffused wake and a maximum Strouhal frequency value. In contrast at g^* =1.05, as illustrated in Figure 2.8, an anti-phase vortex pattern dominates with weak vortex mixing, a tighter spatial wake and the Strouhal frequency tends to a minimum value. At the critical value of g^* =1.0, as shown in Figure 2.7, a thorough mixing and amalgamation of vortex occurs with an intermediate Strouhal frequency value. In-phase and anti-phase vortex shedding switching is observed and a less structured wake occurs. This provides indication of a chaotic behaviour but in all cases the statistical measures reveal an ordered system.

From this evidence, for g^* <1.0 the vortex wake is influenced by in-phase vortex shedding whereas for g^* >1.0 anti-phase vortex shedding is more evident. The next Chapter presents an extension of the present analysis to study the behaviour of circular cylinders when subjected to external forcing. In particular, we consider the rotation of a cylinder as the forcing mechanism and analyse the shedding patterns of twin cylinders in various arrangements.

Chapter 3

Analysis of Rotating Cylinders

3.1 Introduction

The study of the fluid flow past a circular cylinder in steady motion or started from rest in viscous fluids has been an area of theoretical and experimental research for a long time. The problem of flow past a rotating cylinder is of fundamental interest for its variety of practical applications eg. boundary layer control on aerofoils (Tennant et al., 1976) and lift enhancement which is an example of the Magnus effect (Prandtl & Tietjens, 1934, Batchelor, 1971, Sayers, 1979).

The increase in lift is complemented by a high drag penalty, which produces very low aerodynamic efficiency and this is not favourable for practical flow control devices (Nair et al., 1998). The studies of Prandtl show that rotation has the effect of inhibiting the boundary layer separation and this separation can be suppressed completely at high rotational rates. This has prompted Tennant et al. (1976), Modi et al. (1990)and Graham et al. (1999) to use a rotating cylinder as a control device to enhance the performance characteristics on the flaps of aircraft, upstream ship rudders, subsonic diffusers etc.

Batchelor (1971) discussed the Magnus effect on the basis of inviscid theory, which produced lift proportional to the rate of rotation. This, however, is not the case for real fluids with boundary layer separation. Coutanceau & Menard (1985) stated that their experimental results relating to the Magnus effect exhibited a two-dimensional flow field. The influence of surface roughness and other three dimensional effects play a significant role in moderate-to-high Reynolds number flow regimes as discussed by Nair et al. (1998).

Although, there have been numerous numerical simulations relating to rotating cylinder problems, a steady state numerical solution was obtained by Ingham & Tang

(1990), Tang & Ingham (1991) for Reynolds number upto 20. The unsteady flow past a rotating cylinder for low Reynolds number tends to attain a steady state after a prolonged length of simulation. The investigations of Badr et al. (1989) on time dependent calculations indicated that for higher Reynolds number $R_e = 60$ and $R_e = 100$ the flow does not tend to steady state. Tang & Ingham (1991) produced a steady state solution by solving the time dependent Navier-Stokes equation for $R_e = 60$, $R_e = 100$ and rotational parameter α in the range, $0 \leq \alpha \leq 1$. They adopted a numerical scheme which circumvents the constraints of satisfying the boundary conditions at large distance from the cylinder as originally discussed by Ingham & Tang (1990). The study of Baban et al. (1989) on the unsteady forces on circular cylinders showed that, for a two dimensional cylinder in a crossflow, vortex shedding is truly two dimensional and the strength of roll up vortices is fairly uniform along the span (Park & Lee, 2000). In the near wake region of a two dimensional circular cylinder, three dimensionality of the regular vortex shedding is weak with shedding parallel to the cylinder axis and hence the cylinder wake is a two dimensional flow. Also, the Strouhal number does not change along the cylinder's axis if small aspect ratio and appropriate end plates are used (Szepessy & Bearman, 1992).

Significant studies were performed using rotating cylinders as control devices (Tennant et al., 1976, Modi et al., 1990). The advent of micro-electronics has made active control of fluid flows a technical reality.

The control of vortex shedding using a rotating circular cylinder as the controlling device and the concept of optimal control are incorporated into the flow control problem (Homescu et al., 2002). Low dimensional models, which are amenable to control mechanisms, are described in detail and developed by Graham et al. (1999) to achieve efficiency in controlling fluid flows.

In this chapter, validation of the mathematical model describing rotation of a cylinder in a viscous flow and application of the model to the study of the interaction between twin cylinders are investigated. Firstly, a brief overview of the mathematical model with rotation implementation in VCBEM is explained, which is followed by computational domain specifications. The details of the validation of the modified VCBEM model with parametric studies are presented and physical phenomena discussed. Finally, the rotation of twin cylinders for Reynolds number $R_e = 100$ and $R_e = 200$ in side-by-side and tandem arrangements are presented. The effects of key flow parameters, characteristics of drag and lift and vortex shedding patterns are assessed and validated through comparison with experimental results and theoretical predictions. Details of flow characteristics and vortex shedding patterns are illustrated.

3.2 Mathematical Model

The mathematical formulation is explained in Chapter 2, section 2.2. In this section a brief review of the mathematical formulation with time marching schemes is presented and implementation of the rotational boundary conditions on the cylinder discussed.

For the unstructured mesh shown in Figure 2.1 involving a number of cell elements, the sequence of operations involved is herein briefly listed.

- Governing equation for incompressible flows are derived in terms of non-dimensional velocity field as in section 2.2.

- Before transformation of the Navier-Stokes equations into an integral form, Tan et al. (1999) resolved the nonlinear convective term in the momentum equation by time marching schemes. It was shown that this process enhances the efficiency and effectiveness of the overall calculation. The chosen form of time marching is second order. The second order level of numerical accuracy in Δt is achieved at the (n+1)th time step by adopting the approximations

  $\dot{v}_j = \frac{1}{2\Delta t}[3v_j - 4v_j^{(n)} + v_j^{(n-1)}]$ and $U_k = 2v_k^{(n)} - v_k^{(n-1)} - \tilde{v}_k(t)$

  The mathematical basis for the formulations is discussed by Stiefel (1963).

- Formulation of integral equation using method proposed by Tan et al. (1999).

- Specification of boundary conditions on global domain, i.e either velocity V or traction force R, to solve the specific flow problem. It incorporates a primitive-variable formulation and applies to both structured and unstructured meshes.

The problem of rotating cylinders under consideration can be tackled by various numerical procedures. One of the approaches is by using the patched-overset grids, which conceptually simplifies the simulation of fluid-structure interaction discussed by Steger et al. (1983), Freitas & Runnels (1999), David (2001). One of the approaches in implementing an overset grid is by constructing the background grid resolving the entire simulation domain and additional grids surrounding the moving bodies are placed over the background mesh, with no attempt made to align the grid points on the overset grid with that of background mesh, as discussed by Freitas & Runnels (1999). The boundary conditions on overset grids are determined by the interpolation of the current flow solution from the background grid as intermediate boundary conditions in an iterative solution. The obvious limitation on the overset grid method is the development of fast and accurate interpolation schemes for determining the boundary

conditions on the overset grids to minimize the computational penalty on the method (Steger et al., 1983, Freitas & Runnels, 1999).

In VCBEM, one procedure is to alter the fundamental solution to incorporate rotation or the other is to incorporate the boundary conditions on the cylinder surface without the alteration of fundamental solution. Consider the latter approach of incorporating the boundary conditions on the surface and this process can be carried out in two different ways. One procedure is to generate a new mesh iteratively in the time marching process of VCBEM solution, which imposes a computational penalty on the method as a tradeoff for analytical simplification of the solution process and the other is to integrate the mesh generation programme and the VCBEM solver. In the current research a modified VCBEM is developed to incorporate rotation on cylinders by altering the boundary conditions on the surface of the cylinders, which is achieved by integrating the mesh generation programme and VCBEM solver with appropriate modifications.

The boundary conditions are expresssed conveniently using velocity and surface traction force as the basic unknowns. In this research, the rotation boundary conditions are incorporated on the surface of the cylinder without altering the fundamental solution and the VCBEM solver is further modified to account for time dependent boundary conditions in flow simulations of Navier-Stokes equations so as to ensure computational efficiency of the method. The mesh generation programme is modified to implement the rotation boundary conditions on the surface of cylinder and it generates the necessary unstructured mesh for the modified VCBEM solver.

In the case of the numerical simulations, the translation of the cylinder is incorporated in the relative motion of the horizontal free stream velocity $U = 1.0$ and rotation is implemented in the boundary nodes on the cylinder surface with horizontal and vertical velocity components $u = -\gamma y$ and $v = \gamma x$, where γ represents an angular velocity which may be constant or varying with time. The relative motion of freestream with respect to the cylinder provides a space fixed cartesian co-ordinate system of analysis. The boundary nodes with specified boundary conditions are generated in a modified mesh generation programme and the body nodes on the cylinder surface with boundary conditions $u = -\gamma y$ and $v = \gamma x$ are derived. The so derived boundary nodes are used in the modified VCBEM solver to impart initial conditions in the time marching of Navier-Stokes equations. Parametric studies are conducted to investigate the effect of γ and results of C_l and C_d records with time illustrating the different characteristics for $R_e = 100$ are presented in section 3.4.3. In the case of multi-body configuration, rotation on each body is discretely controlled. Hence, cylinders in multi-body configuration can be used as sensors and actuators with different angular rotations providing

a way ahead for optimal control of multi-body configuration of cylinders.

3.3 Computational Domain

Here the focus is on the prediction and description of the incompressible flow past a rotating circular cylinder of diameter 'd'. The computational domain and boundary conditions are shown in Figure 3.1 where, τ_1, τ_3, τ_4 and τ_2 represent boundary conditions on the inlet, outlet, top and bottom extreme boundaries respectively, whereas τ_c represents the no-slip condition on the surface of the cylinder at coordinate (x, y) with velocity $u = -\gamma y$, $v = \gamma x$ and γ ($\gamma = \omega d/U$, where ω is the dimensional angular velocity, d is the diameter of the cylinder and U is the free stream velocity) represents an angular rotation of cylinder normalized by the freestream velocity which may be constant or varying with time. The cylinder rotates with angular velocity γ and an anti-clockwise rotation represents a positive rotation in the mathematical model. The top and bottom boundary conditions of the computational domain are maintained symmetric and the mixed boundary conditions are assumed to have no horizontal traction force and no velocity in the vertical direction. The outlet has no traction force and the inlet has a uniform horizontal velocity.

For steady fluid flows with the cylinder stationary (i.e $\gamma = 0$) at $R_e = 100$ and $R_e = 200$, extensive validation exercises were undertaken by Farrant (1998) and Uzunoglu et al. (2001) to test the sensitivity of the boundary conditions on the parameter values of lift C_l and drag C_d. It was noted by Tan et al. (1999) that the rate of change of drag coefficient reduces exponentially with distance of the boundary from the centre of the cylinder. The findings of Farrant (1998), Uzunoglu et al. (2001) showed that, when the semi-width (h) of the domain is sufficiently large, the influence of the boundary conditions on C_l and C_d is insignificant. For mixed boundary conditions of velocity and traction forces, Uzunoglu et al. (2001) showed that if h is the semi-length and semi-width of a computational domain then $h = 9d$ is sufficient. These findings are incorporated in the present investigation and for computations, the upstream domain and semi-width of the computational domain adopted is $10d$ whereas the downstream domain is taken as $50d$ so that an extensive wake flow pattern region is captured.

Source	Method	C_{dmean}	C_l (peak to peak)
Tritton (1960)	experimental	1.26	-
Henderson (1995)	spectral ele.	1.35	-
Li et al. (1991)	finite ele.	1.33	0.72
Mittal et al. (1991)	finite ele.	1.39	0.74
CFX-3D	finite vol.	1.36	0.65
VCBEM	VCBEM	1.33	0.67
Graham et al. (1999)	finite ele.	1.34	-
He et al. (2000)	finite ele.	1.35	-

Table 3.1: Relative comparison of mean drag (C_{dmean}) and C_l (peak to peak) for Reynolds number R_e=100 for an isolated stationary cylinder

No. of collocation points	S	C_{dmean}	C_l (peak to peak)
8244	0.163	1.39	0.55
12350	0.164	1.35	0.64
17336	0.164	1.33	0.65
21600	0.164	1.33	0.67
26512	0.164	1.33	0.68

Table 3.2: The effect of mesh refinement on Strouhal number (S), mean drag (C_{dmean}) and C_l (peak to peak) for Reynolds number R_e=100 for an isolated stationary cylinder

3.4 Numerical Predictions

3.4.1 Validation of VCBEM for rotation

The computational domain and boundary conditions are described in Figure 3.1. Numerical simulations were performed in flow regimes defined by Reynolds number R_e=100 and R_e=200 for the cylinder with no rotation ($\gamma = 0$) and rotating with steady angular velocity ($\gamma = 1$). The present validation builds on previous studies of Farrant (1998), Farrant et al. (2000), Uzunoglu et al. (2001) and Farrant et al. (2001) who provide detailed analysis of the effect of time stepping and mesh refinement on convergence of solution. These studies were for the case $\gamma = 0$, which are listed in Tables 3.1-3.3, briefly summarising the previous research works (Farrant, 1998) and after repeating their studies and incorporating their findings it was found that for the cases of $\gamma \neq 0$ a mesh size 0.10×0.10 and time step length $\Delta t = 0.10$ were adequate for a similar level of accuracy and convergence of solution. Tables 3.1-3.3 show a comparison of predictions of Strouhal number S, mean drag coefficient C_{dmean} and peak to peak value of C_l for an isolated cylinder with $\gamma = 0$ and R_e=100. Tables 3.4-3.8 show

Δt	S	err. against Williamson(1991)	C_{dmean}	C_l (peak to peak)
0.4	0.169	3.0%	1.45	1.01
0.2	0.166	1.2%	1.35	0.73
0.1	0.164	0.0%	1.33	0.67
0.05	0.163	0.6%	1.33	0.66
0.025	0.163	0.6%	1.33	0.66
Williamson(1991)	0.164	-	-	-

Table 3.3: Relative comparison of Strouhal number (S) with experiment of Williamson (1991) for an isolated stationary cylinder at Reynolds number R_e=100

Δt	C_{dmean}	C_{lmean}
0.10	1.62	−1.29
0.20	1.65	−1.30

Table 3.4: Relative comparison of mean drag (C_{dmean}) and mean lift (C_{lmean}) for an isolated rotating cylinder, Reynolds number R_e = 100 and angular rotation of cylinder γ =1.0 for mesh size 0.10 × 0.10 and different time steps Δt

data of mean drag and lift coefficients for $\gamma = 1$ with variation in Reynolds number R_e, time steps and mesh sizes.

Table 3.4 shows the variation of the mean drag (C_{dmean}) and mean lift (C_{lmean}) coefficients with Δt whereas Table 3.5 shows variation of coefficients C_{dmean} and C_{lmean} with different mesh sizes for time step $\Delta t = 0.10$.

Table 3.6 shows the comparison of mean drag and lift parameters derived from modified VCBEM for the Reynolds number $R_e = 200$ and the rate of angular rotation γ =1.0 with other numerical simulations.

Tables 3.7 and 3.8 show the comparison of the predicted Strouhal number S derived by the modified VCBEM model with other numerical findings. Chen et al. (1999) used upwind schemes for the simulation of the rotating circular cylinder with a rate

Meshsize	C_{dmean}	C_{lmean}
0.10 × 0.10	1.62	−1.29
0.15 × 0.15	1.61	−1.29
0.20 × 0.20	1.60	−1.31

Table 3.5: Relative comparison of mean drag (C_{dmean}) and mean lift (C_{lmean}) for an isolated rotating cylinder, Reynolds number R_e = 100 and angular rotation of cylinder γ =1.0 for $\Delta t = 0.10$ and different mesh sizes

Source	C_{dmean}	C_{lmean}
VCBEM	1.43	−1.23
Chen et al. (1999)	1.25	−1.22
Homescu et al. (2002)	1.42	–

Table 3.6: Relative comparison of mean drag (C_{dmean}) and mean lift (C_{lmean}) for an isolated rotating cylinder, Reynolds number R_e = 200 and angular rotation of the cylinder γ =1.0

Source	S
VCBEM	0.163
Badr et al. (1989)	0.16
He et al. (2000)	0.167

Table 3.7: Relative comparison of Strouhal number (S) for an isolated rotating cylinder, Reynolds number R_e=100 and angular rotation of cylinder γ=1.0

of rotation γ =1.0. Numerical results of Chen et al. (1999) were compared with the simulation of Nair et al. (1998) who dealt with the evolution of wake patterns for different flow regimes but values of force co-efficients are not presented. The typical C_l and C_d records with time are as shown in Figure 3.4 which illustrates the characteristics occurring in the R_e = 100 flow regime.

3.4.2 Physical phenomena

The convection of vortices are studied as a function of Reynolds number of the flow regime. In a stationary cylinder with no rotation (γ = 0), for low Reynolds number R_e < 40, there exists a steady recirculation region with two symmetrically placed vortices behind the stationary cylinder which grows in size with increase in Reynolds number. For 40 < R_e < 60 this trailing vortex becomes unstable and an unsteady wavy pattern is developed. Karman vortex shedding occurs in the near wake due to

Source	S
VCBEM	0.194
Chen et al. (1999)	0.194
Badr et al. (1989)	0.20
He et al. (2000)	0.1928

Table 3.8: Relative comparison of Strouhal number (S) for an isolated rotating cylinder, Reynolds number R_e=200 and angular rotation of cylinder γ=1.0

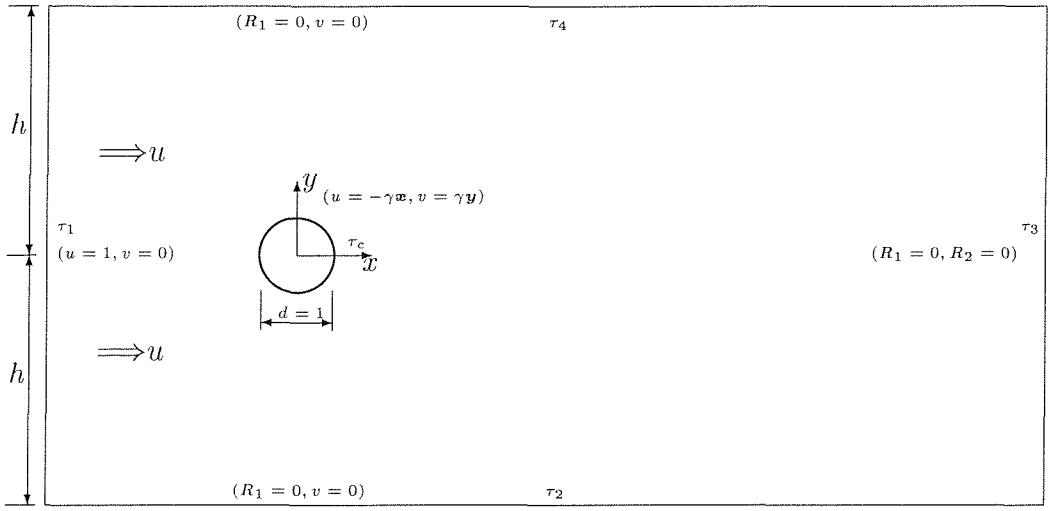

Figure 3.1: Computational domain definition and boundary conditions for rotating cylinder in a uniform flow. All the variables and quantities are nondimensional

flow instabilities with fluctuating pressure and thus an oscillating lift force is developed on the cylinder. The attached vortices become asymmetric and are alternatively shed at a particular frequency as discussed by Williamson (1996), Ding & Kawahara (2000), Homescu et al. (2002).

Bearman (1984) discussed the postulate of Gerrard (1966) that in separating shear layers vortex continues to grow, until it is strong enough to draw the opposing shear layer across the near wake. The rotation of the cylinder ($\gamma \neq 0$) in a viscous uniform flow modifies the wake flow patterns and vortex shedding configuration, which may reduce the flow-induced oscillation or augment the lift force. The basic physical rationale of the influence of rotation is that the flow on the upper region of the cylinder is decelerated and easily separates whereas the flow on the lower region of the cylinder accelerates and separation is suppressed or delayed. Hence a mean lift force is generated as a result of pressure differences created on the accelerated and decelerated sides of the cylinder (Homescu et al., 2002) creating what is known as *Magnus effect* (Barkla & Auchterlonie, 1971, Batchelor, 1971).

As the control parameter γ, i.e the angular rotation of cylinder normalized by the freestream velocity, is increased the flow becomes asymmetric and simultaneously the pressure on the lower accelerated side of the cylinder decreases, resulting in a mean downward lift. There exists a transitional state i.e 'critical state' arising between the state representing the periodic alternate double side shed vortex pattern at lower values of γ to the steady state single side attached vortex shedding pattern occurring at higher values of γ (Badr et al., 1990, Chen et al., 1993, Lingg & Shih, 1999, Homescu et al., 2002).

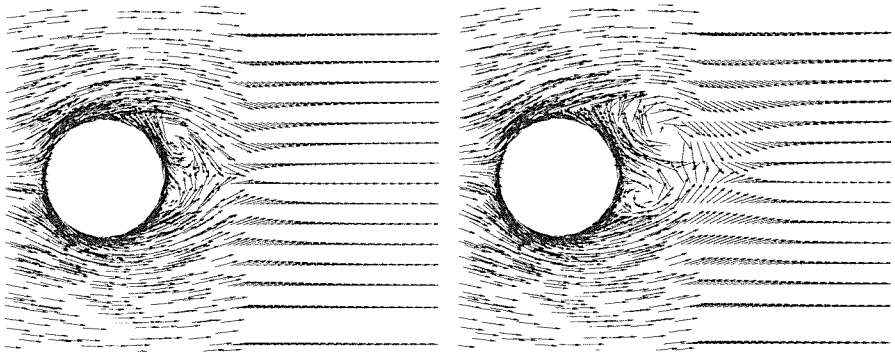

(a) $t = 1.0$sec (b) $t = 2.0$sec

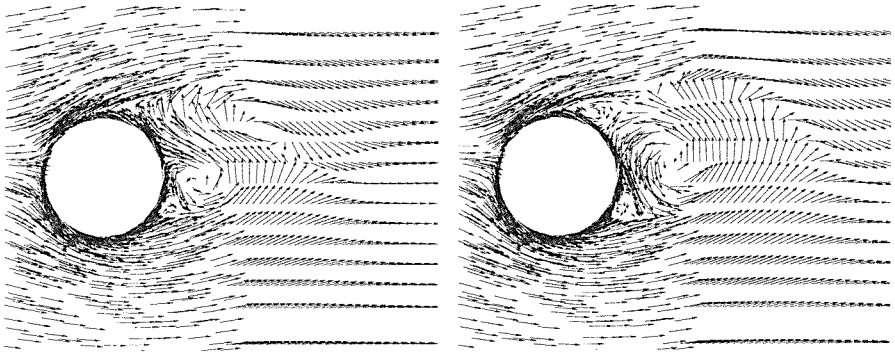

(c) $t = 3.0$sec (d) $t = 4.0$sec

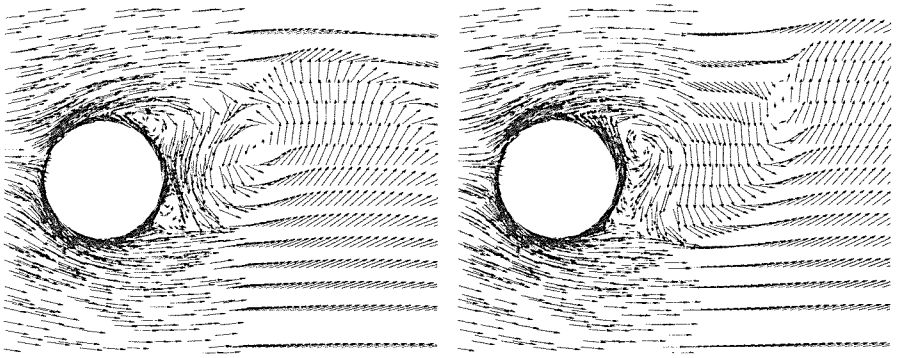

(e) $t = 5.0$sec (f) $t = 6.0$sec

Figure 3.2: Evolution of wake patterns behind an impulsively started isolated rotating cylinder from rest for angular rotation $\gamma = 1.0$ and $R_e = 200$. The patterns illustrated in (a)-(f) at different instantaneous events show similarities with the simulation results of Nair et al. (1998)

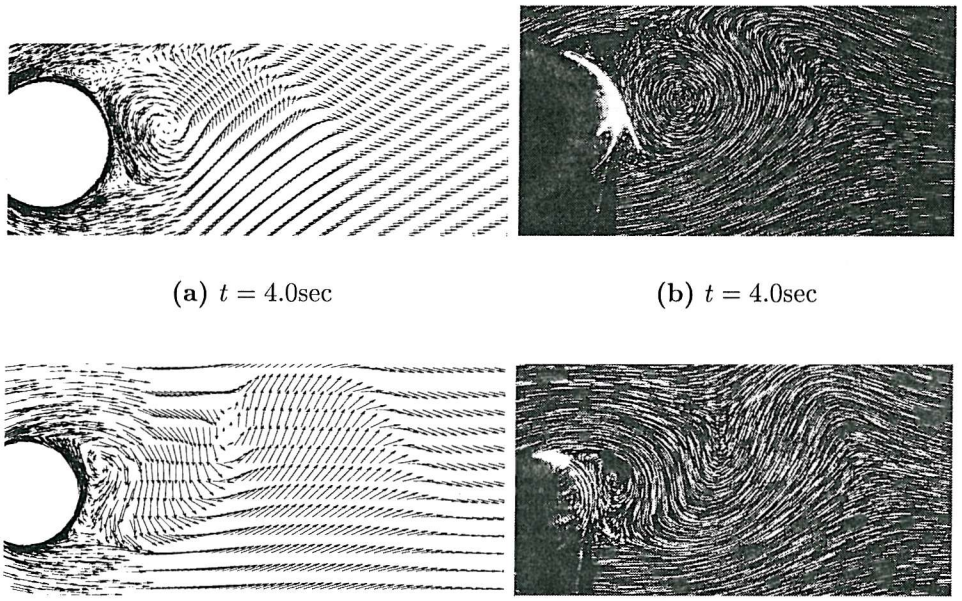

(a) $t = 4.0$sec (b) $t = 4.0$sec

(c) $t = 6.0$sec (d) $t = 6.0$sec

Figure 3.3: Comparison of wake patterns behind an impulsively started isolated translating and rotating cylinder ($\gamma = 1.0$ and $R_e = 200$). (a) & (c) Numerical Predictions (modified VCBEM); (b) & (d) Experimental observations (Coutanceau & Menard (1985))

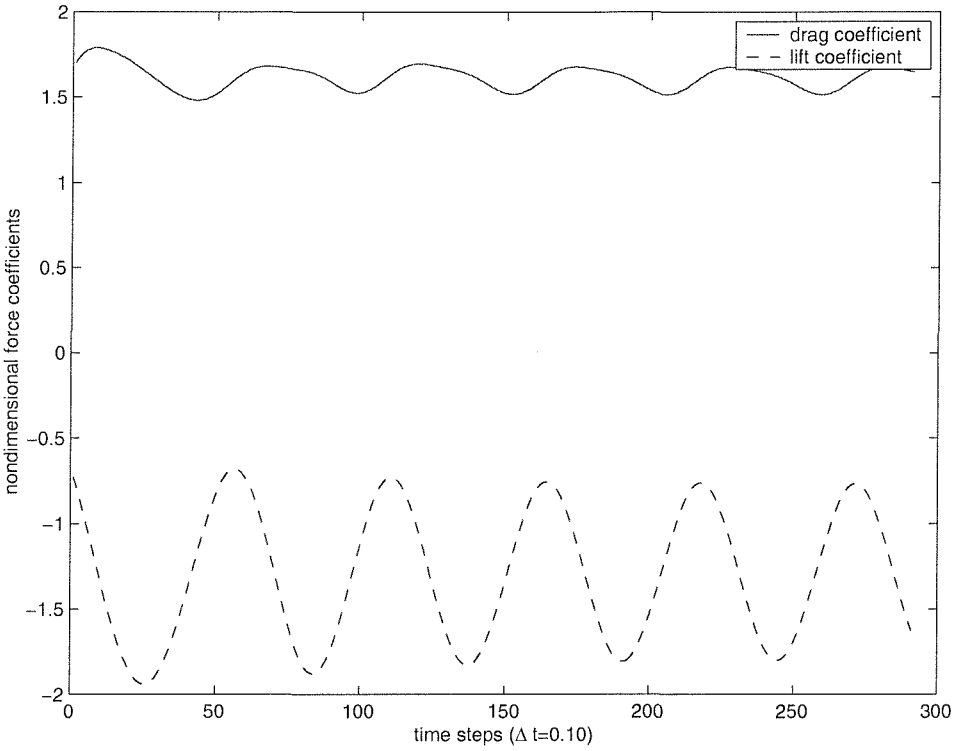

Figure 3.4: Lift C_l and drag C_d records with time illustrating the different characteristics for $R_e = 100$ and constant rate of angular rotation $\gamma = 1.0$, for isolated circulating cylinder

Figure 3.2 shows the evolution of the wake behind an isolated rotating cylinder for R_e=200 determined from the modified ($\gamma \neq 0$) VCBEM mathematical model. The process of evolution of vortices for R_e=200 shows similarities with the numerical simulations of Nair et al. (1998) and the experiments of Coutanceau & Menard (1985). In the experiments, the cylinder was impulsively set into translation and rotation and the early phase of wake development investigated by visualising the flow patterns with solid tracers. Figure 3.2 illustrates the flow topology and specifically the wake generated behind the isolated rotating cylinder and the flow separation patterns. Nair et al. (1998) studied numerically the two dimensional flow field generated by an infinitely long cylinder rotating about its axis and translating at right angles to its axis. The cylinder is assumed to attain rotational and translational speeds impulsively. The numerical simulations of Nair et al. (1998) were comparable with the simulations of Badr et al. (1990), Chen et al. (1993) and the experiments of Coutanceau & Menard (1985). The numerical studies of Badr et al. (1990) and Chen et al. (1993) dealt with the process of evolution of vortices at various instataneous events. Badr et al. (1990) validated with experimental results of Coutanceau & Menard (1985) and Chen et al. (1993) used explicit finite-difference/pseudospectral technique and Biot-Sauart law to

integrate a velocity/vorticity formulation of the Navier-Stokes equation. Temporal evolution of drag and lift co-efficients are presented by Chen et al. (1993) to larger dimensionless time to give more complete discussion of temporal development of wake.

The evolution of Magnus lift with γ is a complicated phenomenon in the case of real fluids due to the development of the boundary layer because of viscous forces. The Reynolds number is one of the main parameters which affects the flow along with other parameters such as surface conditions, aspect ratio, end shapes and wall confinement (Coutanceau & Menard, 1985). A review of the studies of Charrier (1979) and Calamote (1984) at high Reynolds number indicates a particular sensitivity to aspect ratio and so it was necessary for experimenters to investigate methods to approximate the two dimensional flow as discussed by Coutanceau & Menard (1985). It was found that the lift coefficient was independent of Reynolds number for $\gamma = 2.0$ (Swanson, 1961, Charrier, 1979, Calamote, 1984, Coutanceau & Menard, 1985).

The numerical simulations in the present study are undertaken by impulsively setting the rotation on the cylinder $\gamma = 1.0$ and a time step $\Delta t = 0.01$ is adopted to detail the flow topology. A detailed account of the flow topology is given by Coutanceau & Menard (1985). They proposed that the disintegration of symmetry due to rotation arises with the dissappearance of eddies on the lower side of the cylinder when it rotates in a counterclockwise direction. The existence of a thin layer of rotating fluid adjacent to the cylinder results in a shifting of the stagnation point and this is seen in the Figure 3.2. Proceeding with the time marching process (as in Figure 3.2(d)) the formation of an alleyway around the primary vortex is seen, which shows similarities with the simulation results of Nair et al. (1998) and the experiments of Coutanceau & Menard (1985).

The vortex shedding patterns arising from long term simulations of the flow regime for $R_e = 100$, $\gamma = 1$ are shown in the Figure 3.5. These predicted shedding patterns are similar to the shedding patterns illustrated by Homescu et al. (2002) for an isolated rotating cylinder. These authors used an adjoint formulation for the optimal control of the flow around the cylinder.

Another predominant characteristic of the flow is the synchronization of frequency of cylinder and wake, which yields a *lock-on* phenomenon. In the case of harmonic time rotary oscillations, this phenomenon was described experimentally by Tokumaru & Dimotakis (1991) and numerically by Chou (1997) and Dennis et al. (2000) who studied the wake flow patterns generated behind the cylinder for different forcing frequency and amplitude.

It was shown by Graham et al. (1999) that when forcing frequency lies in the neighbourhood of the Karman vortex shedding frequency, the combined system of

wake and cylinder creates a lock on phenomenon and He et al. (2000) reported this to be the optimal value for the forcing frequency for drag reduction. When the cylinder was driven by an angular velocity $\gamma = 2sin(2\pi t/6)$, close to the natural vortex shedding frequency (Graham et al., 1999) of 0.16, lock on phenomenon is observed due to the synchronisation of forcing and natural frequencies with large magnitude of amplitudes. The simulation results produced by the modified ($\gamma \neq 0$) VCBEM mathematical model for an isolated rotating cylinder are similar to the simulation results of Graham et al. (1999), who analysed the wake pattern into modal components. The evolution of modal amplitudes with time and projection of modal amplitudes is dealt in detail in Chapter 4, section 4.8.

It was shown by Homescu et al. (2002) that, when the natural frequency of vortex shedding is higher than the forcing frequency, an initial clockwise vortex is formed on the lower half of the cylinder when the cylinder rotates in a counterclockwise direction and a counterclockwise vortex is formed on the upper half when a clockwise rotation starts. This leads to a non-synchronized vortex formation mode which cannot lead to Karman vortex suppression.

When the forcing frequency is higher than the natural shedding frequency an initial reactive clockwise vortex is formed on the upper half of the cylinder when the cylinder is in counterclockwise rotation and a counterclockwise vortex is formed on the lower half when the clockwise rotation starts. This leads to a synchronized vortex mode for shedding suppression (Homescu et al., 2002).

Figure 3.5: Wake patterns generated behind isolated rotating cylinder for $R_e = 100$ and angular rotation $\gamma = 1.0$

3.4.3 Parametric studies

Parametric studies were performed for various angular rotation values γ of the cylinder at Reynolds number $R_e = 100$ and $R_e = 200$. Table 3.9 shows the relative comparison of mean drag and lift coefficients for $R_e = 100$. Results from the numerical simulation by modified VCBEM for $\gamma = 3.7, 3.8, 3.9, 4.0$ are tabulated in Table 3.9, which shows C_{lmean} to be a minimum for $\gamma = 3.8$. Studies were conducted with γ as a random variable with a mean value of 0.50 and this showed similarity with the time records of C_l and C_d for constant angular rotation $\gamma = 0.50$. The variation of drag and lift coefficients for different values of γ for $R_e = 100$ is shown in the Figures 3.6 and 3.7.

γ	C_{dmean}	C_{lmean}
0.50	1.6011	−1.2837
1.00	1.6209	−1.3004
3.00	1.5777	−1.2785
3.70	1.5857	−1.2946
3.80	1.6356	−1.2660
3.90	1.5827	−1.2957
4.00	1.5813	−1.2967
5.00	1.5493	−1.2871
10.0	1.4942	−1.2910
$2sin(2\pi t)$	1.6000	−1.2820
0.00	1.6152	0.0000

Table 3.9: Relative comparison of mean drag (C_{dmean}) and mean lift (C_{lmean}) for an isolated rotating cylinder, Reynolds number $R_e = 100$ and various angular rotations γ of the cylinder.

Table 3.10 shows a comparison for mean C_d and C_l values at $R_e = 100$ and $R_e = 200$ for stationary and $\gamma = 1.0$ cases. The variation of drag and lift coefficients for Reynolds number of flow $R_e = 100$ and $R_e = 200$ is shown in Figure 3.8. It is seen from Figure 3.8 that the variation of lift is higher for $R_e = 200$ and Farrant (1998) also reported from the research that symmetric separation bubble becomes unstable almost as soon as the uniform flow stream is established.

γ	R_e	C_{dmean}	C_{lmean}
1.0	100	1.6162	−1.2791
1.0	200	1.5866	−1.2746
0.0	100	1.6152	0
0.0	200	1.6286	0

Table 3.10: Mean drag (C_{dmean}) and mean lift (C_{lmean}) for an isolated rotating cylinder, Reynolds number $R_e = 100$ and $R_e = 200$, an angular rotation of the cylinder γ =1.0 compared to a stationary cylinder

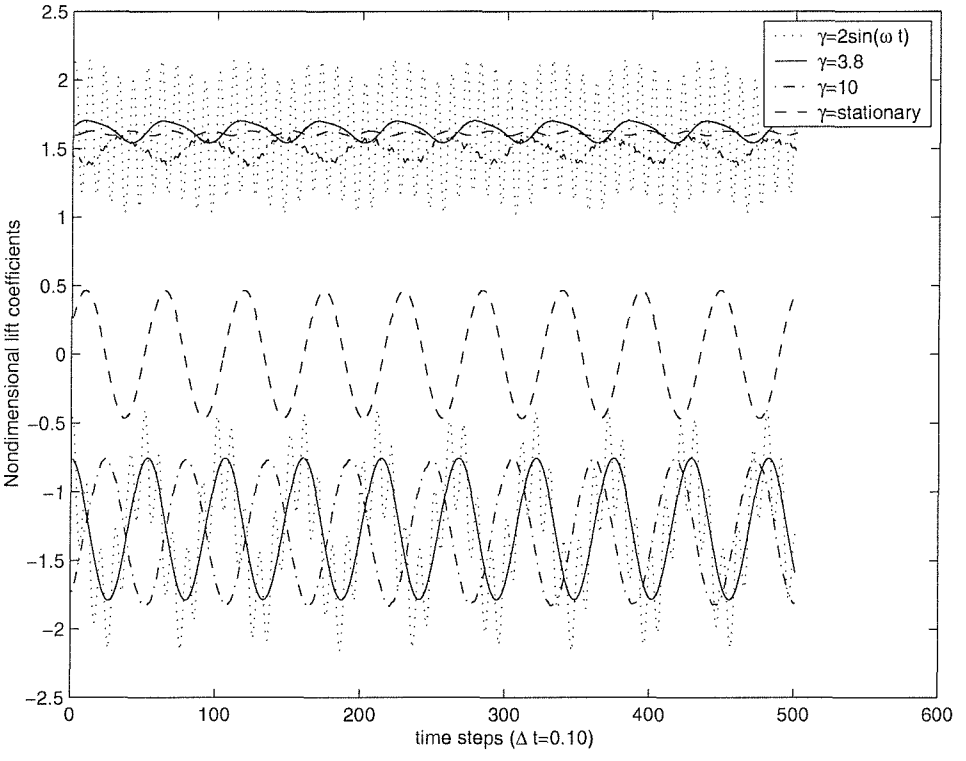

Figure 3.6: Lift C_l and drag C_d records with time illustrating the different characteristics for $R_e = 100$ and parametric angular rotation γ, for isolated rotating cylinder

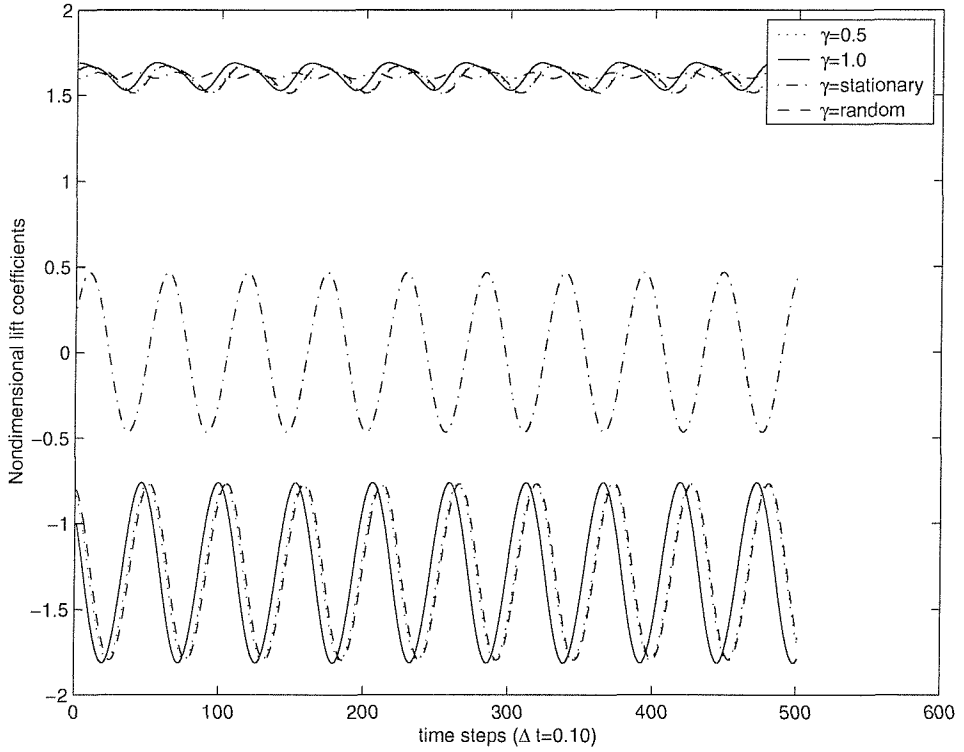

Figure 3.7: Lift C_l and drag C_d records with time illustrating the different characteristics for $R_e = 100$ and parametric angular rotation γ, for isolated rotating cylinder

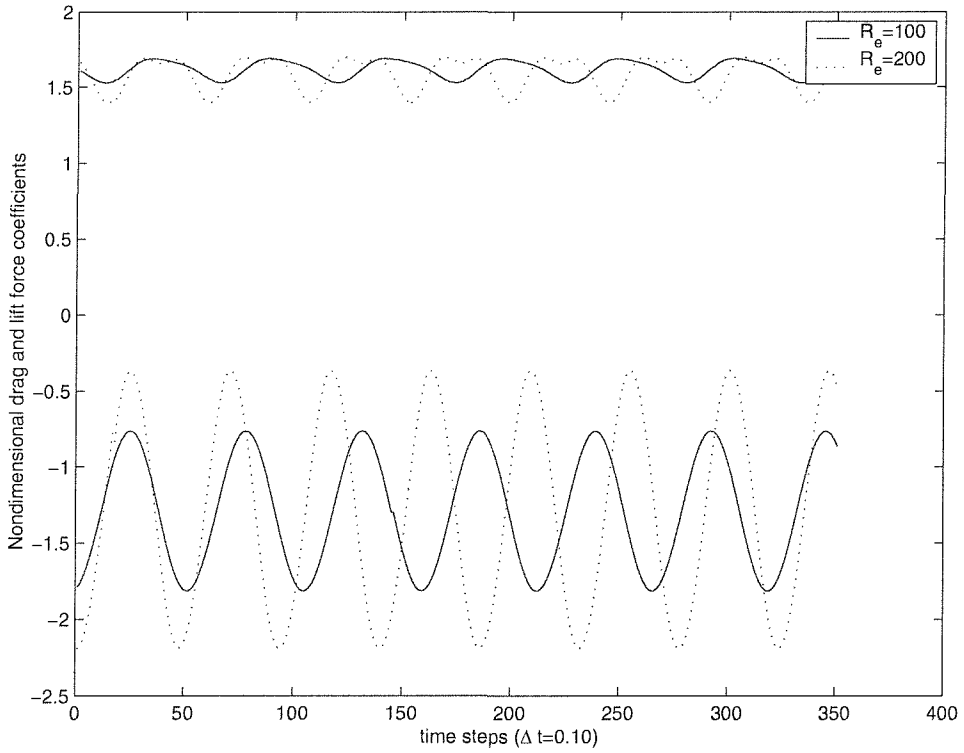

Figure 3.8: Lift C_l and drag C_d records with time illustrating the different characteristics for $R_e = 100$ and $R_e = 200$ for constant rate of angular rotation $\gamma = 1.0$, for isolated rotating cylinder

3.5 Twin Cylinders in Rotation

The flow interaction phenomenon arising in the cases of twin cylinders in co-rotation and counter rotation is examined for the following different arrangements:

I. Side-by-side (see Figures 3.9 and 3.11)

II. Tandem (see Figures 3.10 and 3.12)

The calculations presented are for Reynolds number $R_e = 100$ and $\gamma = 1.0$. A review of the effect of γ on the Magnus effect revealed that the lift coefficient is independent of Reynolds number from $\gamma = 2.0$ (Swanson, 1961, Charrier, 1979, Calamote, 1984, Coutanceau & Menard, 1985). From detailed studies of Uzunoglu et al. (2001) a computational domain of semi-length and semi-width $h = 9d$ is found sufficient for cases with mixed boundary conditions. These findings are incorporated in the present investigation and in the computations the upstream length and semi-width of the computational domain $h = 10d$ is adopted, whereas the downstream domain is taken as $50d$ so that an extensive wake flow pattern region is captured.

Incompressible viscous flow past two stationary parallel (i.e side-by-side) cylinders of equal diameter at a critical gap spacing g^* =0.90 to 1.10 investigated in Chapter 2 showed the dependence of vortex shedding patterns on the spacing factor, which also relates to the interaction mechanism and vortex shedding frequency. Investigation is herein further extended to twin rotating cylinders to detail the flow characteristics. Mittal (2001) using a finite element method investigated the problem to control flow past a circular cylinder using rotating control cylinders. Two dimensional numerical simulations were conducted with two rotating control cylinders for flow past the bluff body. Studies were conducted for different gaps between the main and control cylinders at Reynolds number $R_e = 100$ and $R_e = 10^4$. Computations were initiated to determine steady-state solutions for the principal and control cylinders and the flow was perturbed by the rotating control cylinders at different angular velocity values $\gamma = 1.0, 2.0, \ldots, 5.0$. Studies showed that the effect of gap is found to be more critical at $R_e = 10^4$ than at lower Reynolds number and also the power required to rotate the control cylinders is significant at lower Reynolds number but negligible for a relatively higher Reynolds number $R_e = 10^4$ (Mittal, 2001).

The rotating cylinders each of diameter d are spaced centre to centre distance $2d$. The gap spacing ratio between the cylinders $g^* = 1.0$ is maintained in both the co-rotation and counter rotation cases when the cylinders are in side-by-side or tandem arrangements. An anti-clockwise rotation denotes a positive value of γ. Tables 3.11 and 3.12 give the relative comparison of mean drag (C_{dmean}) and mean lift

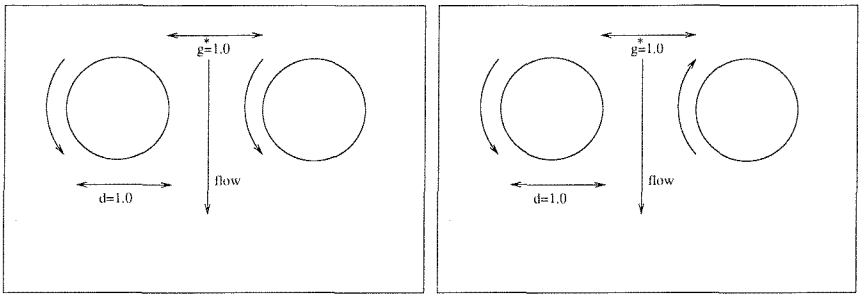

(a) co-rotation **(b)** counter rotation

Figure 3.9: Schematic diagram of rotation of twin cylinders in side-by-side arrangement

(C_{lmean}) forces for twin rotating cylinders in side-by-side and tandem arrangements respectively, for angular velocity of $\gamma = 1.0$, $R_e = 100$.

3.5.1 Side-by-side arrangement

In the Figure 3.11(a) the left cylinder rotates in the counter clockwise direction with the same angular velocity $\gamma = 1.0$ as the right cylinder for co-rotation case whereas for the case of counter rotation in Figure 3.11(b), right cylinder rotates in clockwise direction and left cylinder rotates in counter clockwise direction. The arrangement of cylinders and the directions of rotation is represented in a schematic diagram shown in Figure 3.9.

Cylinders in co-rotation

The wake patterns generated behind twin cylinders of equal diameter in co-rotation in a side-by-side arrangement are shown in Figure 3.11(a). The cylinders rotate in a counter clockwise direction with the same angular velocity $\gamma = 1.0$. The figure clearly shows the development of vortices downstream of the cylinders. The left rotating cylinder drags the flow from its left side to its right side and in a similar manner so does the right cylinder. In case of co-rotation, the flow between the cylinders experience the counteracting forces from the rotating cylinders and generates a wake in contrast to counter rotation where there is a thorough mixing. These patterns of co-rotation vortex shedding show less mixing with the merging of vortices to produce a tighter spatial wake in comparison to the counter rotation case shown in Figure 3.11(b). This affect is also seen from Figures 3.13 and 3.14 where the periods of drag and lift forces are longer than generated in the counter rotation case illustrated in Figures 3.15 and 3.16 for left

Characteristics	Right Cylinder		Left Cylinder	
	Co-rotation	Counter rotation	Co-rotation	Counter rotation
C_{dmean}	2.32	3.53	1.24	0.78
C_{lmean}	-5.88	-0.78	-2.69	-3.35
Nature of forces	High	Low	Low	High
Figure no.	3.13	3.15	3.14	3.16

Table 3.11: Relative comparison of mean drag (C_{dmean}) and mean lift (C_{lmean}) for twin cylinders in rotation with angular velocity $\gamma = 1.0$, Reynolds number R_e=100 in a side-by-side arrangement

Characteristics	Upstream Cylinder		Downstream Cylinder	
	Co-rotation	Counter rotation	Co-rotation	Counter rotation
C_{dmean}	2.20	2.19	-1.06	-1.41
C_{lmean}	-5.89	-5.79	-20.39	-20.04
Nature of forces	High	Low	High	Low
Figure no.	3.17	3.19	3.18	3.20

Table 3.12: Relative comparison of mean drag (C_{dmean}) and mean lift (C_{lmean}) for twin cylinders in rotation with angular velocity $\gamma = 1.0$, Reynolds number R_e=100 in a tandem arrangement

and right cylinders respectively. When compared to the case of an isolated cylinder in rotation, mean forces is approximately two to three times that of the isolated cylinder case and the interactive force between the two cylinders is considerable.

Cylinders in counter rotation

The left hand side cylinder in Figure 3.11(b) rotates in a counter clockwise direction whilst the right hand side cylinder has a clockwise rotation. Both cylinders rotate with the same angular velocity. The shedding pattern shown in Figure 3.11(b) indicates a strong mixing and the wake is more spread and diffused, in contrast to the co-rotation case shown in Figure 3.11(a). A strong mixing of vortices is seen even further downstream. In Figures 3.15 and 3.16, a large variation in the lift and drag forces is observed for left and right cylinders respectively, even though they are periodic. Also, the frequency of the drag and lift forces is higher than the frequency found in the co-rotation case. The drag shows two predominant peaks in a cycle contrasting with the single peak observed in co-rotation case. The lift force magnitude also shows a much higher variation when compared to the co-rotation case.

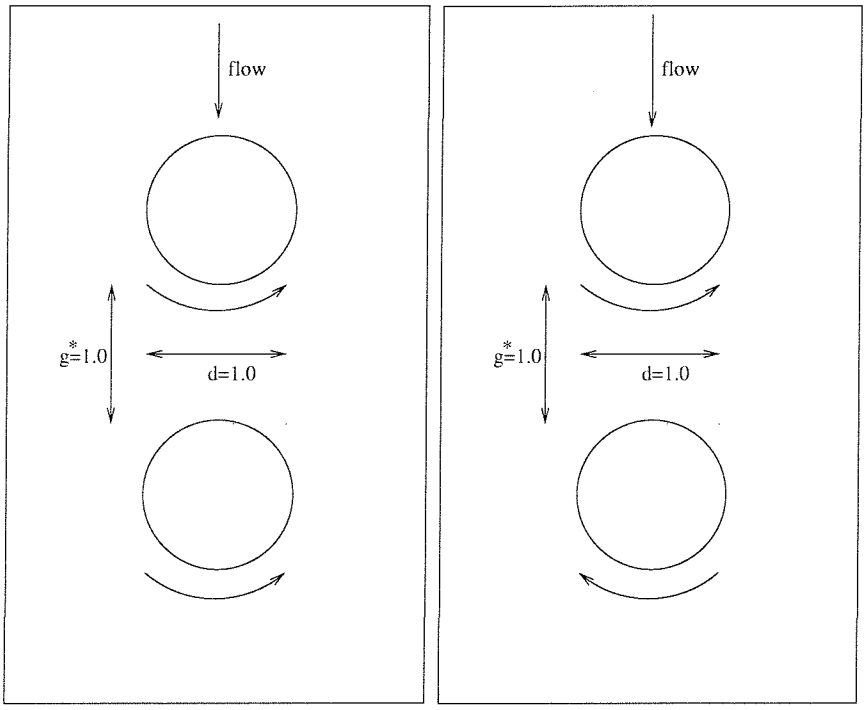

(a) co-rotation (b) counter rotation

Figure 3.10: Schematic diagram of rotation of twin cylinders in tandem arrangement

3.5.2 Cylinders in tandem arrangement

In Figure 3.12(a) the top cylinder rotates in a counter clockwise direction with the same angular velocity $\gamma = 1.0$ as the bottom cylinder for co-rotation case whereas for counter rotation Figure 3.12(b), bottom cylinder rotates in clockwise direction and top cylinder rotates in counter clockwise direction. The arrangement of cylinders and direction of rotation is represented in a schematic diagram shown in Figure 3.10.

Cylinders in co-rotation

In the co-rotation situation, the wake patterns generated behind the twin cylinders of equal diameter are shown in Figure 3.12(a). The development of vortices downstream of the cylinders is clearly illustrated with a thorough mixing of vortices downstream observed and the wake generated is spread and diffused. Figures 3.17 and 3.18 illustrate the lift and drag forces experienced on the upstream and downstream cylinders respectively. As seen from the Figure 3.18, the downstream cylinder experiences a negative drag and the upstream cylinder experiences a positive drag as shown in Fig-

ure 3.17. This indicates that the cylinders are attracted towards each other, this is explained physically by the high velocity of the flow between the cylinders with the development of a suction force. The results also show a high magnitude of lift force and a low magnitude of drag force both with less variation about the mean.

Cylinders in counter rotation

Figure 3.12(b) shows the wake patterns generated behind the twin cylinders of equal diameter in counter rotation. It is seen from Figure 3.12(b) that there is a thorough mixing of vortices downstream and the wake generated is spread and diffused. The shedding patterns are distinct in contrast to the findings observed in the co-rotation case. In co-rotation, the axis of shedding is shifted in the direction of the rotation but in the counter rotation case the effect of the downstream cylinder counter acts the vortices convected downstream from the cylinder. Initially, the upstream cylinder dominates the flow compared to the downstream cylinder. This is visible by the shift of the path of the vortices near to the downstream cylinder and they cross the axis of the cylinder demonstrating the increasing influence of the downstream cylinder as the vortices convect further downstream.

Figure 3.20 shows that the downstream cylinder experiences a negative drag and the upstream cylinder experiences a positive drag as illustrated in Figure 3.19. This indicates that the cylinders are attracted towards each other which is explained physically by the high velocity of the flow between the cylinders and the development of a suction force. A high magnitude of lift force and a low magnitude of drag force are generated both with less variation about the mean. The variation of drag and lift forces for both the upstream and downstream cylinders for the counter rotation case are similar to those experienced in the co-rotation case, with magnitudes smaller than that experienced for co-rotation. This is explained by the physics of the system, where in the counter rotation case counteractive effects on the force cause a smaller magnitude in the resultant forces.

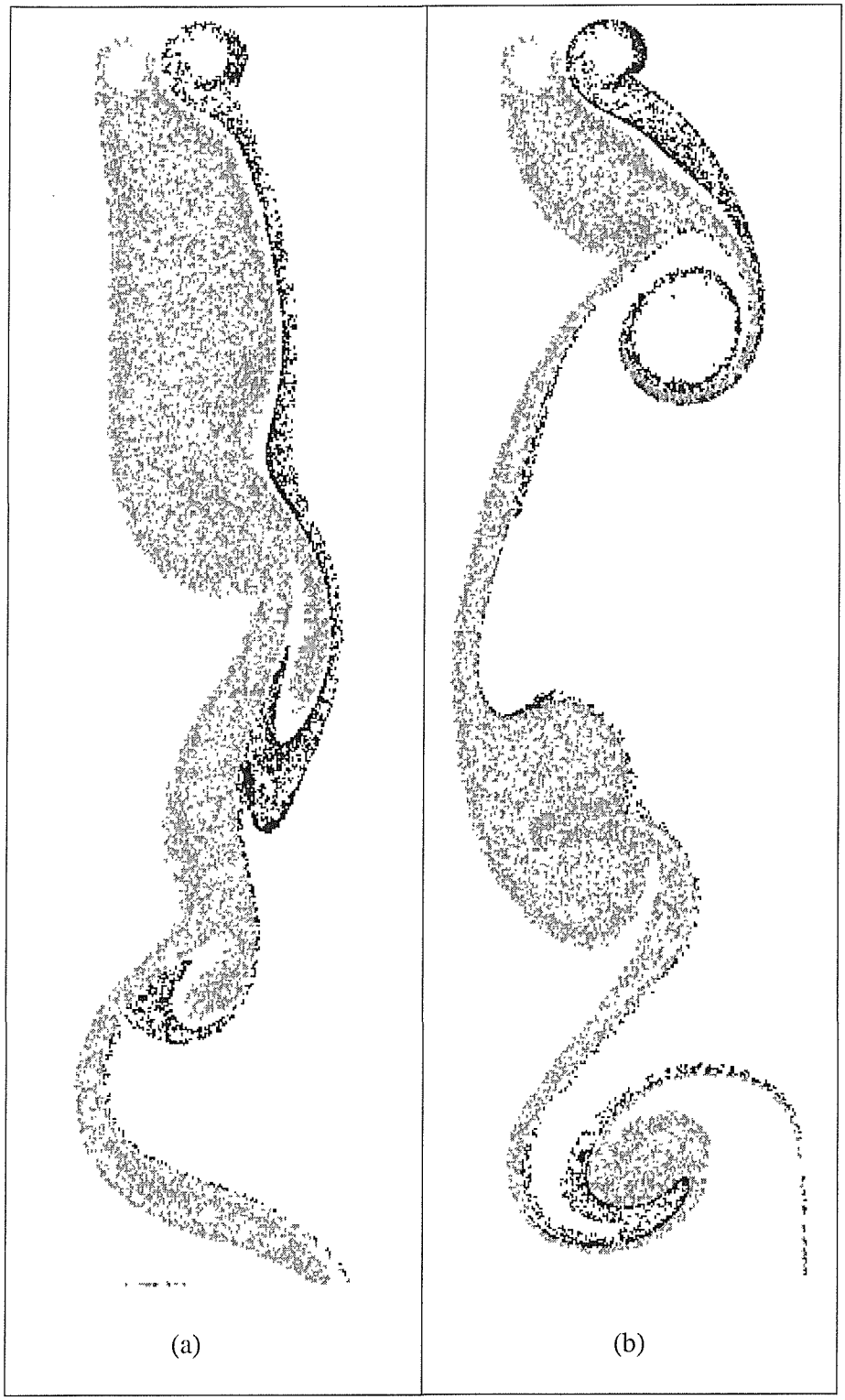

Figure 3.11: Wake patterns generated behind side-by-side cylinders of equal diameter, $R_e = 100$ and angular rotation γ =1.0. (a) co-rotation (b) counter rotation

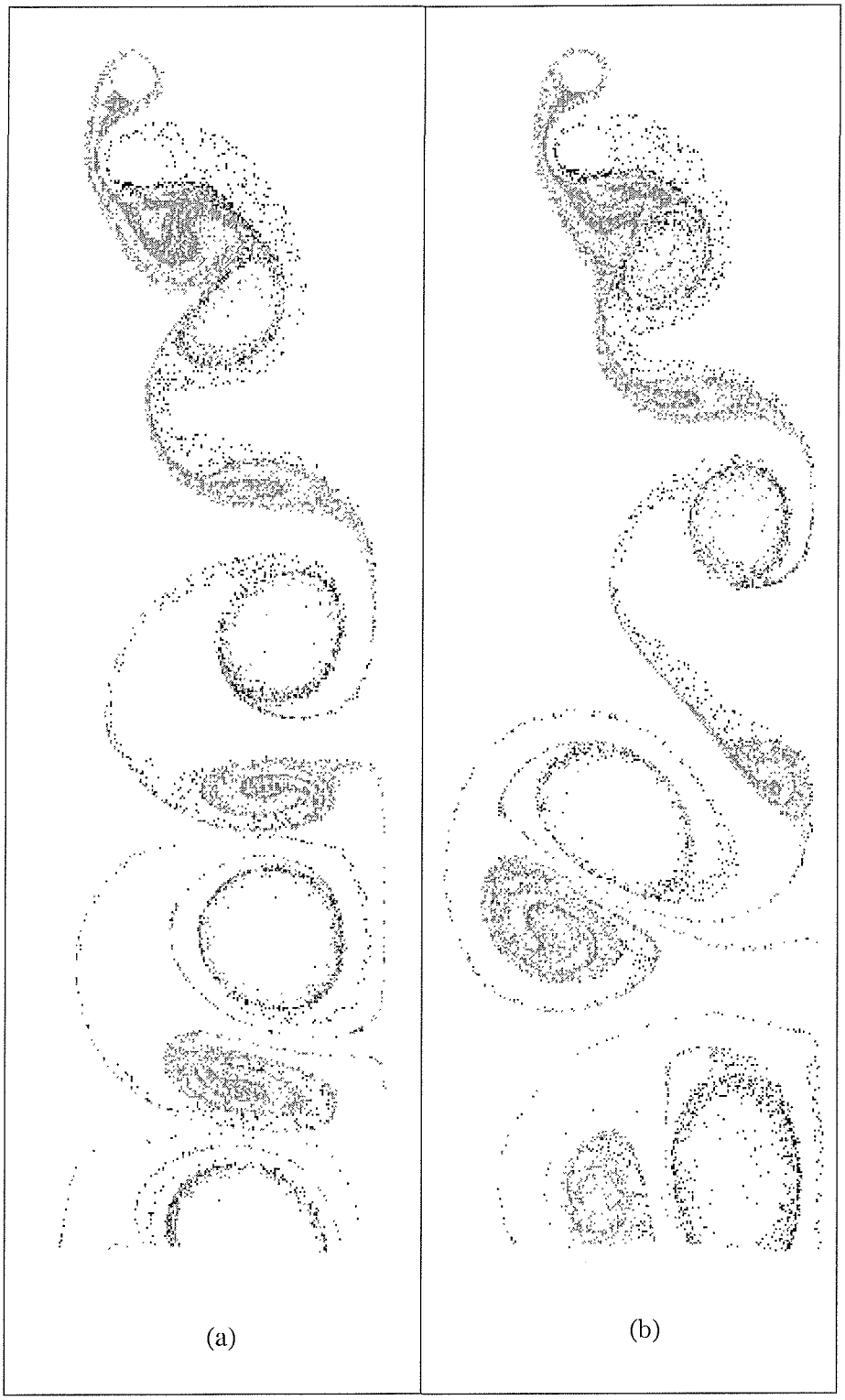

Figure 3.12: Wake patterns generated behind twin tandem cylinders of equal diameter for (a) co-rotation (b) counter rotation, R_e = 100 and angular rotation γ =1.0

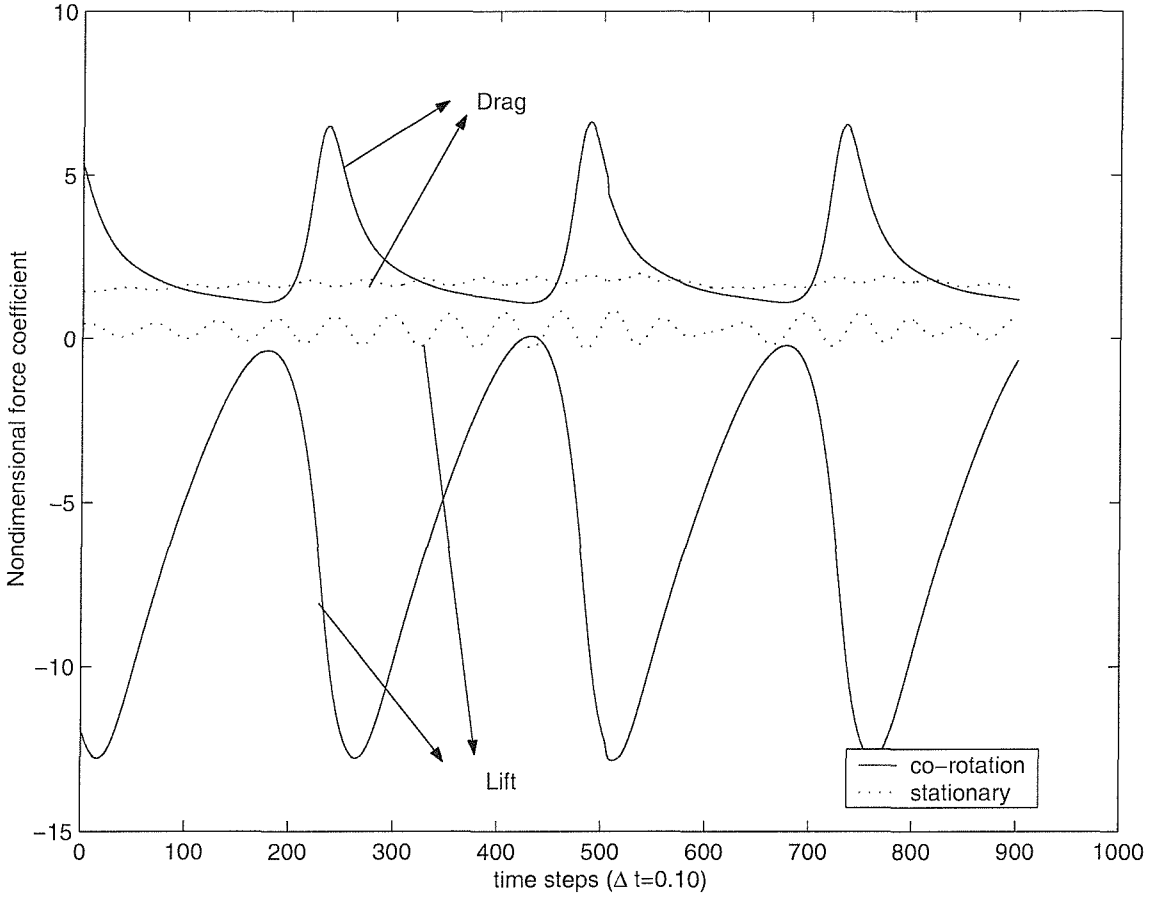

Figure 3.13: Lift C_l and drag C_d records with time for right hand side cylinder in side-by-side arrangement, g^* =1.0. This illustrates the different characteristics for co-rotation of twin cylinders of equal diameter for $R_e = 100$ and angular rotation γ =1.0 in comparison to corresponding twin stationary cylinders

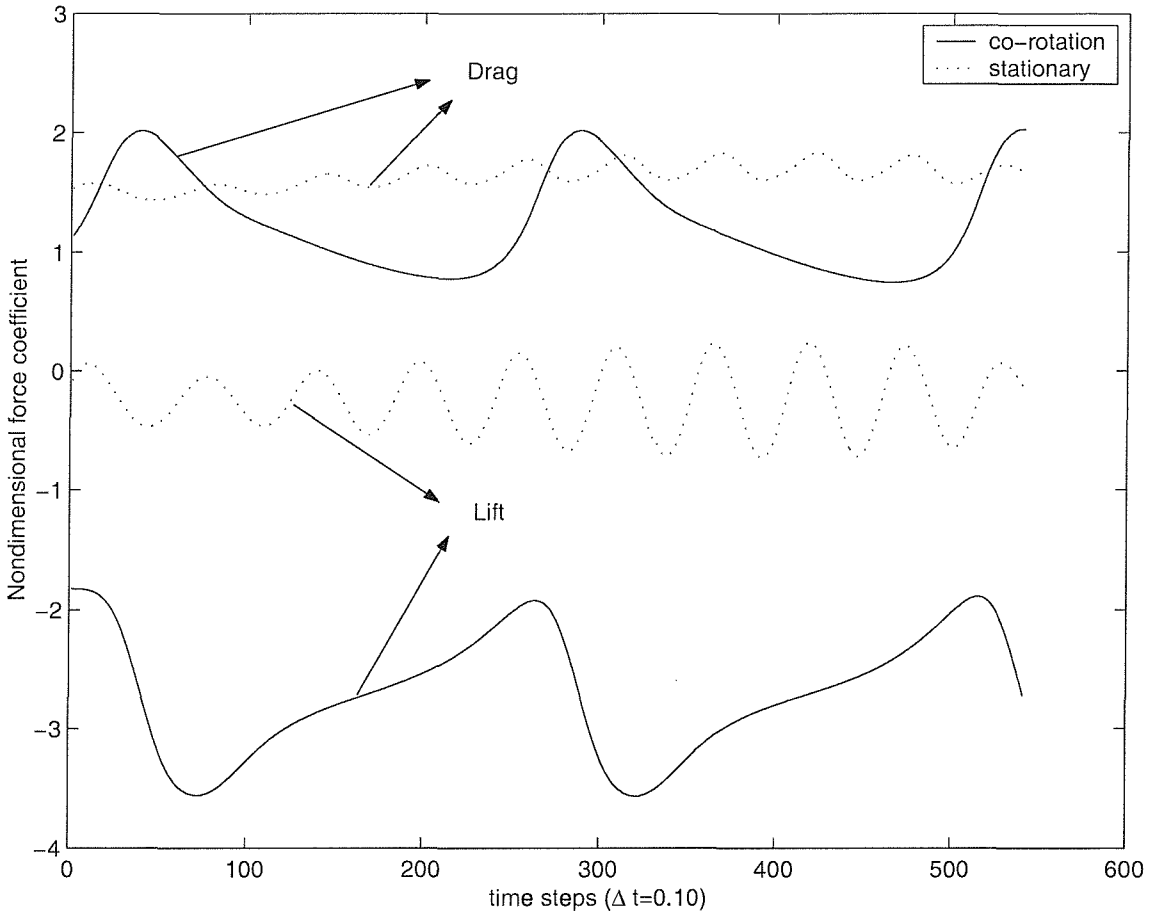

Figure 3.14: Lift C_l and drag C_d records with time for left hand side cylinder in side-by-side arrangement, g^* =1.0. This illustrates the different characteristics for co-rotation of twin cylinders of equal diameter for $R_e = 100$ and angular rotation γ =1.0 in comparison to corresponding twin stationary cylinders

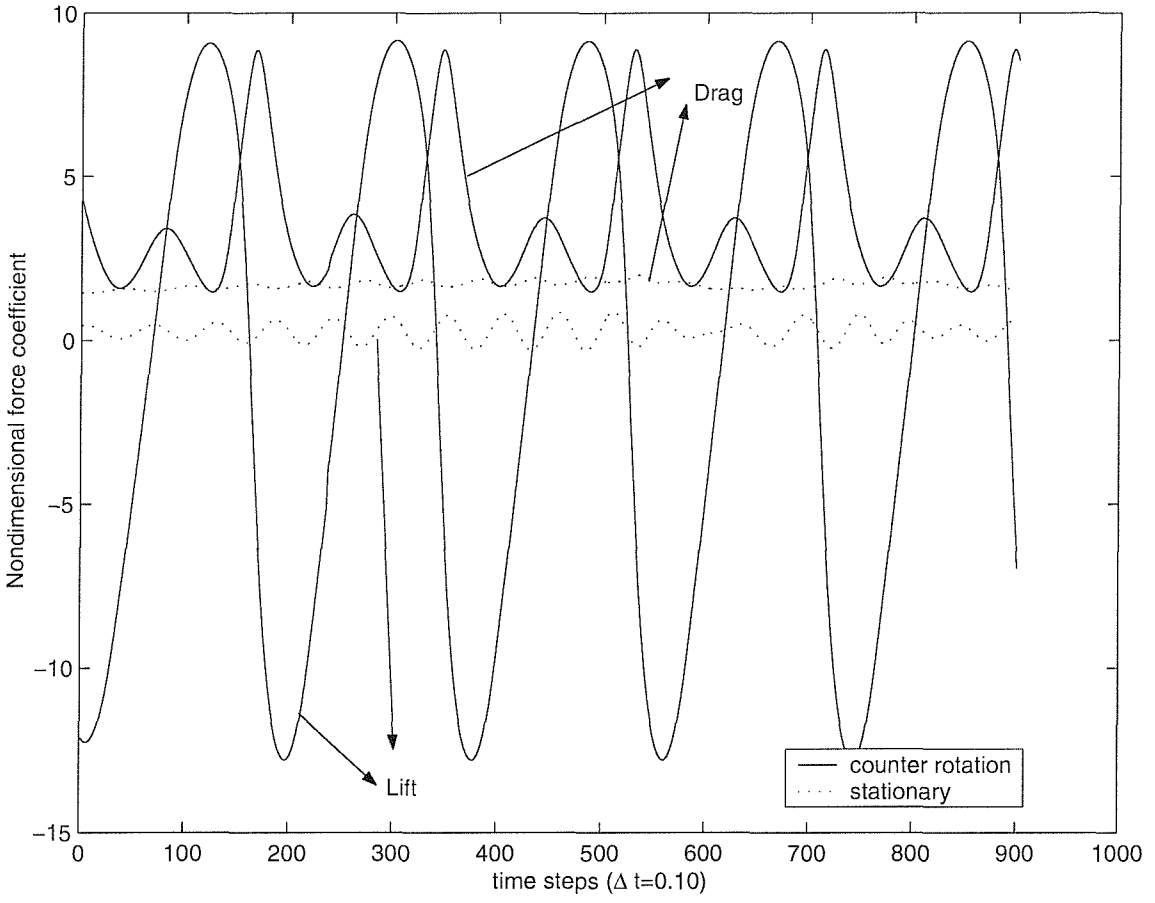

Figure 3.15: Lift C_l and drag C_d records with time for right hand side cylinder in side-by-side arrangement, g^* =1.0. This illustrates the different characteristics for counter rotation of twin cylinders of equal diameter for R_e = 100 and angular rotation γ =1.0 in comparison to corresponding twin stationary cylinders

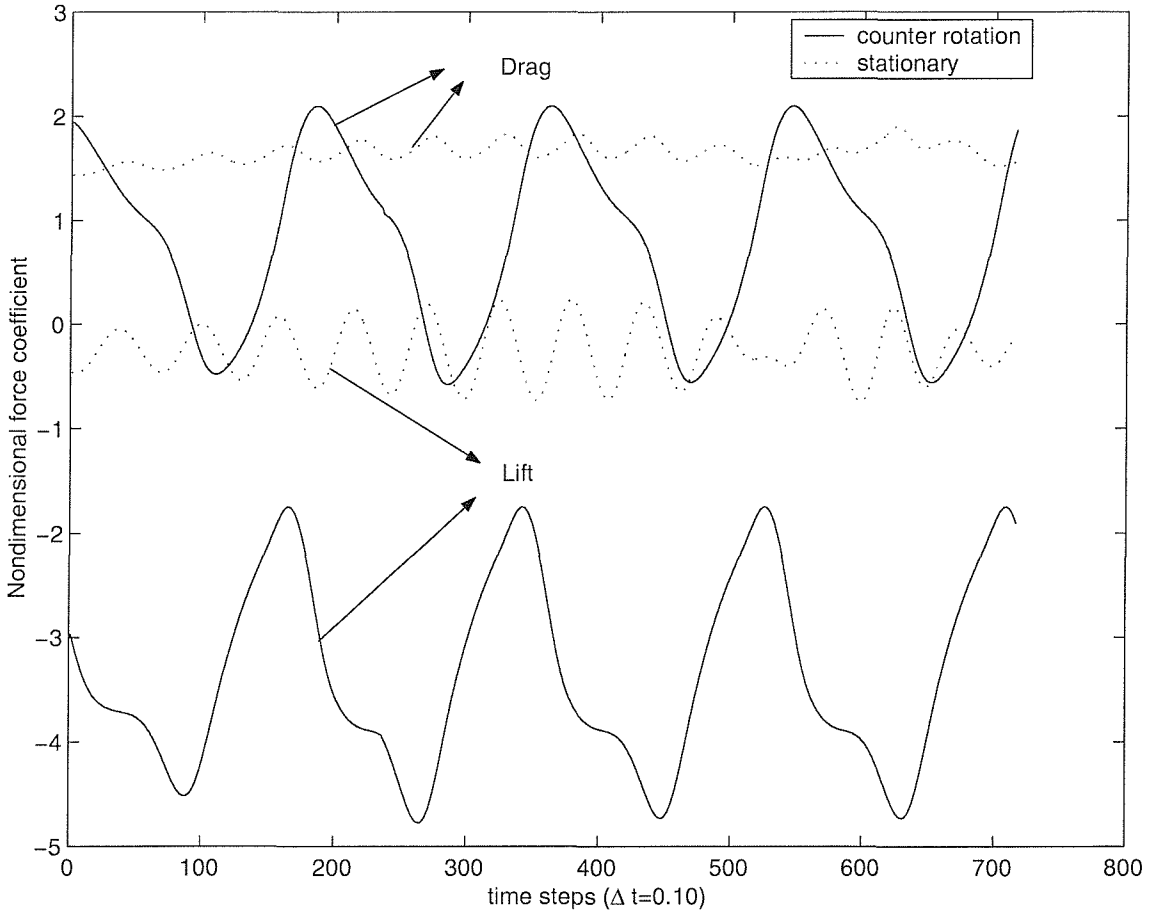

Figure 3.16: Lift C_l and drag C_d records with time for left hand side cylinder in side-by-side arrangement, g^* =1.0. This illustrates the different characteristics for counter rotation of twin cylinders of equal diameter for R_e = 100 and angular rotation γ =1.0 in comparison to corresponding twin stationary cylinders

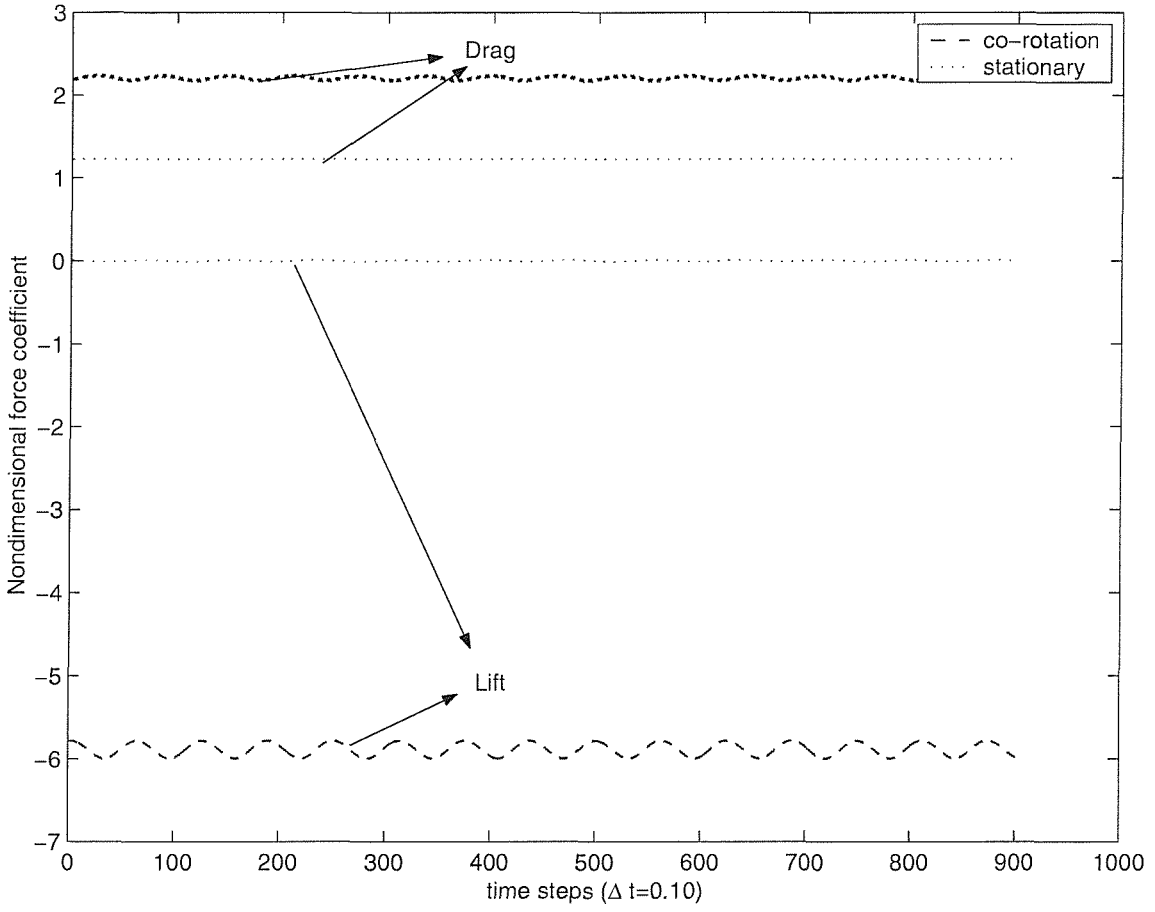

Figure 3.17: Lift C_l and drag C_d records with time illustrating the different characteristics experienced by upstream twin tandem cylinder in co-rotation, g^* =1.0, R_e = 100 and angular rotation γ =1.0 in comparison to corresponding twin stationary cylinders

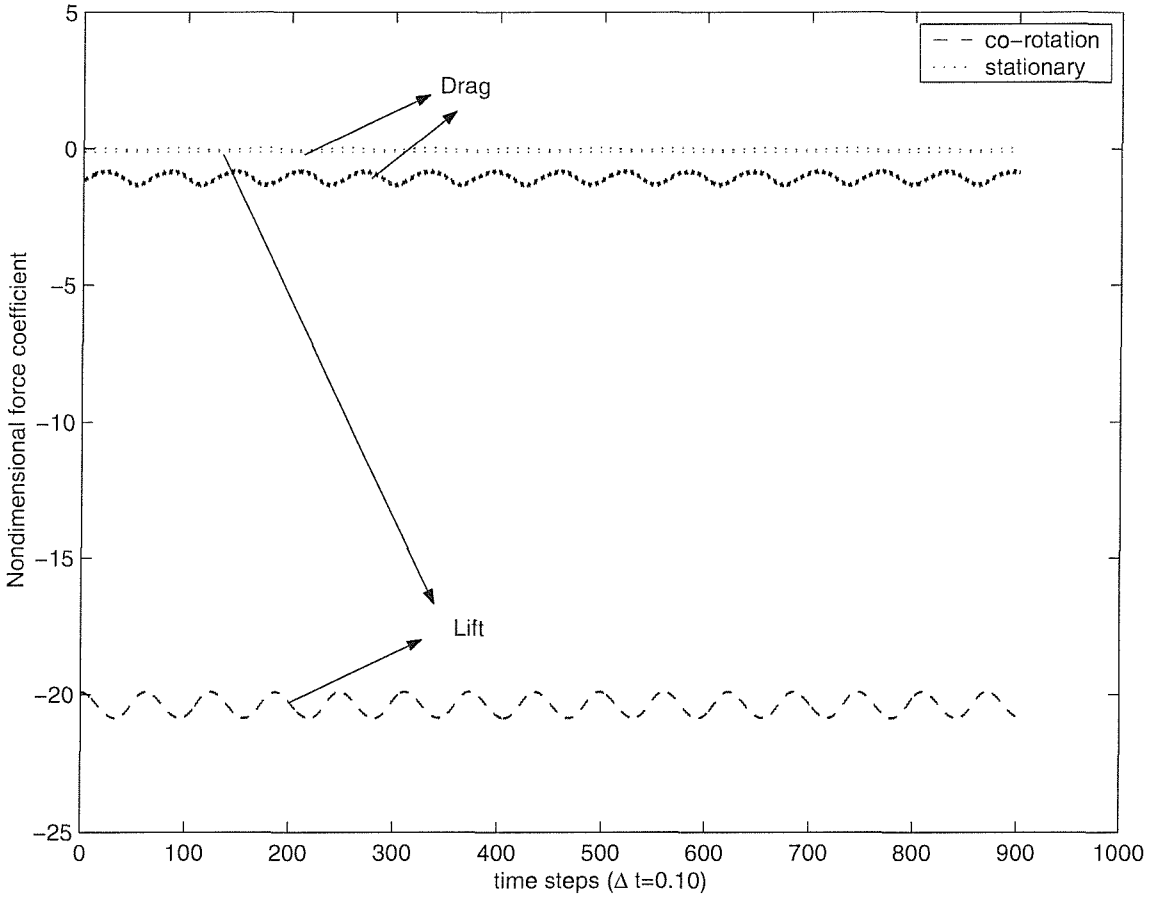

Figure 3.18: Lift C_l and drag C_d records with time illustrating the different characteristics experienced by downstream twin tandem cylinder in co-rotation, g^* =1.0, R_e = 100 and angular rotation γ =1.0 in comparison to corresponding twin stationary cylinders

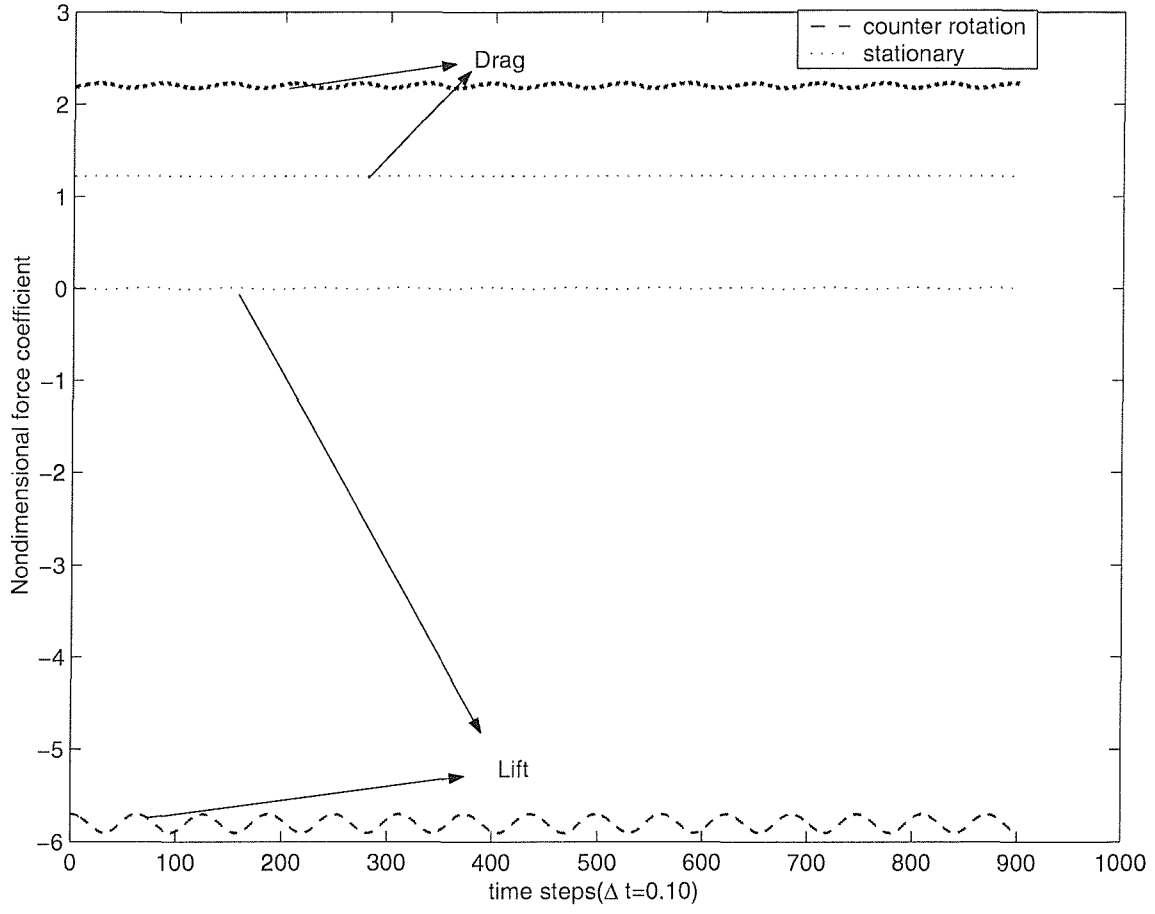

Figure 3.19: Lift C_l and drag C_d records with time illustrating the different characteristics experienced by upstream twin tandem cylinder in counter rotation, g^* =1.0, R_e = 100 and angular rotation γ =1.0 in comparison to corresponding twin stationary cylinders

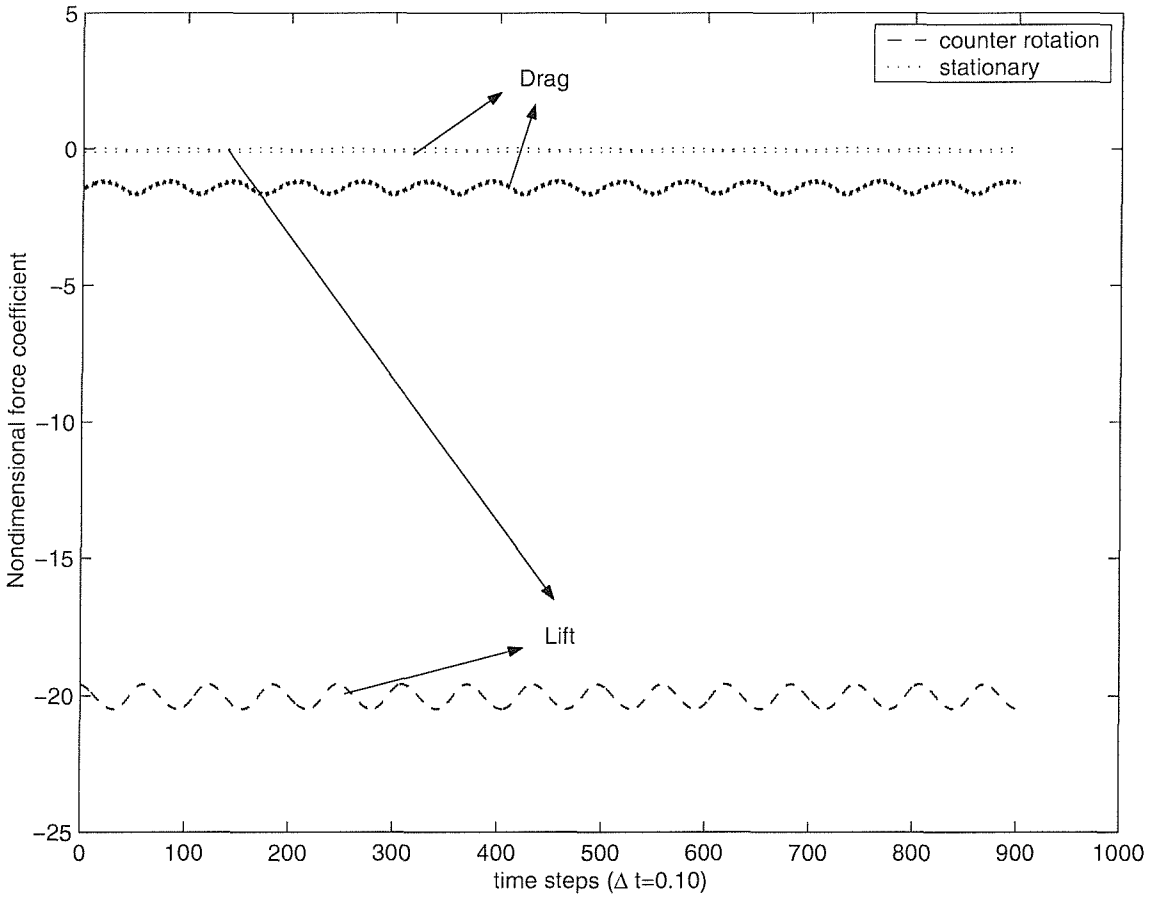

Figure 3.20: Lift C_l and drag C_d records with time illustrating the different characteristics experienced by downstream twin tandem cylinder in counter rotation, g^* =1.0, R_e = 100 and angular rotation γ =1.0 in comparison to corresponding twin stationary cylinders

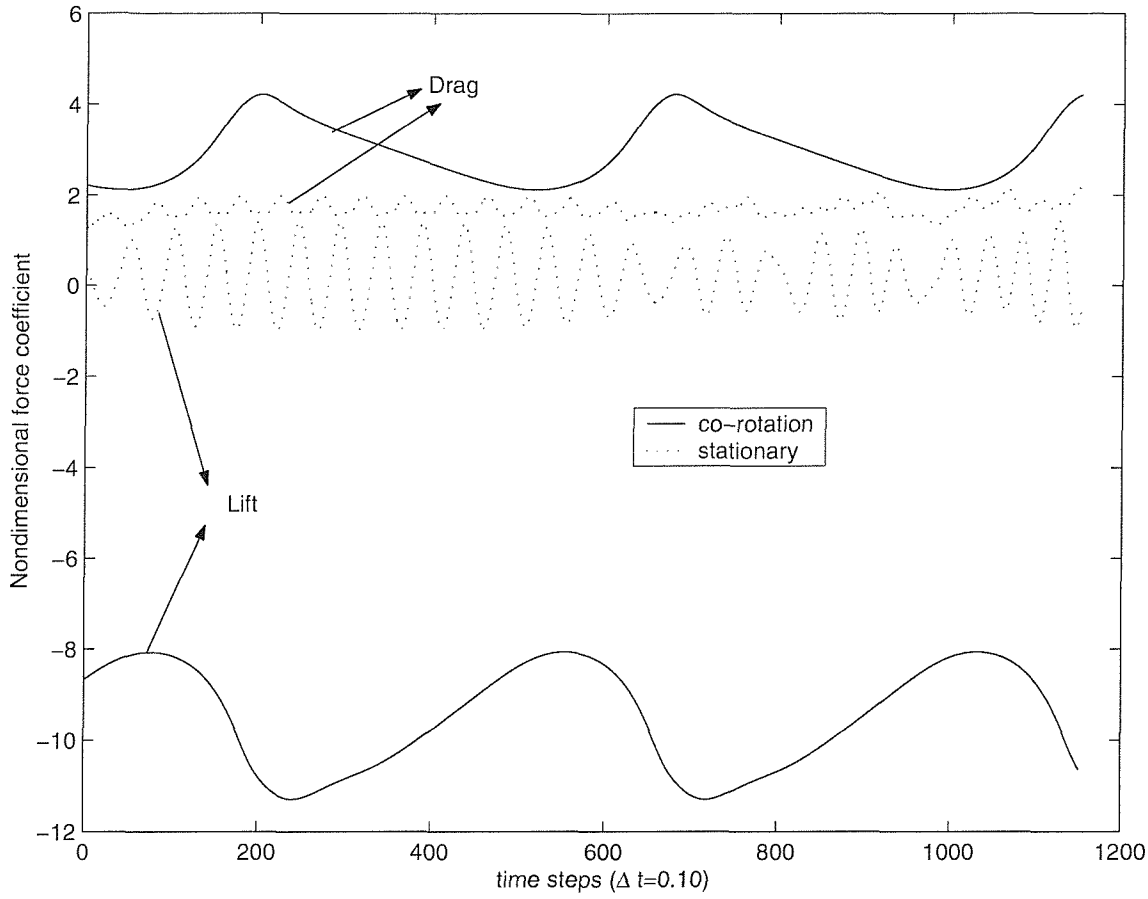

Figure 3.21: Lift C_l and drag C_d records with time for right hand side cylinder in side-by-side arrangement, g^* =1.0. This illustrates the different characteristics for co-rotation of twin cylinders of equal diameter for, R_e = 200 and angular rotation γ =1.0 in comparison to twin stationary cylinders

3.5.3 Twin cylinders in rotation: $R_e = 200$

In order to study the behaviour of twin cylinders in different flow regimes, simulations were carried out for R_e = 200 in various configurations of cylinders as in side-by-side and tandem arrangements. The simulation of C_l and C_d records are shown in the Figures 3.21 and 3.22 for right and left cylinders respectively in side-by-side arrangement and Figures 3.23 and 3.24 for tandem arrangement of upstream and downstream cylinders respectively. The findings are compared to their corresponding stationary cases. From the figures the effect of rotation on the drag and lift, coupled with the interaction effect between the cylinders on the forces is observed. The variation of forces R_e = 200 show similarity to nature of corresponding forces developed in the case of R_e = 100 but with a lesser magnitude of forces.

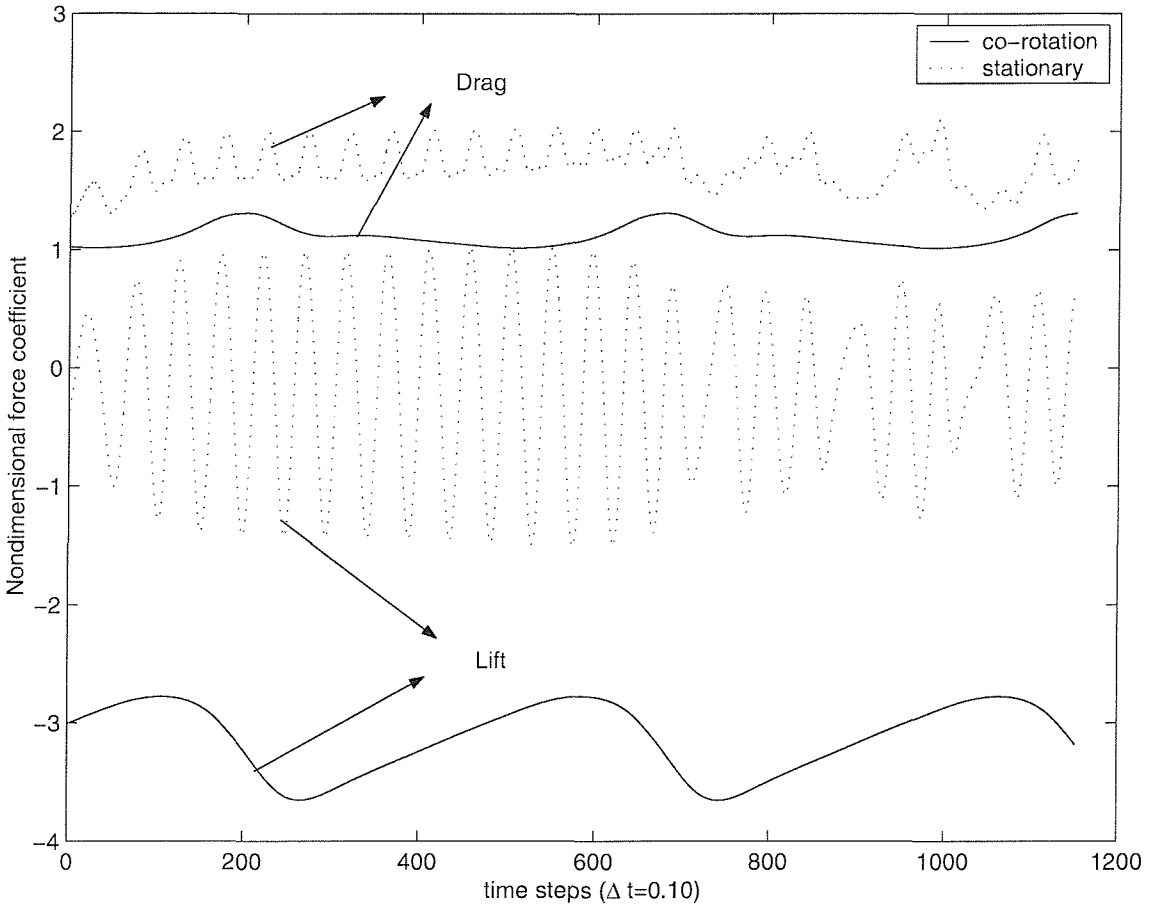

Figure 3.22: Lift C_l and drag C_d records with time for left hand side cylinder in side-by-side arrangement, g^* =1.0. This illustrates the different characteristics for co-rotation of twin cylinders of equal diameter for, R_e = 200 and angular rotation γ =1.0 in comparison to twin stationary cylinders

3.6 Discussion of Results

Tables 3.11 and 3.12 show the magnitudes of mean drag (C_{dmean}) and mean lift (C_{lmean}) forces predicted for R_e=100 in side-by-side and tandem arrangements at angular velocity of rotation γ=1.0. There are some high lift coefficients present in these tables. The mean lift coefficients of the order of 5-6 are seen apart from the lift coefficients of downstream tandem cylinder. The similar values of lift coefficients of order 6-8 are reported in the studies of Nair et al. (1998) for rotating single cylinder case for higher Reynold number of 3800. Lift coefficients of the order of 3 are reported in the works of Badr et al. (1989) for unsteady flow past single rotating cylinder at Reynolds number of 100. Also it is reported in Badr et al. (1990) that for Reynold number 1000 and higher rotational rates $C_l > 8$ and increases with the rotational rate.

In light of the above listed works, results reported in current research for two cylin-

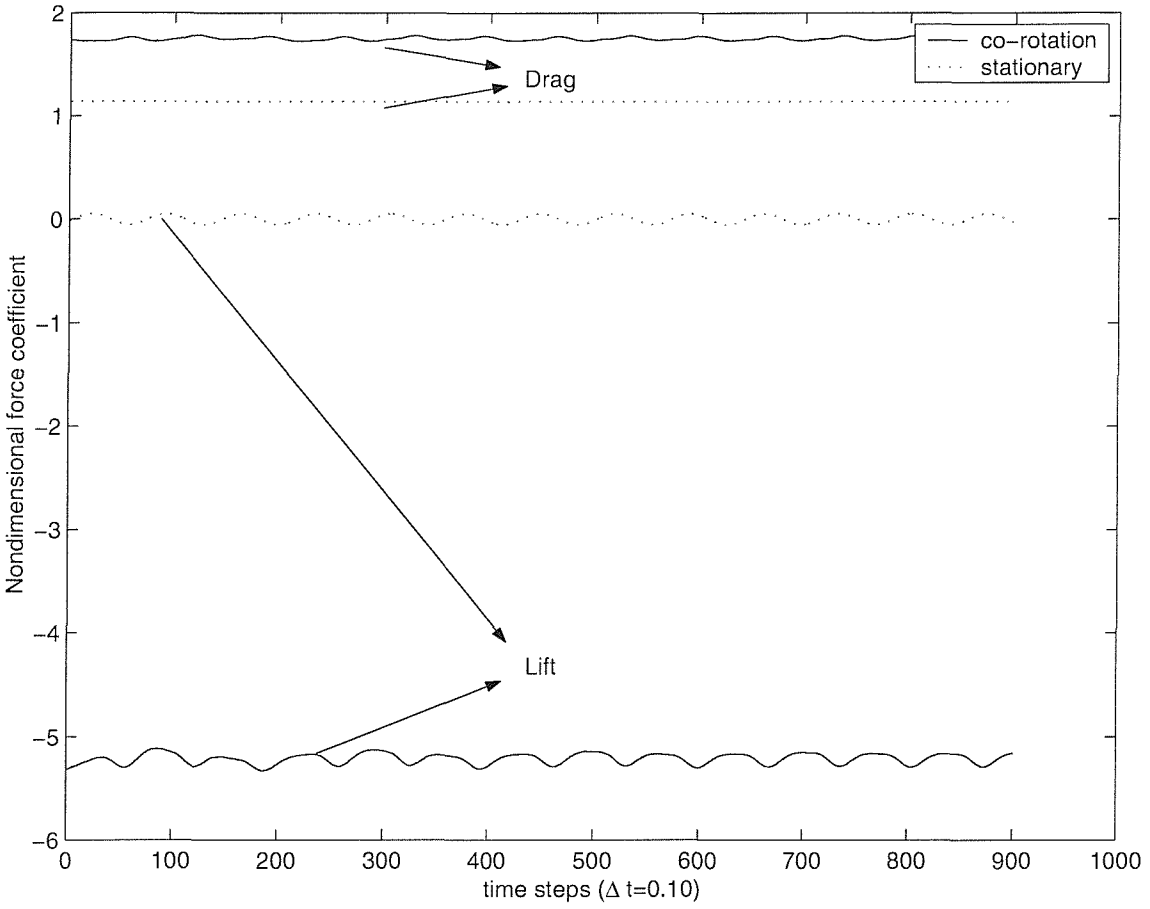

Figure 3.23: Lift C_l and drag C_d records with time illustrating the different characteristics experienced by the upstream twin tandem cylinder in co-rotation, g^* =1.0, R_e = 200 and angular rotation γ =1.0 in comparison to twin stationary cylinders

der case involve interaction between the cylinders and this might have some effect on the increased magnitude of lift co-efficient. However, higher values of C_l are found for downstream cylinder in tandem arrangement which experience a suction force owing to the interaction between the cylinders. Further validation is needed to verify these values. Figures 3.11 and 3.12 show the wake patterns generated behind twin rotating cylinders in side-by-side and tandem arrangements with large vortices convecting downstream.

The study of rotating twin cylinders at g^* =1.0 and angular rotation γ =1.0 has reported interesting results. Further parametric studies need to be conducted to evaluate and validate the model further, so as to apply for multi-body configuration of cylinders and to detail the flow characteristics.

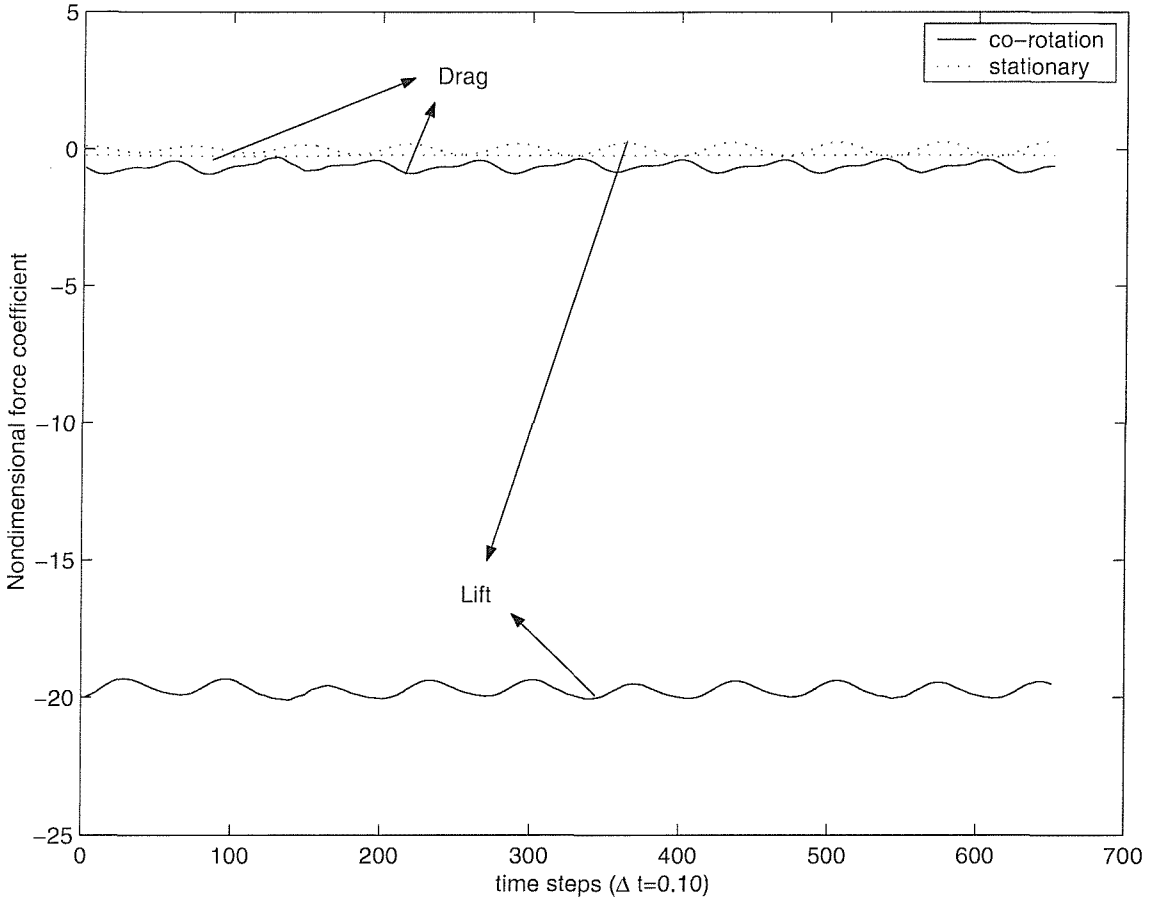

Figure 3.24: Lift C_l and drag C_d records with time illustrating the different characteristics experienced by the downstream twin tandem cylinder in co-rotation, g^* =1.0, R_e = 200 and angular rotation γ =1.0 in comparison to corresponding twin stationary cylinders

3.7 Conclusions

The Viscous Cell Boundary Element Method (VCBEM) is validated for the case of a single cylinder in rotation. The critical aspects of stagnation point and the alleyway formation around the primary vortex are shown to have similarities with other numerical predictions and experimental studies.

The method is then extended to the study of twin cylinders in various arrangements such as side-by-side and tandem. The magnitudes of mean drag (C_{dmean}) and mean lift (C_{lmean}) forces predicted in both arrangements are tabulated in Tables 3.11 and 3.12 for R_e=100 and angular velocity of rotation γ=1.0. In the case of the side-by-side arrangement we see a thorough mixing of vortices and high frequency forces in counter rotation as compared to a closed knitted wake and low frequency forces generated in the co-rotation case. In the case of a tandem arrangement thorough mixing of vortices

occurs downstream exhibiting a diffused wake. The cylinders are attracted to each other due to the interactive suction force and a high velocity of flow exists between the cylinders. The influence of the cylinders in counter rotation is seen in the downstream vortex shedding patterns, with a shift in the axis of shedding. The magnitude of forces are reduced compared to that of co-rotation case because of the counter effect of forces between the cylinders. These follow similar patterns of variation when compared to the co-rotation case, for cylinders positioned along the same axis to the flow.

The next chapter presents reduced-order modelling techniques which can be applied to construct low-order models to the Navier-Stokes equation. The key objective is to develop computationally inexpensive surrogate models which can be employed to design controllers to achieve vortex suppression.

Chapter 4

Reduced Order Modelling

4.1 Introduction

The advent of increasingly high performance computers has enhanced our ability to solve problems of high complexity and now one can construct, solve and predict the time histories and frequency domain responses of extremely large dynamic systems. One of the governing factors in dealing with such issues is the computational cost and time. Hence, precise models are prohibitive when parametric studies and analysis are required. The applicability of these models is significantly reduced when dealing with control problems since most control schemes can only be efficiently implemented for relatively small systems with 1-100 degrees of freedom (Deane et al., 1991, Berkooz et al., 1993, Ravindran & Ito, 1998, Epureanu et al., 2001).

The development of efficient numerical schemes for optimal flow control is a topic that has attracted much attention in recent years. One major challenge in this area arises from the fact that, in practice, computationally expensive high fidelity models are required to analyze the behaviour of controlled flows (Homescu et al., 2002). To overcome the computational obstacles to flow control, the idea of constructing computationally lower cost reduced order models has been pursued in many recent studies, see for example Deane et al. (1991), Ravindran & Ito (1998), Tan et al. (2000), Homescu et al. (2002). This lower cost of computation makes the Reduced Order Models (ROM), with their smaller degrees of freedom a possible way forward.

Reduced order models, in general, possess much smaller degrees of freedom as compared to the original model. The method attempts to capture the essential dynamics of the original model with acceptable accuracy. The tradeoff between complexity and accuracy is problem specific and application orientated. Many of the proposed control strategies have relatively large robustness to account for model uncertainties and hence

the ones designed and tested on reduced order models have proved successful on the full order systems (Deane et al., 1991, Berkooz et al., 1993, Epureanu et al., 2001). A uncertainity set is said to be strongly robust if the set contains the true system to be controlled and any model selected from this uncertainity set stabilizes the true system. In particular, a controller is said to be robust if it remains stable in the presence of neglected dynamics of the full order system.

The control systems can be of linear, nonlinear or adaptive type. In linear control systems the dynamic relationship between input and output will be as a first, second or higher order differential equations and the principle of superposition is valid in this case. The stability of nonlinear control systems described by state space notation and with continuous nonlinear characteristic is investigated by Liapunov methods (Joseph, 1998). Adaptive control system changes according to the environment and plant, which is usually evaluated by some performance index. The controller must adapt as rapidly as possible in comparison with the parameter changes of the environment or plant so that it is always at, or nearly at, its most suitable performance. As the adaptive controller requires a performance index, it is important that the chosen cost function should reflect the effect of system parameters which are likely to vary, so that adaptive nature can be realized to the full (Richards, 1979).

Previous work on reduced order models for fluid dynamic analysis used physical insights (Greitzer, 1976, Whitehead, 1959). Recently, systematic studies in developing reduced order model techniques have been undertaken, involving Pade' approximations to the unsteady aerodynamic transfer function (Udea & Dowell, 1984, Peterson & Crawley, 1988, Dowell, 1980), eigen mode summation either in the time or frequency domain (Dowell, 1995, Hall, 1994) and Proper Orthogonal Decomposition (Romanowski, 1996). Most techniques are primarily concerned with the linearized system, but techniques such as proper orthogonal decomposition have been applied to model both linear and non-linear phenomenon (Kirby & Sirovich, 1990, Noor, 1994, Stone & Cutler, 1996). Shaw & Pierre (1993, 1994) have investigated fully non-linear normal modes and reduced order models.

Reduced order model techniques have been applied to a wide range of systems such as the Burger models of turbulence (Canuto et al., 1988, Chambers et al., 1988), Euler equations, Navier-Stokes equations (Deane et al., 1991), turbulence & boundary layer models (Liu et al., 1994, Sirovich, 1987). The eigen modes for Navier-Stokes flow in the time domain was obtained by Mahajan et al. (1991).

4.2 Overview of Reduced Order Model Development

The various steps involved in the reduced order model development are briefly summarised to give an overview of the process of model reduction. The sequence of operations involved in the development of reduced order models is as follows:

- Aspects of model reduction: This section discusses the criteria to produce the ensemble data required for the model reduction process. The ensemble data can be generated either by physical or numerical experiments. In the case of numerical experiments, the full order Navier-Stokes equations are simulated to generate the necessary database for model reduction. In the current research, modified VCBEM is used to solve the full order Navier-Stokes equations to generate the ensemble data for the development of the reduced order model.

- Reduced Order Models for the rotating cylinder: Details of the methods involved in the development of reduced order models for the case of a rotating cylinder is explained in this section. There are two methods of model development

  I. Penalty function. The details of this model reduction technique are discussed in section 4.4.1

  II. Control function method.

  In the current investigation, the control function method is adopted to develop the reduced order model.

- Control function method: This section describes the model reduction process within the control function method. The control function method adopted in the current research involves

  I. The generation of an ensemble database of snapshots from the numerical simulation of the full order Navier-Stokes equations using modified VCBEM.

  II. Generation of control function snapshots from the full order Navier-Stokes equations to produce divergent free basis functions ϕ for the reduced order model.

  III. Generation of modified ensemble database for use in the proper orthogonal decomposition method to produce divergence free basis functions ϕ for the reduced order model.

IV. Application of the proper orthogonal decomposition method to modified ensemble database to generate the divergence free basis function ϕ in the proper orthogonal decomposition space.

V. Development of reduced order models using the divergence free basis function ϕ, derived by the application of proper orthogonal decomposition method on the modified ensemble database.

VI. Time marching of the reduced order model developed by the control function approach to produce predictions of time dependent modal amplitudes.

- Proper Orthogonal Decomposition: This section discusses the method of proper orthogonal decomposition in detail, which is used in the development of reduced order model. This method is applied to the modified ensemble database of snapshots to generate the divergence free basis functions ϕ for the control function reduced order model.

- Validation of Reduced Order Model for rotating cylinder: This section describes the validation of the generated control function used in the reduced order model by the comparison of projections determined from the full order modified VCBEM model and predictions derived from time marching of the reduced order model developed by control function approach.

In the current research, the control function method mathematical formulation of Graham et al. (1999) is used. A proper orthogonal decomposition method is adopted to derive the basis functions ϕ in the mathematical formulation and the modelling is developed based on the results derived using the modified VCBEM unstructured mesh approach. On generating the proper orthogonal decomposition basis functions ϕ, various coefficients of the control function method reduced order model are evaluated and used to produce predictions of time dependent modal amplitudes by using a time marching scheme.

4.3 Aspects of Model Reduction

Let us consider a superspace high fidelity model with N basis elements and a subspace for the reduced order model with M basis elements. The superspace dynamics are represented by snapshots collected at discrete time intervals, hence a sufficient number of snapshots should be selected to represent adequately the physical process and this forms the data base from which the reduced order model is extracted. Hence, sampling

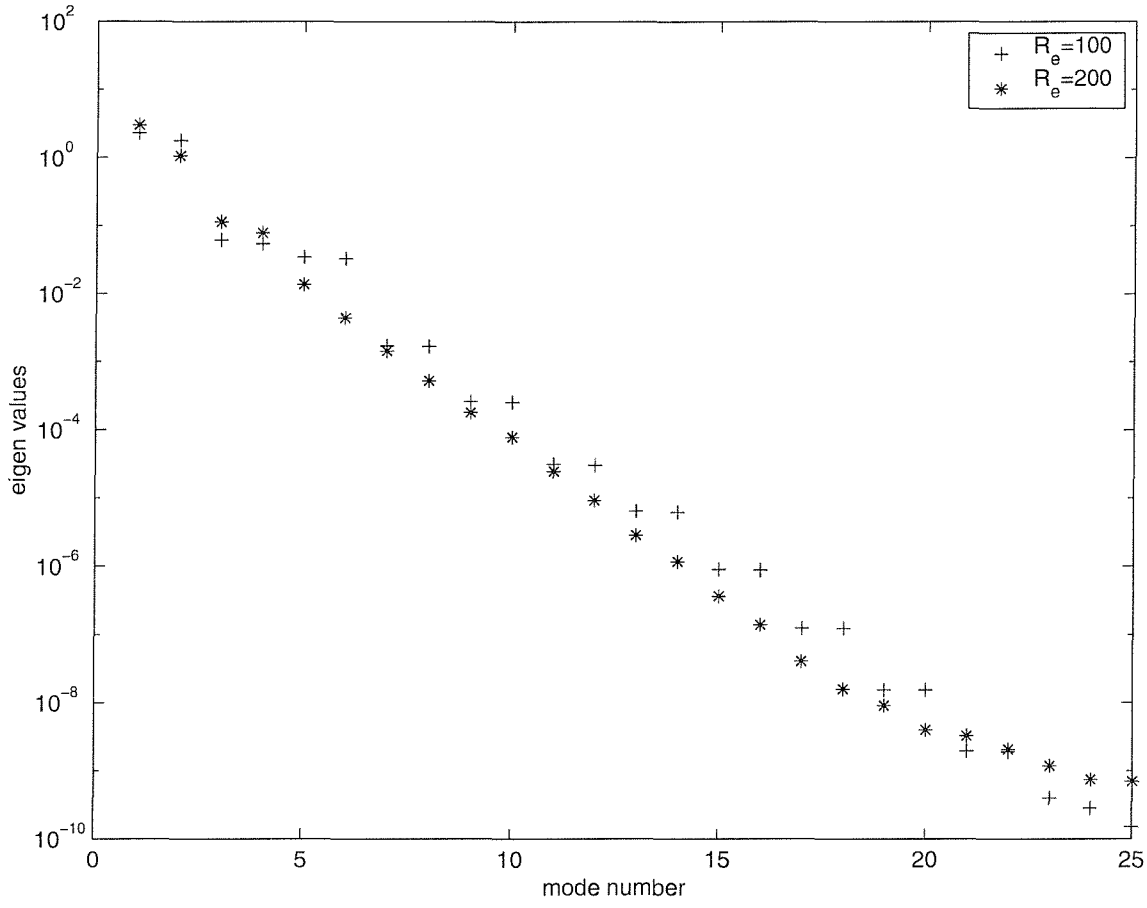

Figure 4.1: Typical semilog plot of eigenvalues of the correlation matrix for datasets generated for flows of $R_e = 100$ and $R_e = 200$ at the start of flow.

and selection of snapshots of the full order model plays a vital role in the generation of the reduced order model to represent the physical process.

The sampling of snapshots can be chosen as a function of the signal which represents the system. As an example, let us consider the vortex shedding problem with the lift coefficient selected as signal. The signal must be band limited containing frequencies up to some maximum frequency in the frequency spectrum. The research work of Joseph (1998) on optimal control of unsteady flow around the cylinder showed that when Nyquist criterion is violated the numerical eigen values exhibit a nonphysical behaviour and hence care must be taken to construct discretizations to avoid numerical artifacts. The detailed mathematical analysis of Nyquist criterion for vortex shedding problem is presented in the work of Joseph (1998). The sampling rate allowed is the Nyquist rate which is the maximum frequency and at least twice the maximum frequency should be selected as the upper limit of the frequency spectrum (Graham et al., 1999, Gillies, 1998, Ravindran, 1999, Homescu et al., 2002). Consider the vortex

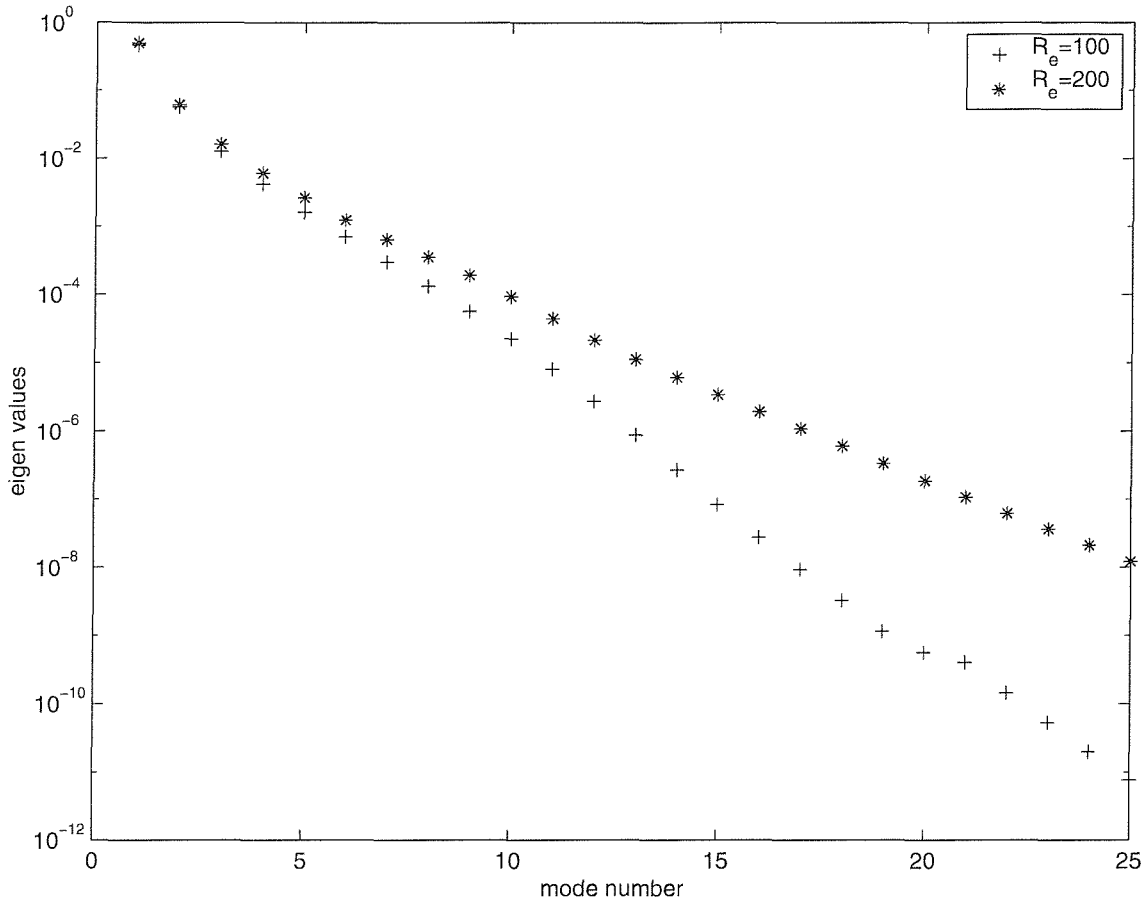

Figure 4.2: Typical semilog plot of eigenvalues of the correlation matrix for datasets generated for flows of $R_e = 100$ and $R_e = 200$ at steady state of vortex shedding.

shedding problem which is periodic in nature and governed by predominant modes. Twice the vortex shedding period captures the significant physical phenomenon to be described. The efficiency of the reduced order model is based on the degree of capture of the underlying dynamics of the system. In order to capture the essential dynamics it is expedient to keep N as large as needed.

Let us consider the characteristic behaviour of energy spectrum of covariance matrix in correspondence to physical process under consideration. If the energy spectrum of physical process is uniform, the process is controlled by many modes and all the eigen modes have significant influence on the process on the contrary to a decaying energy spectrum with principal eigen modes controlling the physical process. Vortex shedding problem exhibits a decaying spectrum as shown in Figures 4.1 and 4.2 indicating the physical process is controlled by principal eigen modes.

The characteristic of the eigenvalues of the covariance matrix $\mathbf{A}$(as in equation 4.27) is used to determine the maximum number of the reduced set of basis elements M and

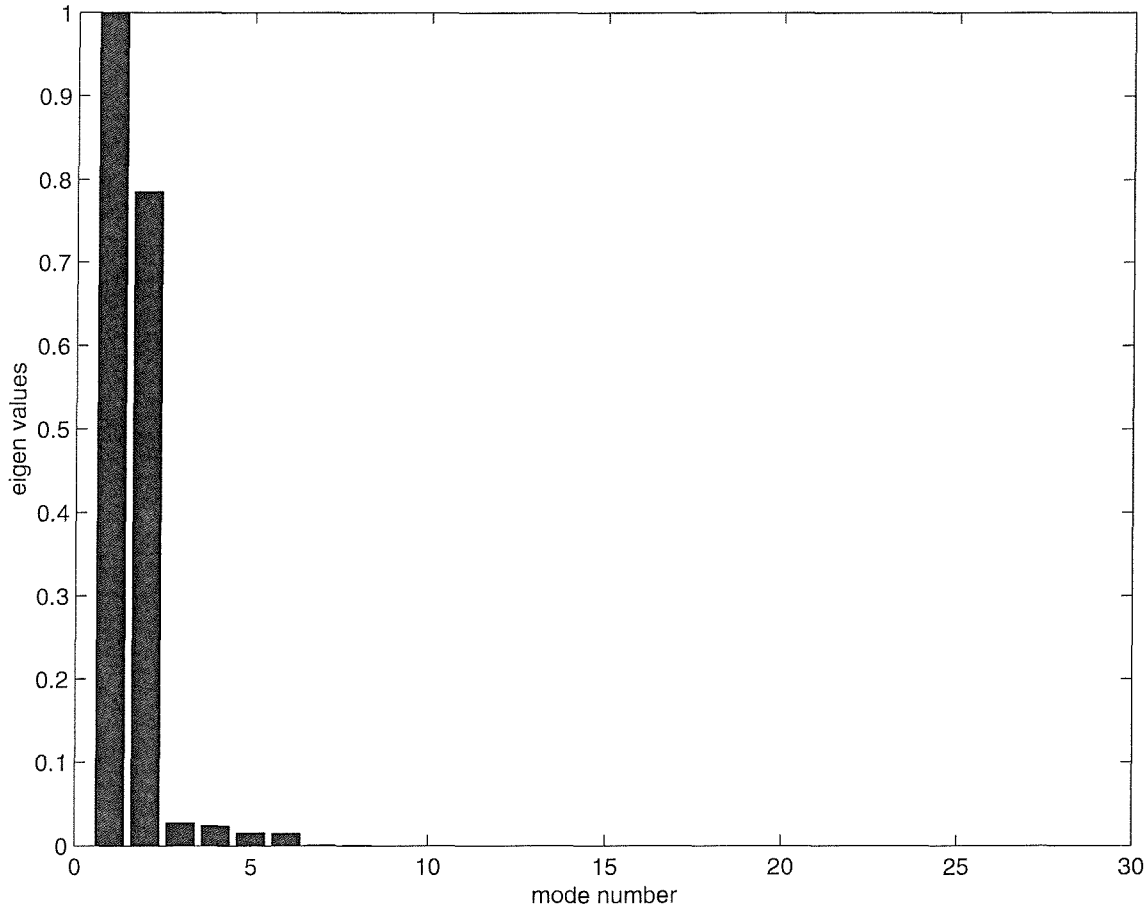

Figure 4.3: Typical representation of normalized eigenvalues of the correlation matrix for the datasets used.

this will be a large number if the rate of decay of eigenvalues in the covariance matrix is low. If the eigenvalues of the covariance matrix decay at a faster rate, we can select M $\ll$ N, and carry out Galerkin procedures on the reduced basis set $[\phi_1, \ldots \phi_m]$ so that $\sum_{i=1}^{M} \lambda_i \approx \sum_{i=1}^{N} \lambda_i$, where λ_i denotes the ith eigenvalue. As the number of modes incorporated in the reduced order model increases the design of control becomes complicated and hence an optimum number of modes should be selected, which is based on energy criteria for the vortex shedding problem. It is shown in Graham et al. (1999), Ravindran (1999) that the sum of all the eigen values represent the average unsteady energy in the data set considered. If the eigen values are ordered ($\lambda_i > \lambda_{i+1}$), then the ratio $\frac{\sum_{i=1}^{M} \lambda_i}{\sum_{i=1}^{N} \lambda_i}$ determines the percentage of total kinetic energy contained in the first M proper orthogonal decomposition elements.

The numerical data describing the wake are generated by the modified viscous cell boundary element method and typically sixty snap shots per cycle are collected. Figures 4.1 and 4.2 represent the typical semilog plot of eigen values of the correlation

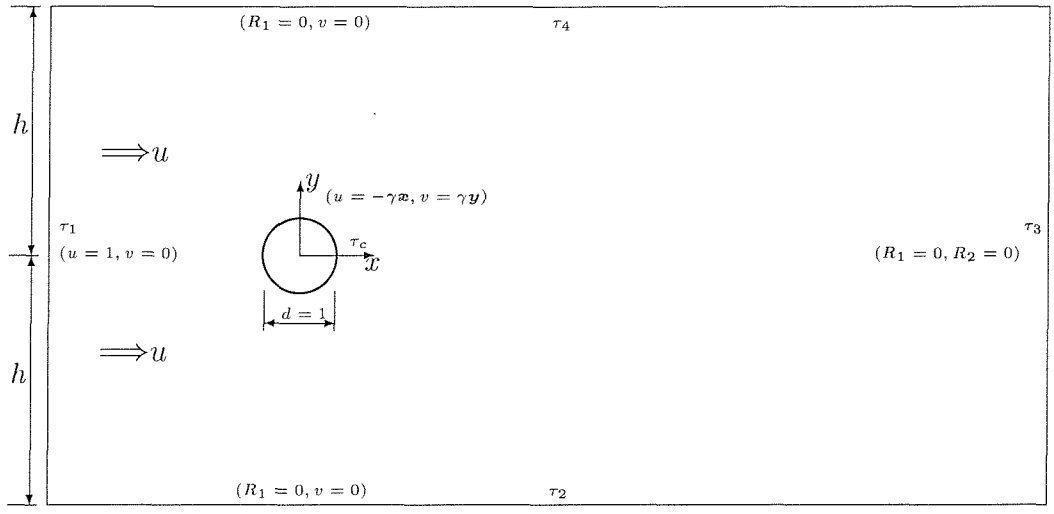

Figure 4.4: Computational domain definition and boundary conditions for rotating cylinder in a uniform flow. All the variables and quantities are nondimensional

matrix for flows of $R_e = 100$ and $R_e = 200$ at the start of flow and when the flow reaches a steady state of vortex shedding. Figure 4.3 shows a typical plot of the magnitude of the evaluated eigenvalues produced for the data sets generated. This confirms the rapid rate of decay of the eigenvalues of the covariance matrix and also the eigenvalues indicate the energy level in each mode. From this picture, it is evident that only the first few modes contain most of the energy associated with vortex shedding and hence M $\ll$ N can be adopted. In the analysis $M = 6$ is used, i.e the first six modes, which capture 99.84 % of the flow energy.

4.4 Reduced Order Models for Rotating Cylinder

Let us now consider the case of a rotating cylinder as discussed in Chapter 3 and apply the proper orthogonal decomposition approach to the *lock on* flow. That is, when the natural frequency of vortex shedding synchronizes with the frequency of cylinder rotation producing a strong vortex shedding. The eigen spectrum is concentrated on the first few modes and the modal structure is similar to a stationary cylinder as reported by Graham et al. (1999). Since the cylinder rotates, the velocity formulation required for the Galerkin projection changes (Graham et al., 1999). Graham et al. (1999) proposed the following two methods to solve the problem of rotating cylinders:

I. Penalty function method.

II. Control function method.

To the best of authors knowledge, these are the only two methods available in current literature for rotating cylinder case. In the penalty function, the inhomogeneous boundary conditions are incorporated in a weak form in the Galerkin projection and the basis functions retain their original form. The control function method involves the removal of inhomogeneous boundary conditions by a suitably chosen function e.g. the control function in the velocity field expansion producing the homogeneous boundary conditions on the basis functions used in Galerkin projections (Graham et al., 1999). In current research control function method is adopted since it can be readily extended to construct reduced order models for flow around multiple array of cylinders. The mathematical details of the method can be found in Graham et al. (1999). For the completeness of formulation a summary of the methods propose by Graham et al. (1999) is given in section 4.4.1 and 4.5 to follow.

4.4.1 The penalty function method

In this method the velocity v is determined or measured at a distance ϵ from the cylinder's boundary in the fluid and this distance is reduced until satisfactory solutions are obtained. The velocity on the cylinder is expressed by (Graham et al., 1999)

$$v = \gamma Re_\theta - \epsilon \frac{\partial v}{\partial n} \tag{4.1}$$

where R(=1/2) is the cylinder's (nondimensional) radius, e_θ is the unit tangent vector and γ denotes the angular rotation of the cylinder. From equation 4.1,

$$\frac{\partial v}{\partial n} = -\frac{v - \gamma Re_\theta}{\epsilon} \tag{4.2}$$

This can be incorporated in a Galerkin projection via surface integral terms (Zienkiewicz & Morgan, 1982). The velocity field expansion can be written as

$$\tilde{\boldsymbol{v}}(\boldsymbol{x}, t) = \bar{\boldsymbol{v}}(\boldsymbol{x}) + \sum_{k=1}^{n} y_k(t) \boldsymbol{\phi}_k(\boldsymbol{x}) \tag{4.3}$$

where $y_k(t), k = 1, 2, \ldots, n$ are the undetermined time-dependent amplitudes of the proper orthogonal decomposition modes.

On substituting equation 4.3 into equation 4.4, which is described in section 4.6.1,

$$(\boldsymbol{\phi}_i, \frac{\partial v}{\partial t} + (v.\nabla)v) + (\boldsymbol{\phi}_i, \nabla p) = \frac{1}{R_e}(\nabla \boldsymbol{\phi}_i, \nabla v) + \frac{1}{R_e}[\boldsymbol{\phi}_i \nabla v]. \tag{4.4}$$

we arrive at the following reduced order system of n ordinary differential equations

$$\frac{dy_i}{dt} = a_i + \sum_{j=1}^{N} b_{ij}\ y_j + \sum_{j=1}^{N}\sum_{k=1}^{N} c_{ijk}\ y_j\ y_k + d_i\gamma \tag{4.5}$$

The coefficients of the differential equation are given by

$$a_i = -(\phi_i, (\bar{\boldsymbol{v}}.\nabla)\bar{\boldsymbol{v}}) - \frac{1}{R_e}(\nabla\phi_i, \nabla\bar{\boldsymbol{v}}) + \frac{1}{R_e}[\phi_i \nabla\bar{\boldsymbol{v}}] - \frac{1}{R_e}\int_{\tau_c} \phi_i(\frac{\bar{\boldsymbol{v}}}{\epsilon} + \frac{\partial\bar{\boldsymbol{v}}}{\partial n})d\tau \tag{4.6}$$

$$b_{ij} = -(\phi_i, (\phi_j.\nabla)\bar{\boldsymbol{v}}) - (\phi_i, (\bar{\boldsymbol{v}}.\nabla)\phi_j)$$

$$-\frac{1}{R_e}(\nabla\phi_i, \nabla\phi_j) + \frac{1}{R_e}[\phi_i\nabla\phi_j] - \frac{1}{R_e}\int_{\tau_c} \phi_i(\frac{\phi_j}{\epsilon} + \frac{\partial\phi_j}{\partial n})d\tau \tag{4.7}$$

$$c_{ijk} = -(\phi_i, (\phi_j.\nabla)\phi_k) \tag{4.8}$$

$$d_i = \frac{1}{\epsilon R_e}\int_{\tau_c} \phi_i.(Re_\theta)d\tau \tag{4.9}$$

where $(a,b) = \int_\Omega a.b\ d\Omega$; $(\alpha, a) = \int_\Omega \alpha a\ d\Omega$; $[a] = \int_{\tau_{1,2,3,4,c}} a.n\ d\tau$

Once the coefficients are evaluated and suitable initial conditions prescribed for y_i, and the time history of the control input γ known, a time marching scheme applied to equation 4.5 produces the predictions of the modal amplitudes for the reduced order model.

4.5 Control Function Method

In this method, the inhomogeneous boundary conditions describing rotation on the cylinder τ_c are removed from each snapshot by subtracting a suitable *control function* before generating proper orthogonal decomposition basis functions. The control function to be selected is arbitrary but has to be divergent free in order to retain divergence free properties of the basis functions (Graham et al., 1999). It should also satisfy the

homogeneous boundary conditions on τ_1, τ_2 and τ_4. Hence, the control function can be conveniently generated by a flow simulation of the desired motion of the boundary. In this study the control function $v_c(x)$ is generated by a steady cylinder rotation with angular velocity $\gamma = 1.0$. The modified snapshot dataset is then given by

$$v(x, t^k) - \gamma(t^k) v_c(x) \tag{4.10}$$

which produces a snapshot data set which gives divergent free basis functions. The reduced basis function and the mean flows are generated from this modified snapshot set. The reduced basis function ϕ thus generated has zero velocity on the cylinder surface and the velocity field expansion equation 4.11 automatically satisfies the boundary conditions. This can be written as

$$\tilde{\boldsymbol{v}}(\boldsymbol{x}, t) = \bar{\boldsymbol{v}}(\boldsymbol{x}) + \gamma(t)\boldsymbol{v_c}(\boldsymbol{x}) + \sum_{k=1}^{n} y_k(t)\boldsymbol{\phi}_k(\boldsymbol{x}) \tag{4.11}$$

where $y_k(t), k = 1, 2, \ldots, n$ are the undetermined time-dependent amplitudes of the proper orthogonal decomposition modes.

On substituting equation 4.11 into equation 4.4, which is described in section 4.6.1, we arrive at the following reduced-order system of n ordinary differential equations

$$\frac{dy_i}{dt} = a_i + \sum_{j=1}^{n} b_{ij}\ y_j + \sum_{j=1}^{n}\sum_{k=1}^{n} c_{ijk}\ y_j\ y_k +$$

$$d_i \frac{d\gamma}{dt} + (e_i + \sum_{j=1}^{n} f_{ij}\ y_j)\gamma + g_i\gamma^2. \tag{4.12}$$

The coefficients of the differential equation are given by

$$a_i = -(\phi_i, (\bar{\boldsymbol{v}}.\nabla)\bar{\boldsymbol{v}}) - \frac{1}{R_e}(\nabla\phi_i, \nabla\bar{\boldsymbol{v}}) + \frac{1}{R_e}[\phi_i \nabla\bar{\boldsymbol{v}}], \tag{4.13}$$

$$b_{ij} = -(\phi_i, (\phi_j.\nabla)\bar{\boldsymbol{v}}) - (\phi_i, (\bar{\boldsymbol{v}}.\nabla)\phi_j)$$

$$+\frac{1}{R_e}(\nabla\phi_i, \nabla\phi_j) + \frac{1}{R_e}[\phi_i \nabla\phi_j], \tag{4.14}$$

$$c_{ijk} = -(\phi_i, (\phi_j.\nabla)\phi_k), \tag{4.15}$$

$$d_i = -(\phi_i, v_c), \tag{4.16}$$

$$e_i = -(\phi_i, (\bar{\boldsymbol{v}}.\nabla)v_c) - (\phi_i, (v_c.\nabla)\bar{\boldsymbol{v}})$$

$$-\frac{1}{R_e}(\nabla\phi_i, v_c) + \frac{1}{R_e}[\phi_i \nabla v_c], \tag{4.17}$$

$$f_{ij} = -(\phi_i, (\phi_j.\nabla)v_c) - (\phi_i, (v_c.\nabla)\phi_j), \tag{4.18}$$

$$g_i = -(\phi_i, (v_c.\nabla)v_c). \tag{4.19}$$

Once suitable initial conditions are prescribed for y_i and the time history of the control input γ known, a time marching scheme can be used for equation 4.12 to compute the evolution of modal amplitudes y_i. The mathematical details of the method can be found in Graham et al. (1999).

It is beneficial to retain divergence free condition on the basis functions used in Galerkin projection since the model is suitable for further extension to multi body configuration of cylinders and for this reason a control function method is adopted in the analysis.

4.6 Proper Orthogonal Decomposition

In this study reduced order models for active control are constructed using proper orthogonal decomposition. In other words, proper orthogonal decomposition is used to design reduced order models which capture the essential dynamics of the flow field predicted using the computationally expensive Navier-Stokes equations. The motivation for this arises from the fact that the solution of complex fluid dynamic problems using techniques such as finite element, finite volume, finite difference or spectral method are not feasible generally for real time control (Ravindran, 1999, Ravindran & Ito, 1998).

Proper orthogonal decomposition is a model reduction technique for complex nonlinear systems and was originally proposed by Lumley (1967). The mathematical foundations of this technique are based on the seminal works of Loeve (1945) and Karhunen (1946).

Basis functions are used for spatial discretization in a proper orthogonal decomposition method. However, these basis functions are extracted from numerical simulations using a high fidelity model or experimental results.

For any given ensemble of data, through application of proper orthogonal decomposition an orthonormal co-ordinate system is generated. This is optimal in the sense that approximate representation of 'snapshots' using the basis functions ϕ derived by proper orthogonal decomposition maximizes the captured energy. This is the basis for the generation of optimal basis functions for Galerkin representation (Ravindran, 1999, Graham et al., 1999, Hirsch, 1988, Van de Vosse et al., 1986, Li et al., 1991).

4.6.1 Proper orthogonal decomposition illustration

To illustrate a proper orthogonal decomposition application and the development of a proper orthogonal decomposition subspace to a specific problem, let us examine the two dimensional, incompressible flow of a fluid past a circular cylinder of diameter d. The computational domain and boundary conditions are shown in Figure 4.4. Given an ensemble of flow field snapshots predicted by the Navier-Stokes equation, the reduced-order modelling problem reduces to:

(1) extracting coherent structures from the snapshots of the flow field and

(2) employing the computed structures to construct a low-order mathematical model.

Methodology

Given an ensemble of the vector field v, it is necessary to elicit a function ϕ which typifies members of the ensemble. The function $\boldsymbol{\phi}_k(\boldsymbol{x})$ is chosen such that the projection of the ensemble onto the subspace of the function ϕ for which the inner-product (ϕ, ϕ) exists, is maximal with respect to the function $\boldsymbol{\phi}_k(\boldsymbol{x})$ (*i.e.* $(\boldsymbol{\phi}_k, \boldsymbol{\phi}_k) \equiv \int \boldsymbol{\phi}_k(\boldsymbol{x}) \cdot \boldsymbol{\phi}_k(\boldsymbol{x}) \mathrm{d}\boldsymbol{x} = 1$). Once this function is found, the ensemble can be projected onto the subspace spanned by ϕ. As shown by Ravindran (1999), ϕ can be computed by maximizing the expression

$$\sum_{i=1}^{m} \frac{|(\boldsymbol{v}(\boldsymbol{x}, t_i), \boldsymbol{\phi})|^2}{(\boldsymbol{\phi}, \boldsymbol{\phi})^{1/2}}, \tag{4.20}$$

which incorporates the flow field statistics of the problem under consideration and m stands for the number of solutions at different time steps.

Let us consider a spatio-temporal ensemble of velocity field $\tilde{\boldsymbol{v}}(\boldsymbol{x}, t)$ defined over the spatial domain Ω in the interval of $0 \leq t \leq T$. Let us assume that the velocity field $\tilde{\boldsymbol{v}}(\boldsymbol{x}, t)$ can be written as

$$\tilde{\boldsymbol{v}}(\boldsymbol{x}, t) = \bar{\boldsymbol{v}}(\boldsymbol{x}) + \boldsymbol{v}(\boldsymbol{x}, t), \tag{4.21}$$

where $\bar{\boldsymbol{v}}(\boldsymbol{x})$ is the temporal mean of the velocity field and $\tilde{\boldsymbol{v}}(\boldsymbol{x}, t_i)_{i=1}^{i=m}$ obtained at the m snapshots or discrete time intervals t_i along fixed points in the spatial domain.

The temporal mean, when reduced from the velocity field given by equation 4.21 provides insight into the structural fluctuations. If we denote the temporal mean of $\boldsymbol{v}(\boldsymbol{x}, t)$ by $\langle \boldsymbol{v}(\boldsymbol{x}, t) \rangle$, it will be zero in equation 4.21.

The derived functions $\boldsymbol{\phi}_k(\boldsymbol{x})$, are the eigenfunctions of a Fredholm integral equation of the second kind, i.e.

$$\int_{\Omega} \boldsymbol{K}(\boldsymbol{x}, \boldsymbol{x}') \cdot \boldsymbol{\phi}(\boldsymbol{x}') \, \mathrm{d}\boldsymbol{x}' \; = \; \lambda \boldsymbol{\phi}(\boldsymbol{x}) \tag{4.22}$$

where the kernel $\boldsymbol{K}(\boldsymbol{x}, \boldsymbol{x}')$ is the time averaged correlation function

$$\boldsymbol{K}(\boldsymbol{x}, \boldsymbol{x}') \; = \; \langle \boldsymbol{v}(\boldsymbol{x}, t) \, \boldsymbol{v}(\boldsymbol{x}', t) \rangle. \tag{4.23}$$

where $\langle . \rangle$ denotes the time average operator. These functions $(\boldsymbol{\phi}_k(\boldsymbol{x}), \; k = 1, \cdots)$ are called the *empirical eigenfunctions* or the *coherent structures*.

It is seen from the works of Sirovich (1987) that any projection of the data on to

a finite set of $\boldsymbol{\phi}_k(\boldsymbol{x})$ is given by

$$\boldsymbol{v}_n(\boldsymbol{x},t) = \sum_{k=1}^{n} y_k(t)\boldsymbol{\phi}_k(\boldsymbol{x}). \tag{4.24}$$

The sample vectors are reconstructed using

$$\tilde{\boldsymbol{v}}(\boldsymbol{x},t) = \bar{\boldsymbol{v}}(\boldsymbol{x}) + \sum_{k=1}^{n} y_k(t)\boldsymbol{\phi}_k(\boldsymbol{x}). \tag{4.25}$$

The coefficients $y_k(t)$ are determined from the reduced dynamical equations and the parametric value of n depends upon the maximum number of coherent structures required to capture the essential dynamics of the system (Ravindran, 1999, Tan et al., 2000).

Since low dimensional attractors are derived from the complex spatio-temporal data, which are the representations of the system under consideration, high spatial resolution is a necessity to ensure the fidelity of the model. In such cases, the size of spatial data set ϱ is bulky and the calculation of a $\varrho \times \varrho$ correlation matrix to evaluate the correlation function is impractical and so a dual approach applied to the m snapshots is inevitable as discussed by Sirovich (1987). This method is also known as *sample space setting* (Preisendorfer, 1988), where the snapshot vectors $\boldsymbol{v}(\boldsymbol{x},t_i)$, $i = 1,\ldots,m$ are considered and they determine the empirical eigenfunctions $\boldsymbol{\phi}_k(\boldsymbol{x})$ as a linear combination of the snapshots given by,

$$\boldsymbol{\phi}_k(\boldsymbol{x}) = \sum_{i=1}^{m} \alpha_i^{(k)} \boldsymbol{v}(\boldsymbol{x},t_i) \tag{4.26}$$

such that equation 4.22 is satisfied. The corresponding eigenvalue problem requires determination of the eigenvalues and eigenfunctions of a symmetric matrix $m \times m$ such that,

$$\boldsymbol{A}\,\boldsymbol{\alpha}^{(k)} = \lambda_k \boldsymbol{\alpha}^{(k)} \tag{4.27}$$

where

$$A_{ij} = \frac{1}{m}\int_{\Omega} \boldsymbol{v}(\boldsymbol{x},t_i)\cdot\boldsymbol{v}(\boldsymbol{x},t_j)\,\mathrm{d}\boldsymbol{x} \tag{4.28}$$

and $\boldsymbol{\alpha}^{(k)}$ is a single column array with $\alpha_i^{(k)}$ introduced in equation 4.26 as elements.

The sum of all the eigenvalues of the correlation function represents the average

unsteady energy E of the dataset corresponding to the velocity because the trace of the matrix $\boldsymbol{A}$ represents the average energy retained in the snapshot. Hence

$$E = \sum_{i=1} \lambda_i \tag{4.29}$$

where the eigenvalues are arranged in descending order i.e ordering of the eigenfunctions from largest to least energy content.

The coefficients $y(t)$ at given discrete times t_i are computed from a projection of the sample vector onto an eigenfunction given by,

$$y_k(t_i) = \int_\Omega \boldsymbol{v}(\boldsymbol{x}, t_i) \cdot \boldsymbol{\phi}_k(\boldsymbol{x}) \, \mathrm{d}\boldsymbol{x} = m\lambda_k \alpha_i^{(k)}. \tag{4.30}$$

The expression given in equation 4.30 is used to evaluate the initial conditions and the necessary projection data for the time marching events of $y_k(t)$. The Galerkin projection scheme is then used to derive lower dimensional mathematical models. The objective of this approach is to replace the given dynamics by the dynamics of the subspace in the form

$$\dot{y}(t) = f(y(t)) \tag{4.31}$$

where $y(t)$ is the time-dependent amplitude of the basis functions as discussed by Tan et al. (2000).

For problems associated with non-stationary flows with forcing, the system under examination is formulated by Tan et al. (2000) as,

$$\dot{\boldsymbol{v}}(\boldsymbol{x}, t) = NS(\boldsymbol{v}(\boldsymbol{x}, t), c(\boldsymbol{x}, t)) \tag{4.32}$$

$$z(t) = h(\boldsymbol{v}(\boldsymbol{x}, t)) \tag{4.33}$$

where NS denotes Navier-Stokes solution for the control input, c denotes the control input and z represents an output signal.

Galerkin Procedure

For a fluid assumed incompressible, as discussed in Chapter 2, the Navier-Stokes equation of the flow in terms of a non-dimensional velocity field $v_k(t)$, relative velocity

between body $\tilde{v}_k(t)$ and fluid i.e $U_k = \tilde{v}_k(t) - v_k(t)$ and the pressure p is given by

$$\dot{v}_j + (v_j U_k)_{,k} + p_{,j} - [\nu_e(v_{j,k} + v_{k,j})]_{,k} = 0, \tag{4.34}$$

$$v_{j,j} = 0. \tag{4.35}$$

where $\nu_e(= 1/R_e)$ represents the inverse of the Reynolds number. The subscript index j=1, 2 or j=1, 2, 3 denotes two-dimensional and three-dimensional body-fluid interaction problems respectively.

If the operator $\int_\Omega \phi_{ji}\ ()\ d\Omega$ is applied to the Navier-Stokes equation, the following reduced model is obtained (Graham et al., 1999). That is,

$$\begin{aligned}(\boldsymbol{\phi}_i, \frac{\partial v}{\partial t} + (v.\nabla)v) + (\boldsymbol{\phi}_i, \nabla p) \\ = \frac{1}{R_e}(\nabla \boldsymbol{\phi}_i, \nabla v) + \frac{1}{R_e}[\boldsymbol{\phi}_i \nabla v].\end{aligned} \tag{4.36}$$

Equation 4.35 is satisfied automatically since the basis functions created by the proper orthogonal decomposition method are divergence free because of their definition as discussed by Sirovich (1987).

4.7 Development of Reduced Order Model for modified VCBEM.

The two methods of reduced order model development for rotating cylinders, Control function and penalty function methods were developed by Graham et al. (1999). The current research involves the implementation of the method developed by Graham et al. (1999) and proper orthogonal decomposition procedure proposed by Ravindran (1999) for developing the reduced order model for modified VCBEM. The reduced order model for modified VCBEM is developed using the Control function approach proposed by Graham et al. (1999). In the current research the boundary conditions on the surface of cylinders are incorporated in unstructured mesh generation programme and VCBEM solver is modified to account for time dependent boundary conditions in flow simulations. In the case of penalty function method, the velocity v is obtained by trial and error for each case as compared to control function method, which incorporates rotation of cylinder in the mathematical formulation. Control function method provides means for generating a modified dataset from which divergence free basis

functions ϕ are derived. This provides a generalized approach which can be extended for array of multiple cylinders and is hence developed for modified VCBEM in order to further extend the study to array of cylinders. A complete set of control function reduced order model numerical codes are developed for an unstructured mesh modified VCBEM solver in the current research, which can further be used for the analysis of multiple array of cylinders. The divergence free basis functions ϕ are derived for the control function approach from the modified snapshot database computed by modified VCBEM using the proper orthogonal decomposition procedure described by Ravindran (1999). A set of numerical codes was developed for deriving ϕ for the dataset generated by modified VCBEM.

4.8 Validation of Reduced Order Model

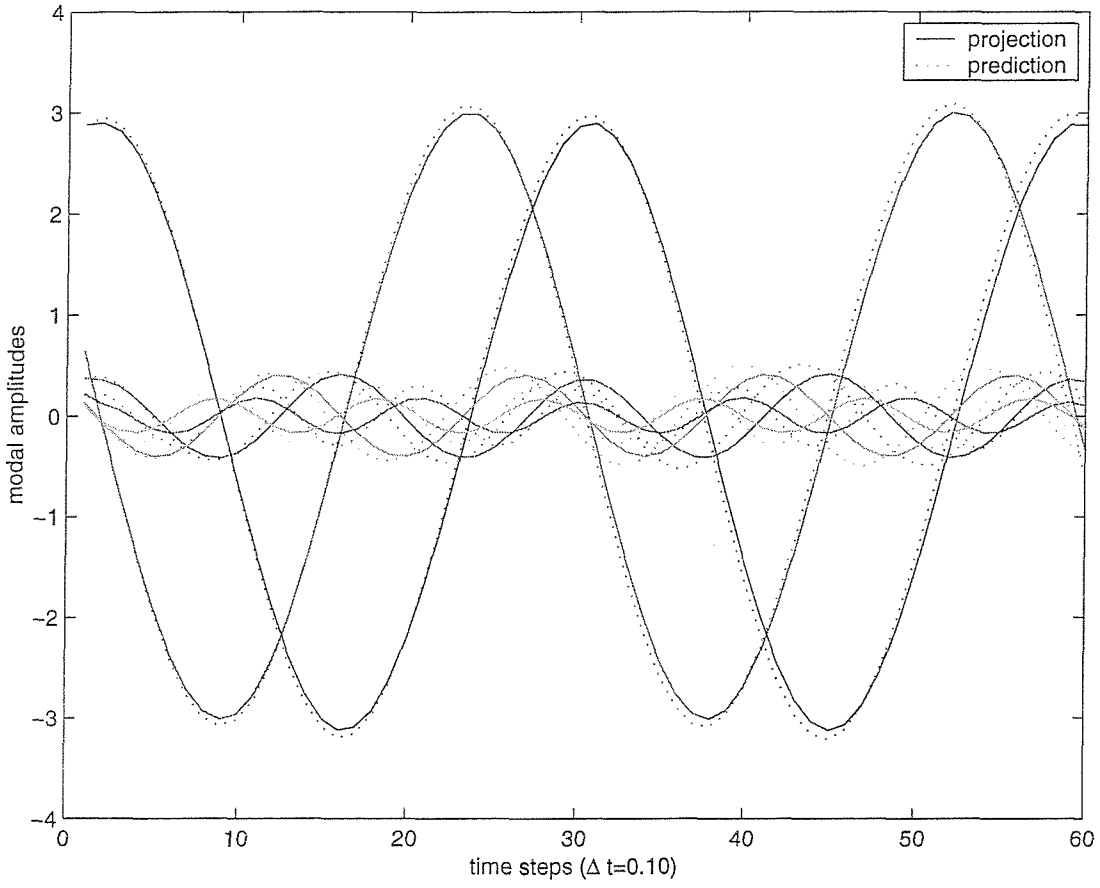

Figure 4.5: Comparison of predicted and projected modal amplitudes for Reynolds number $R_e = 100$ and angular rotation $\gamma = 2\sin(\pi t/3)$.

Time-dependent boundary conditions were incorporated into the VCBEM method and the validation of the code is discussed in Chapter 3. The computational domain and boundary conditions are shown in Figure 4.4. Here, τ_1, τ_2, τ_3 and τ_4 represent boundary conditions on the inlet, bottom, outlet and top respectively. The boundary τ_c, represents the no slip condition on the surface of the cylinder with horizontal and vertical velocity components $u = -\gamma y$, $v = \gamma x$ respectively. The top and bottom boundary conditions of the computational domain are assumed to maintain symmetry having mixed boundary conditions of zero horizontal traction force and zero vertical velocity. A zero traction force is imposed on the outlet force and a uniform horizontal flow velocity at the inlet.

Farrant (1998), Uzunoglu et al. (2001) showed that the influence of the boundary conditions on C_l and C_d is insignificant for sufficiently large semi-width (h) of the computational domain. Research works of Uzunoglu et al. (2001) showed that if, h is the semi-length and semi-width of a computational domain then, $h = 9d$ is sufficient for mixed boundary conditions of velocity and traction forces. Hence in this set of computations, an upstream domain and a semi-width computational domain of $h = 10d$ is adopted, whereas the downstream domain is $20d$.

The reduced order model developed was found to be consistent with predictions obtained from reduced order model matching reasonably well with projections from full order modified VCBEM. In order to validate the reduced order model developed a set of 60 snapshots at a time step interval of 0.20 were collected, corresponding to twice the lift Nyquist frequency, by executing the full-order VCBEM code for the case $\gamma(t) = 2\sin \pi t/3$. The eigenvalues of the correlation matrix computed using these snapshots are shown in Figure 4.3. The reduced order model was constructed with different modes and was found consistent with full order model. The computational time increased with the increase in the number of modes included in the reduced order model construction. The design of controller gets more complicated with more number of modes and hence an minimum number of modes are to be selected for the reduced order model construction which can represent the full order system with sufficient accuracy. As seen from the Figure 4.3, the first six modes were found sufficient to account for the energy of the system under consideration and was optimum from the computational time. In this case, the first 6 modes capture 99.84 % of the flow energy. The predicted and projected basis function amplitudes were found to be in agreement. It was observed that the reduced-order model agreed reasonably well with the full-order Navier-Stokes equations for this particular control input and this evidence is shown in Figure 4.5. In lieu with the physical flow phenonmenon of vortex shedding goverened by the predominant eigen modes flow, computational time considerations

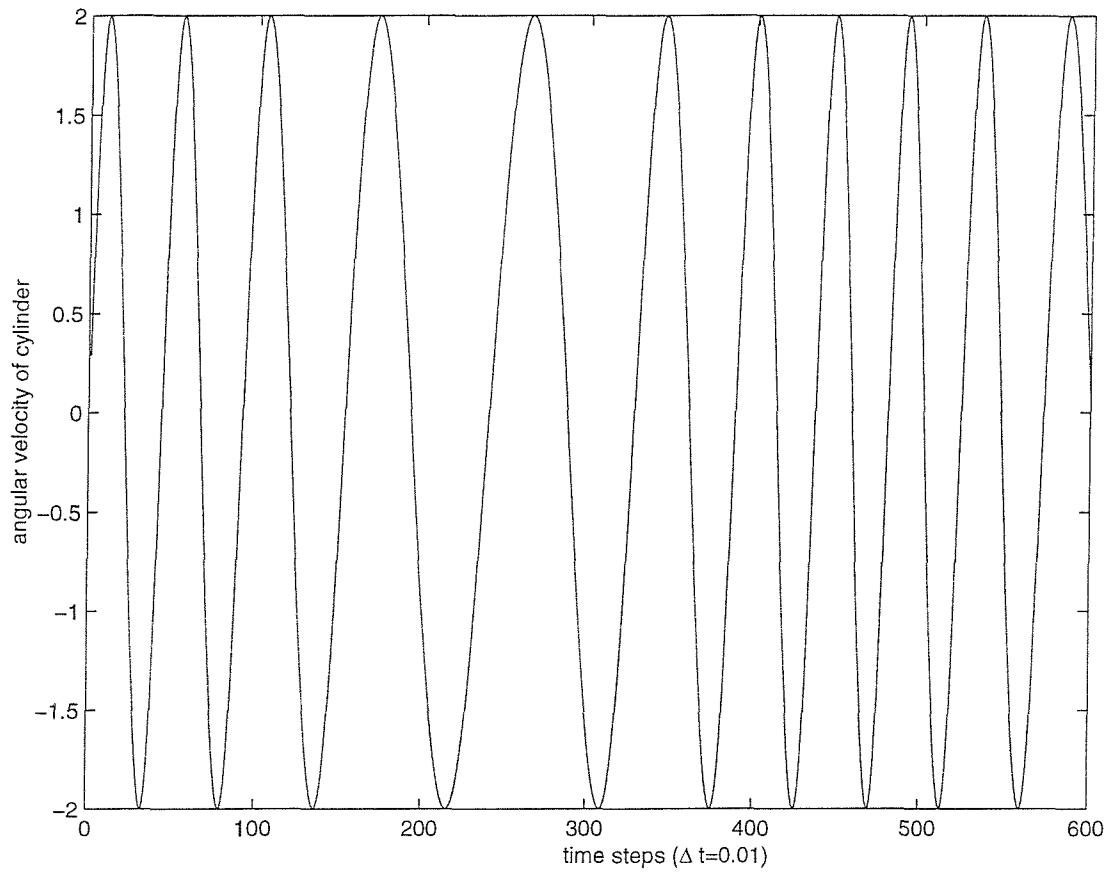

Figure 4.6: Time history of angular rotation $\gamma = \gamma_0 \sin[\frac{2\pi t}{T_1} + A\pi \sin(\frac{2\pi t}{T_2})]$ as chosen by Graham et al. (1999)

and design of controller, the first 6 modes are adopted in future studies.

The optimal control input can be either a regular or a irregular signal, hence for generality the reduced order model is tested for an irregular signal input. A parameterized time history of the time-dependent boundary conditions is used to study the behaviour of the reduced order model to an irregular signal. This also allows us to judge the efficacy of the reduced order model to capture the unsteady dynamics of the system. In order to carry out this system identification procedure the cylinder rotation γ is given by,

$$\gamma = \gamma_0 \sin[\frac{2\pi t}{T_1} + A\pi \sin(\frac{2\pi t}{T_2})] \tag{4.37}$$

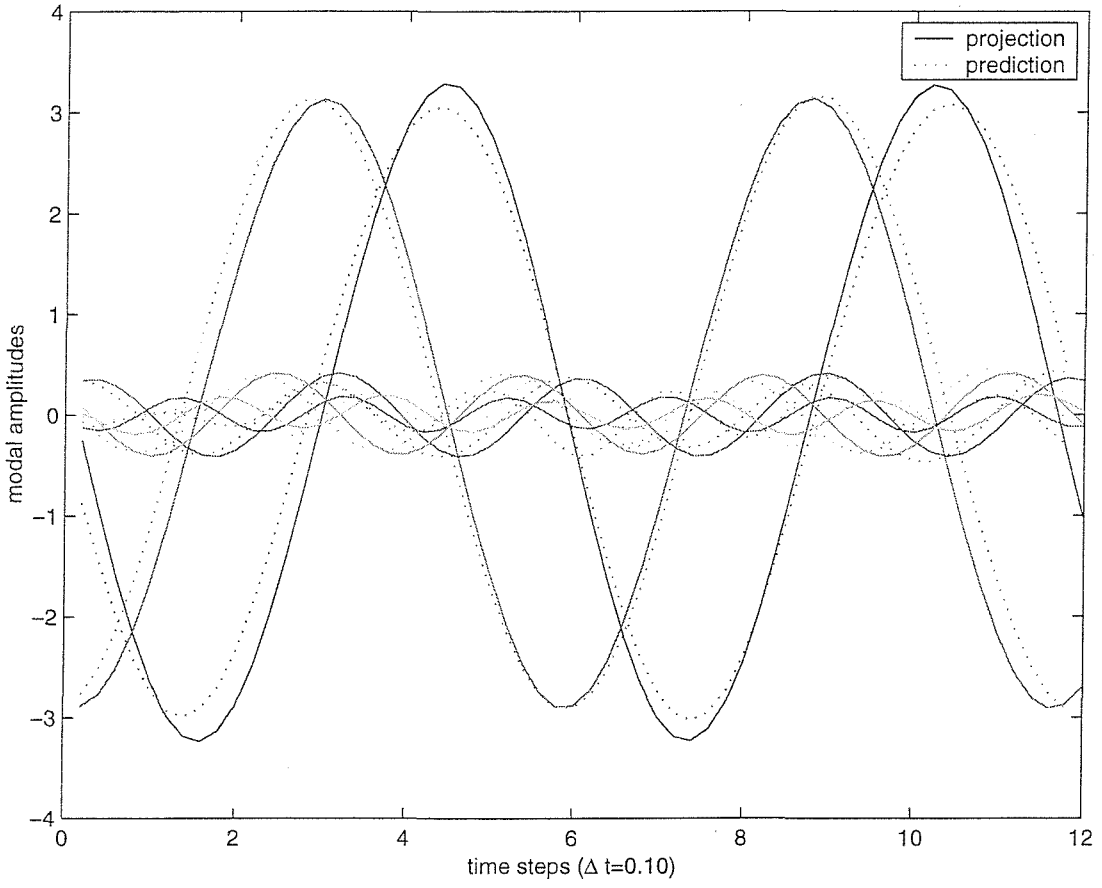

Figure 4.7: Comparison of predicted and projected modal amplitudes for $R_e = 100$ with angular rotation $\gamma = \gamma_0 \sin[\frac{2\pi t}{T_1} + A\pi \sin(\frac{2\pi t}{T_2})]$

Figure 4.6 illustrates the irregularity of the rotation signal assuming a typical parameter set with values $\gamma_0 = 2, T_1 = 6, A = 1, T_2 = 48$. As seen, Graham et al. (1999) used this signal since it yields an excitation frequency from half to twice the shedding frequency. The projection from the modified VCBEM and predictions from the reduced order model agree as shown in Figure 4.7.

In order to further check the efficacy of the reduced order model, rotation input signal $\gamma(t)$ was parameterized by the function,

$$\gamma(t) = \sum_{i=1}^{m} A_i \sin(2\pi i t/T), \tag{4.38}$$

where $A_i, i = 1, 2, \ldots, m$ denote a set of parameter variables.

Figure 4.8 illustrates the irregularity of the rotation signal for a parameter set of values $m = 10$ and $T = 6.0$ with random values of A_i . The results of the comparison between *projection* solutions from the full order Navier-Stokes equations solved using the modified VCBEM and *prediction* solution derived from the control function method of the reduced order model are shown in Figures 4.9 and 4.10. The Figure 4.10 shows the comparison of first four eigen modes and it seen from the figure that the first two predominant modes are congruent with the full order Navier-Stokes equations. The higher modes 3 and 4 agree reasonably well with full order Navier-Stokes and discrepancy is seen modes 5 and 6 as shown in Figure 4.9. It is observed that the reduced order model agrees reasonably well with the full-order Navier-Stokes for the vortex shedding case examined. The energy contribution of higher harmonics is insignificant when compared to that of first two prime modes in vortex shedding case and hence vortex shedding governed by the predominant modes of flow.

If the reduced order model does not or poorly represents the full order Navier-Stokes equations, then the control system designed on the basis of reduced order model will be ineffective when applied to the full order system. Hence, the effectivesness of control strategy designed based on reduced order model depends on the degree of accuracy to which the reduced order model captures the essential dynamics of full order Navier-Stokes. The control function reduced order model developed in the current research for vortex shedding problem represents the dynamics of full order Navier-Stokes flow reasonably well and is hence adopted in the control strategies.

This limited validation of the reduced order model for the optimized control input provides the tools necessary to investigate control of vortex shedding. Feedback and feed forward control techniques provide a way forward and in the next chapter emphasis is focused on how these control techniques can be applied to a real problem and assessment of success.

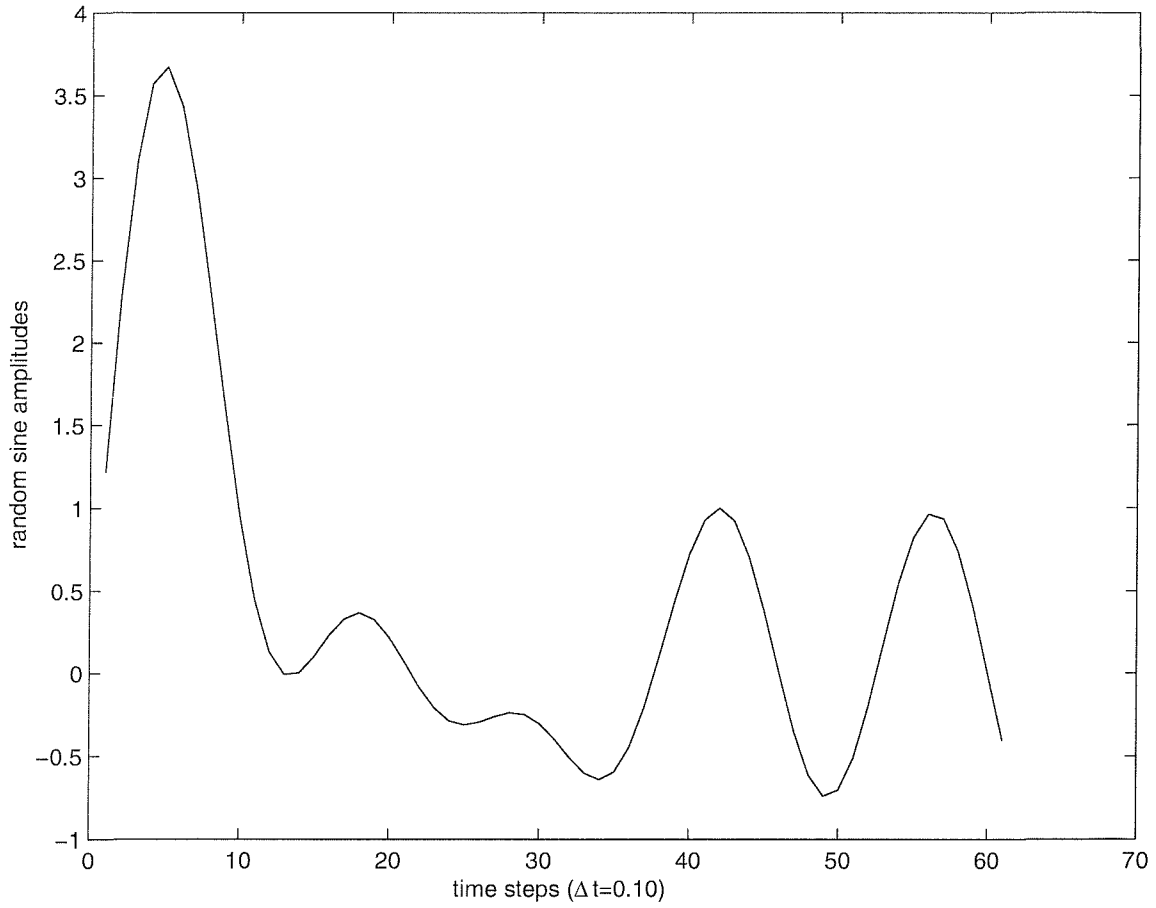

Figure 4.8: Parametric time history of angular rotation γ given by $\gamma(t) = \sum_{i=1}^{m} A_i \sin(2\pi it/T)$

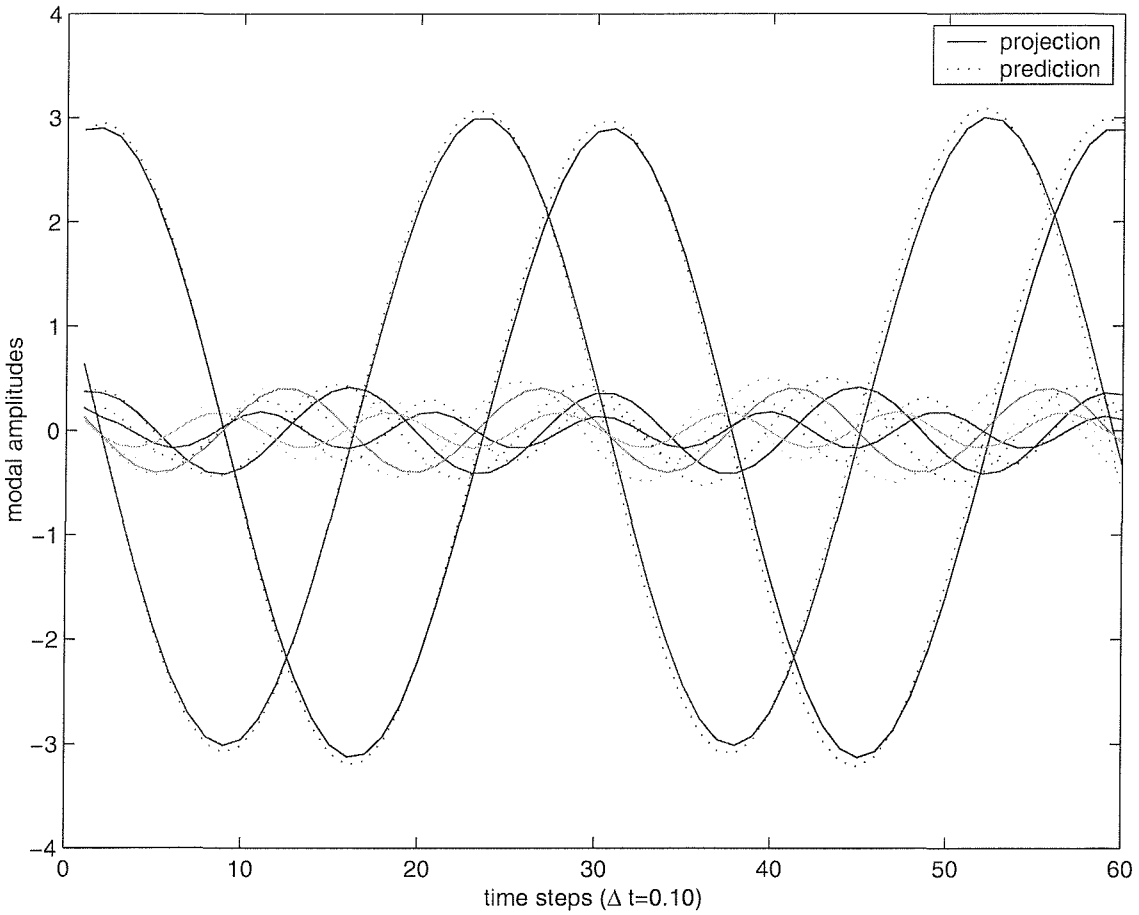

Figure 4.9: Comparison of predicted and projected modal amplitudes for $R_e = 100$ with parametric angular rotation γ given by $\gamma(t) = \sum_{i=1}^{m} A_i \sin(2\pi i t/T)$

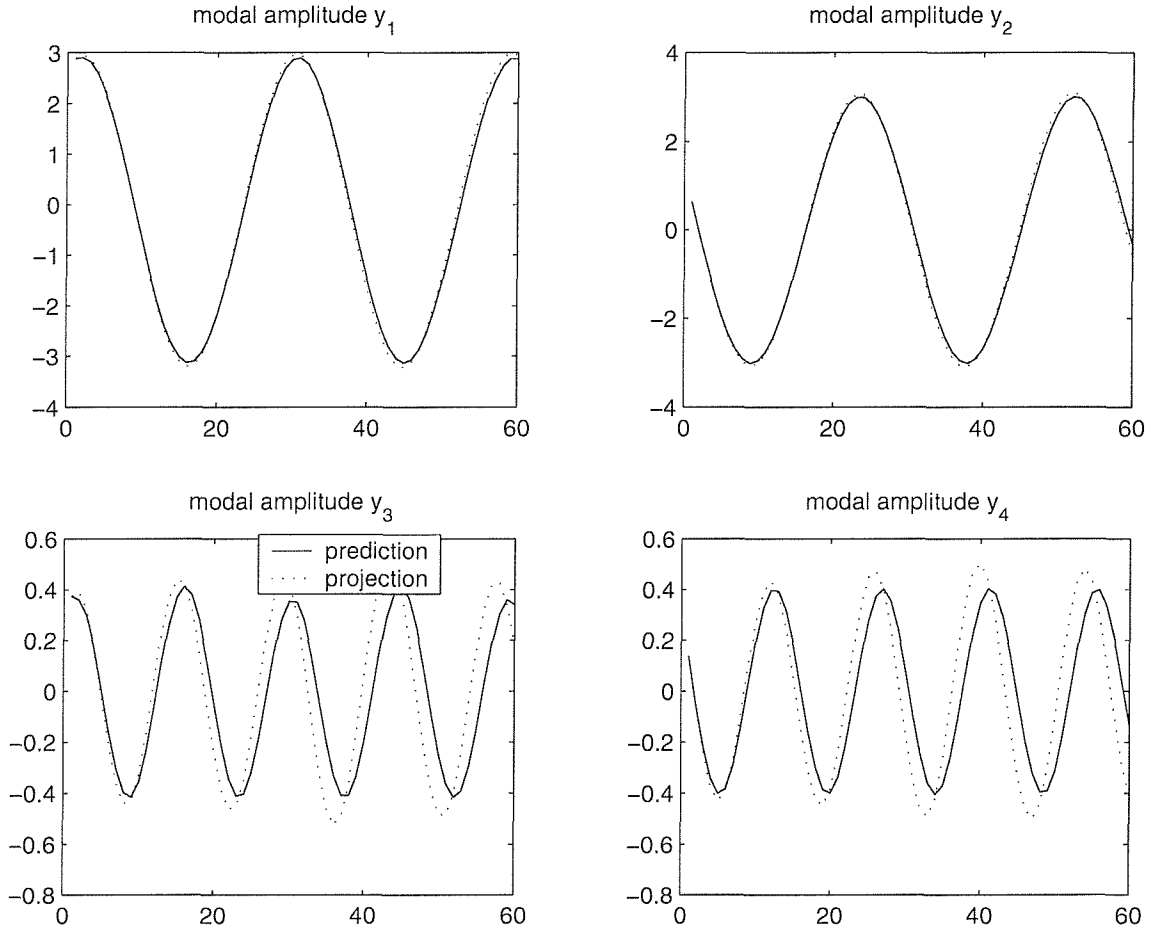

Figure 4.10: Comparison of predicted and projected modal amplitudes of the first four modes for $R_e = 100$ with parametric angular rotation γ given by $\gamma(t) = \sum_{i=1}^{m} A_i \sin(2\pi it/T)$ and time step ($\Delta t = 0.10$)

Chapter 5

Active Flow Control

5.1 Introduction

This chapter describes the application of trust-region augmented reduced order modelling techniques for optimal control of vortex shedding. Our model problem involves suppressing Karman vortex shedding in the wake of a circular cylinder by imparting time-dependent angular velocity to the cylinder. The reduced order model is used in lieu of the full order Navier-Stokes equations to design suboptimal control strategies (Graham et al., 1999). This gives rise to a fundamental problem; the ability of the reduced order model to predict the effects of the control signal on the flow field may deteriorate when the baseline control input is modified during the course of an optimization procedure. In other words, there is no theoretical guarantee that an optimal strategy developed using a reduced order model converges to that computed using the full order Navier-Stokes equations.

This limitation of reduced order models can also be analyzed from the viewpoint of a reduced basis approximation. Clearly, a reduced order model gives accurate predictions only when the actual flow field lies in the subspace spanned by the set of basis functions. However, in practice, this assumption may not hold since the optimum control input may drive the true flow field away from the subspace spanned by the set of baseline basis functions. In particular, an optimal control strategy based on a reduced order model alone may lead to controller spillover effects, which can potentially make the higher modes unstable.

One way to circumvent control spillover is to interleave the full order Navier-Stokes equations and the reduced order model during the optimization process. This strategy is computationally more efficient than an approach using only the full order Navier-Stokes equations, and it also overcomes the accuracy limitations of the reduced order

model. An important issue in developing such a scheme is to ensure that asymptotic convergence to the high fidelity optima is achieved.

Alexandrov et al. (1997) proposed a globally convergent trust-region framework for interleaving exact and approximate objective function models in numerical optimization. A trust-region framework is interpreted as an adaptive method to monitor the amount of optimization achieved using the approximation model, before the high fidelity model is run to check the validity of the current iteration. By comparing the approximation model prediction to the exact value periodically, useful information regarding the accuracy of the reduced order model is obtained. This information can then be employed to decide the move limits (i.e to increase or decrease the adaptive radius δ at each iteration) to be enforced in the next optimization iteration, as well as to update the approximation model.

More recently, Arian et al. (2000) presented an extension of this approach to optimal flow control. It was shown that, under some mild assumptions on the accuracy of the reduced order model, convergence to the high fidelity optimal solution is guaranteed within the domain boundaries. An attractive feature of this approach is that, by checking the effects of control input on the flow field using high fidelity simulation (at various stages of the optimization iterations), the effects of control spillover are minimized.

The present chapter provides an overview of flow control followed by the development of active flow control strategies. The current chapter develops and discusses the application of trust-region augmented proper orthogonal decomposition models to optimal control of vortex shedding. It includes discussion of both feedforward and feedback control strategies. The basic idea is to compute the undetermined parameters of the controller by minimizing a suitable objective function. Minimization is carried out using trust-region algorithms which allow systematic updating of the reduced order model during the course of the optimization iterations. To demonstrate the effectiveness of the proposed strategies, as an example, a feedforward control strategy to suppress Karman vortex shedding in the wake of a circular cylinder is considered. The active suppression of vortex shedding is achieved by imparting an optimal time-dependent angular velocity to the cylinder. A selection of numerical results are presented for the feedforward control strategy at Reynolds number, $R_e = 100$ and $R_e = 200$.

5.2 Overview Of Flow Control

Flow control theory and application requires a multidisciplinary approach incorporating aspects of fluid dynamics i.e. Navier-Stokes equations, mathematical modelling, computational engineering, numerical methods and control theory. The integration of various disciplines has given rise to appropriate techniques to address fundamental issues and created opportunities for new areas of research. As traditional scientific disciplines individually grow towards maturity, the urge to break the mindset of *outside our area* has gained impetus and advances in integrating activities along interdisciplinary domains have gained momentum (Bewley, 2001). For example, significant developments in control theory in the last few decades have considerably expanded the selection of tools applied to regulate physical and electrical systems (Abergel & Temam, 1990, Bewley, 2001). The classification of flow control schemes are based on many different criteria such as, the distance to wall (Townsend, 1961, Bakewell & Lumley, 1967, Townsend, 1970, Lumley, 1971, Williamson, 1985, Aubry et al., 1988, Robinson, 1991), energy expenditure (Gad-el Hak, 1996, Ravindran & Ito, 1998, Ravindran, 1999, Graham et al., 1999) or classification based on the control scheme directly modifying the shape of instantaneous/mean velocity profile or selectively influencing small dissipative eddies (Schlicthing, 1932, Lumley, 1971, Sirovich, 1987).

Depending upon the control loop involved and energy expenditure, the flow control can be classified as active or passive control. A control device can be a passive device requiring no auxiliary power or active thus requiring energy expenditure (Gad-el Hak, 1996). Active control can be further divided into predetermined control or reactive control. A predetermined control includes the application of steady or unsteady energy input without regard to the particular state of flow and the control loop is open and no sensors are required in this type of control.

Reactive control is a particular case of an active control mechanism, where the control input is continuously monitored based on measurements of some kind. The control loop can be open (feedforward) or closed (feedback) (Gad-el Hak, 1996, Gillies, 1998, Graham et al., 1999, Bewley, 2001). When dealing with the control of flow structures which convect over the stationary sensors and actuators, distinction between feedforward and feedback is of particular importance.

In a feedforward control, the measured variable and controlled variable may differ (Gad-el Hak, 1996). For example, the pressure or velocity can be sensed in the upstream flow and the resulting signal, in accordance with an appropriate control law, can be used to trigger the actuator downstream, which in turn influences the velocity at a downstream position (Gad-el Hak, 1996, Gillies, 1998, Bewley, 2001).

In the case of a feedback control, it is a necessity that the controlled variable be measured, fedback and compared with a reference input. Reactive feedback control strategies are further classified into four categories, depending on the extent to which they are based in the governing equations as, adaptive, physical, model-based and optimal control (Moin & Bewley, 1994). All three categories, apart from adaptive control, can be used in a feedforward mode or a combined feedforward-feedback mode. A detailed review of the methods of flow control is given by Gad-el Hak (1996), Bewley (2001).

In feed forward control the measured variable is sensed using a sensor and the sensed information is incorporated in a signal which is fed forward (Graham et al., 1999, Gad-el Hak, 2000) where as a feed back control is a closed loop control where the controlled variable is measured and fed back in comparsion to a reference input (Gad-el Hak, 2000, Sahjendra et al., 2001). Models and controllers are developed in adaptive schemes via some learning algorithum without regard to flow physics. System indentification is carried out independently of the flow dynamics or Navier-Stokes equations that govern these dynamics. In an adaptive controller a specified performance index is tried to be optimised by providing a control signal to an actuator (Gad-el Hak, 1996, 2000).

5.2.1 Control of wake of circular cylinder

The flow control of a circular cylinder, which is an archetypal unstable flow, has received a great deal of attention because of its wide range of applications in civil, aeronautical, mechanical and chemical engineering. The application ranges over the spectrum from noise and vibration control, improvement in mixing of chemicals, dynamic stall control and lift enhancement (Gillies, 1998, Cortelezzi, 1996).

The response of a cylinder to a fluid flow, and absolutely unstable wake flows in general, to a periodic forcing above a threshold amplitude possesses the characteristics of a nonlinear oscillator with forced oscillations (Detemple & Eckelmann, 1989). The wake of circular cylinder exhibits vortex shedding oscillations that persist purely as a result of flow instability above a critical Reynolds number. It is not caused by internal pressure feedback, noise or external forcing and the flow exhibits self excited oscillations (Gillies, 1998, Karniadakis & Triantafyllou, 1989, Detemple & Eckelmann, 1989) which have significant consequences in the flow control problem. A significant region of absolute instability is present near the wake region and it is a necessary condition for self-excited wakes and global wake oscillations (Karniadakis & Triantafyllou, 1989, Williamson, 1996).

The wake response to open loop forcing can be characterized as 'lock-in' and 'beat' depending upon the forcing frequency being the same or different to the wake frequency. The different forcing techniques used to stimulate the flow and wake response are found to be similar irrespective of the type of external forcing, such as, acoustic excitation, alternate blowing and suction at separation points, vibrating wires, longitudinal or lateral vibrations of cylinders as discussed by Gillies (1998), Karniadakis & Triantafyllou (1989), Detemple & Eckelmann (1989).

Control of global flow oscillations due to absolute instability is difficult, though the von Karman mode is the first global mode to become unstable, but the flow may possess multiple global modes. The attenuation of all these global modes is a necessary requirement for the control of flow as discussed by Monkewitz (1989). For flow regimes at Reynolds number just above the critical value, for self-excited oscillations there is typically only one globally unstable mode, resulting in Karman vortex shedding (Huerre & Monkewitz, 1990). Hence the flow behaviour at each point in a wake is related to every other by a simple phase shift (Park et al., 1994). Linear feedback control of such flows is theoretically possible by means of a single sensor-actuator feedback loop. The use of single point forcing is justified in a convectively unstable flow which can be controlled, because the stability convects in the downstream direction of the source of local initialized impulse (Huerre & Monkewitz, 1990). The study of Ffowcs Williams & Zhao (1989) showed the oscillations to be suppressed at the sensor location, but are, in general exacerbated elsewhere (Roussopoulos, 1993). The result of these investigations lead to the conclusion that points in the wake are therefore not just merely connected via phase shift and so multiple, spatially distributed sensors are needed for flow control (Gillies, 1998).

The cylinder wake being absolutely unstable, is more difficult to characterize by the use of a single sensor, as discussed. The use of multiple sensors in various streamwise locations is a necessity to suppress the multiple global modes, which exist in the absolutely unstable cylinder wake. A configuration involving multiple control sensors and many flow variables at different spatial locations configure the absolute unstable region , but they do complicate the control algorithm and prove to be computationally expensive (Gillies, 1998). Cylinder wake flows are generally dominated by the dynamics of large-scale spatial structures and the dynamics of small-scale spatial structures are relatively unimportant as reported by Gillies (1998). Physical evidence shows that for at least periodically forced vortex streets, absolutely unstable flows can be regarded as low-dimensional. In the experimental studies of periodically forced vortex streets, Detemple & Eckelmann (1989) for cylinder wake flows used 12 modes and Gopalkrishnan et al. (1994) for airfoils adopted 3 modes and a relatively small number

of characteristic spatial structures are observed. Hence, computational limitation is overcome by the use of surrogate reduced order models which capture the essential dynamics of the system.

5.2.2 Choice of cost functions

The behaviour of flow can be controlled using various approaches. Several possible approaches have evolved based on the studies of Abergel & Temam (1990), Burns & Ou (1993), Ou (1996), Ghattas & Bark (1997), Berggren (1998), Bewley et al. (2000) for cost functions, such as,

flow tracking: Where the cost function to be minimized is the velocity field, which should be 'close' to a desired velocity field.

enstrophy minimization: Where vorticity is the cost function to be minimized

dissipation function: Where the cost function to be minimized is the rate at which heat is generated by deformations of the velocity field.

In the current investigation a flow tracking cost function is considered. The design of suitable controller in feedforward control involves the estimation of time history of the control force $c(\boldsymbol{x}, t)$, which minimizes the objective function:

$$f(c) = \int_{t_1}^{t_2} \int_{\Omega_{obs}} |\boldsymbol{v}(c; \boldsymbol{x}, t) - \boldsymbol{v}^d(\boldsymbol{x}, t)|^2 d\Omega dt. \tag{5.1}$$

In the current formulation of vortex shedding problem $\boldsymbol{v}^d(\boldsymbol{x}, t)$ represents the desired state intended to be achieved for a prescribed control input $c(\boldsymbol{x}, t)$ and $\boldsymbol{v}(c; \boldsymbol{x}, t)$ is the solution of two-dimensional Navier-Stokes (NS) equation for the corresponding $c(\boldsymbol{x}, t)$ control input. The desired state, for example, may be chosen as Stokes flow. Ω_{obs} denotes the domain over which the state of the system is observed and the time-interval over which the objective function is computed is represented by $[t_1, t_2]$ (Arian et al., 2000).

The studies have shown that, the time window chosen has to be longer than the Karman vortex shedding period (i.e the inverse of the Strouhal frequency) for the development of a robust control (Homescu et al., 2002, Zhijin et al., 2002).

5.2.3 Control actions

The focus of an optimal flow control problem is the minimization of an objective or cost function which provides a quantitative measure of the desired objective and

depends critically on the solution (optimal solution) that satisfies the governing partial differential equations of the fluid flow (Zhijin et al., 2002).

Flow control investigations involving flow past obstacles/cylinders have been undertaken by Park et al. (1992), Sritharan (1992), Sritharan et al. (1996), Ou (1996). Gunzburger & Manservisi (1999) who implemented an adjoint technique in an idealized distributed control. For boundary control, studies adopting dynamic boundary action to reduce vorticity were conducted by Berggren (1998) and cylinder rotation control action was used to suppress the wake behind the cylinder in the investigations of He et al. (2000), Tokumaru & Dimotakis (1991). Zhijin et al. (2002) demonstrated the complete control of vortex shedding for Reynolds number up to 110. The optimal values of the suction/blowing parameters were found to be insensitive to initial conditions of the model when the control time window was larger than the vortex shedding period of the robust control.

The behaviour of cylinder flow is affected by several different forcing techniques. However at low Reynolds number, the wake response to forcing is similar for each forcing under examination. That is acoustic excitation of wake (Detemple & Eckelmann, 1989, Roussopoulos, 1993), longitudinal or lateral vibrations of cylinder (Detemple & Eckelmann, 1989), rotation of cylinder (Tokumaru & Dimotakis, 1991, He et al., 2000), alternate blowing and suction at separation points (Roussopoulos, 1993) or vibrating wires in the wake (Karniadakis & Triantafyllou, 1989). For vortex shedding suppression, Tokumaru & Dimotakis (1991) involved rotation of the cylinder or Lewit (1992) incorporated a scheme of alternate suction/blowing. These have gained some success as reported by Gillies (1998).

5.3 Feedforward Control Strategy

The trust-region augmented proper orthogonal decomposition modelling approach for feedforward control of vortex shedding is now developed and it is subsequently extended to design optimal feedback control schemes.

In feedforward control, the design of a suitable controller involves determining the time history of the control force $c(\boldsymbol{x}, t)$, which minimizes the objective function:

$$f(c) = \int_{t_1}^{t_2} \int_{\Omega_{obs}} |\boldsymbol{v}(c; \boldsymbol{x}, t) - \boldsymbol{v}^d(\boldsymbol{x}, t)|^2 d\Omega dt. \tag{5.2}$$

In this formulation $\boldsymbol{v}(c; \boldsymbol{x}, t)$ is the solution of the two-dimensional Navier-Stokes (NS) equations for prescribed control input $c(\boldsymbol{x}, t)$ and $\boldsymbol{v}^d(\boldsymbol{x}, t)$ is a desired state in the vortex shedding problem. For example, the latter may be chosen to be a Stokes flow.

The domain over which the state of the system is observed is denoted Ω_{obs} and $[t_1, t_2]$ is the time-interval over which the objective function is computed as discussed by Arian et al. (2000).

If the full order Navier-Stokes equations are used to compute $\boldsymbol{v}(\boldsymbol{x}, t)$, minimization of $f(c)$ is a computationally expensive problem. An alternative approach using a reduced order model as a surrogate for the full order state equations allows the approximate objective function to be defined as

$$m(c) = \int_{t_1}^{t_2} \int_{\Omega_{obs}} |\boldsymbol{v}^{pod}(c; \boldsymbol{x}, t) - \boldsymbol{v}^{d}(\boldsymbol{x}, t)|^2 d\Omega dt \tag{5.3}$$

where $\boldsymbol{v}^{pod}(c; \boldsymbol{x}, t)$ is the solution of the proper orthogonal decomposition reduced order model for control input $c(\boldsymbol{x}, t)$.

Note that the reduced order model is constructed using the flow snapshots obtained by solving the Navier-Stokes equations for given $c(\boldsymbol{x}, t)$. In general, the accuracy of the approximate objective function $m(c)$ tends to deteriorate when the control input is changed significantly from the baseline $c(\boldsymbol{x}, t)$. Hence, for two arbitrary control inputs c_1 and c_2, $m(c_2) < m(c_1)$ does not imply that $f(c_2) < f(c_1)$. This suggests that a naive strategy based on minimization of $m(c)$ alone may not lead to minimization of the full order objective function $f(c)$. In order to ensure that we are minimizing the actual objective function $f(c)$, therefore it is necessary for the optimization strategy to interleave both the full order and reduced order objective function predictions.

For example, let $c_0(\boldsymbol{x}, t)$ denote an initial guess of the optimal control input at which the full order Navier-Stokes equations are solved to obtain a set of flow snapshots. These snapshots may be used to construct a reduced order model of the flow. The next step involves determining the control input $c_1(\boldsymbol{x}, t)$ which minimizes the surrogate objective function given in equation 5.3. In order to improve the reduced order model, the full order Navier-Stokes equations are solved using $c_1(\boldsymbol{x}, t)$ as the control input, to compute a new set of flow snapshots, which are then used to construct an updated reduced model. This iterative process continues until no further reduction in $f(c)$ is achieved. If reasonably tight move limits are placed on the control input amplitudes, this procedure *may* converge close to the optima of the full order objective function $f(c)$.

This sequential approximation model updating strategy has been used in the design optimization literature to reduce the computational cost of numerical optimization (Rodriguez et al., 1998). From a theoretical viewpoint, there is no guarantee that the sequential iterative procedure described converges to the minima of $f(c)$. Recently,

Alexandrov et al. (2000) proposed a trust-region framework to integrate variable-fidelity analysis models in nonlinear programming formulations. This framework is theoretically guaranteed to converge to the minima of $f(c)$ provided at the beginning of each iteration, the objective function and its gradient computed using the full order and the reduced order model agree with each other.

Arian et al. (2000) presented an application of the trust-region framework to optimal flow control. The optimal control strategy used in this thesis is based on this framework. For a detailed exposition of trust-region frameworks and global convergence results, the reader is referred to Alexandrov et al. (1997, 2000) and Arian et al. (2000). Global convergence analysis of trust-region methods for nonlinear programming problems with general constraints have been presented by Rodriguez et al. (1998). Hence, trust-region methods can also be applied to cases when the optimal control problem is modified to incorporate constraints on the controller energy requirements and robustness to parametric uncertainties. Here a brief overview of the trust-region algorithm for unconstrained problems is described, with emphasis on those aspects which differ from earlier studies.

To enable the application of numerical optimization schemes, it is first required to parameterize the control input $c(\boldsymbol{x}, t)$ using a finite number of optimization variables, i.e.,

$$c(\boldsymbol{x}, t) = \mathcal{N}(\boldsymbol{\theta}, \boldsymbol{x}, t), \tag{5.4}$$

where $\boldsymbol{\theta}$ denotes the vector of optimization variables which is to be computed by minimizing equation 5.2. Henceforth, the objective function computed using the full order and reduced order models will be explicitly denoted as a function of $\boldsymbol{\theta}$.

The trust-region procedure guarantees the convergence of the variable-fidelity modelling approach by reformulating the optimization problem as

$$\textbf{Minimize}: \quad m_k(\boldsymbol{\theta}_k + s), \tag{5.5}$$

$$\textbf{Subject to}: \quad ||s|| \leq \delta_k, \tag{5.6}$$

where $||.||$ is L_∞ and the minimization is carried out with respect to s. $\boldsymbol{\theta}_k$ denotes the parameter values used in equation 5.4 to generate snapshots (i.e., by solving the full order Navier Stokes equations for control input $c_k = \mathcal{N}(\boldsymbol{\theta}_k, \boldsymbol{x}, t)$) for constructing the reduced order model. δ_k denotes the trust-region radius at iteration number k. $m_k(\boldsymbol{\theta}_k + s)$ is the objective function based on the reduced order model, which is constructed using flow snapshots computed for control input $c_k = \mathcal{N}(\boldsymbol{\theta}_k, \boldsymbol{x}, t)$. The subscript k is used to indicate that the reduced order model is updated at each iteration.

Let $\boldsymbol{\theta}_0$, δ_0, $0 < \eta_1 < \eta_2 < 1$, and
$0 < \gamma_1 \leq \gamma_2 < 1 \leq \gamma_3$ be given.
Set k = 0.

Step 1: Solve the full order state equations for flow snapshots corresponding to control input $c_k = \mathcal{N}(\boldsymbol{\theta}_k, \boldsymbol{x}, t)$ and compute $f(\boldsymbol{\theta}_k)$.
Step 2: Compute POD basis functions, build the reduced order model and compute $m_k(\boldsymbol{\theta}_k)$.
Set $\beta_k = f(\boldsymbol{\theta}_k)/m_k(\boldsymbol{\theta}_k)$.
Step 3: Compute s_k by minimizing the objective function $\beta_k m_k(\boldsymbol{\theta}_k + s)$, subject to the trust-region constraint $||s|| \leq \delta_k$.
Step 4: Compute $f(\boldsymbol{\theta}_k + s_k)$ by solving the full order state equations. Set $\rho_k = \delta f / \delta m_k$, where $\delta f = f(\boldsymbol{\theta}_k) - f(\boldsymbol{\theta}_k + s_k)$ and $\delta m_k = m_k(\boldsymbol{\theta}_k) - m_k(\boldsymbol{\theta}_k + s_k)$.
Step 5: If convergence criteria are satisfied stop. Else update the trust-region radius to δ_{k+1}.
Set $k = k + 1$.
- If $\rho_k > \eta_1$ set $\boldsymbol{\theta}_{k+1} = \boldsymbol{\theta}_k + s_k$ and go to Step 1.
- If $\rho_k \leq \eta_1$ set $\boldsymbol{\theta}_{k+1} = \boldsymbol{\theta}_k$ and go to Step 3.

Figure 5.1: Trust-region augmented variable-fidelity optimization algorithm

The basic idea of the trust-region approach is to increase or decrease the adaptive radius δ_k (or move limits) at each iteration, depending on how well $m(\boldsymbol{\theta}_k)$ correlates with $f(\boldsymbol{\theta}_k)$. In general, at the beginning of each iteration k, $m_k(\boldsymbol{\theta}_k) \neq f(\boldsymbol{\theta}_k)$ and $\nabla m_k(\boldsymbol{\theta}_k) \neq \nabla f(\boldsymbol{\theta}_k)$. Arian et al. (2000) showed that convergence to the minima of $f(\boldsymbol{\theta})$ can still be guaranteed under some assumptions placed on the gradient of $m(\boldsymbol{\theta})$, i.e., when ∇m_k approximates to ∇f sufficiently well within the limit. Since we do not have a theoretical bound on how well ∇m_k approximates to ∇f, it is difficult to validate and guarantee global convergence for a given problem. Nevertheless, in practice, convergence close to a local optima can often be obtained in a computationally efficient fashion, even if the consistency conditions are not satisfied.

In the present investigation zero-order consistency conditions are imposed on the approximate objective function $m(\boldsymbol{\theta}_k)$. This involves computing a constant β_k, such that at each iteration k, $\beta_k m_k(\boldsymbol{\theta}_k) = f(\boldsymbol{\theta}_k)$. The motivation for this is to improve the accuracy of the objective function predicted using the reduced order model. It is expected that this leads to accelerated convergence as compared to the approach used by Arian et al. (2000), who used first order consistency conditions. It is important to

note that, if an adjoint Navier-Stokes solver is available, then it is possible to choose scaling parameters such that the condition $\nabla m_k(\boldsymbol{\theta}_k) = \nabla f(\boldsymbol{\theta}_k)$ is also satisfied. This is expected to lead to a further improvement in the accuracy of the cost function predicted by the reduced order model.

The steps involved in the trust-region augmented variable-fidelity optimization algorithm are summarized in Figure 5.1. Note that in Step 5, the step s_k is rejected if it leads to an increase in the high fidelity objective function. The trust-region radius update strategy in Step 5 is based on the following procedure:

- If $\rho_k \leq \eta_1 : \delta_{k+1} = \gamma_1 \delta_k$.
- If $\eta_1 < \rho_k < \eta_2 : \delta_{k+1} = \gamma_2 \delta_k$.
- If $\rho_k \geq \eta_2 : \delta_{k+1} = \gamma_3 \delta_k$.

In the current numerical study $\eta_1 = 0.25$ and $\eta_2 = 0.75$ as proposed by Alexandrov et al. (1997). Arian et al. (2000) suggested that γ_1, γ_2, and γ_3 should be set at 0.5, 0.5, and 2, respectively.

In practice, an approximate solution of the optimization problem in Step 3 is sufficient to achieve convergence to the high fidelity optima. In the present investigation, only a few steps of the limited memory Broyden-Fletcher-Goldfarb-Shanno (BFGS) algorithm (Zhu et al., 1997) were found necessary to compute the optimal value of s_k at each iteration and the trust-region constraint adopted is based on the L_∞ norm defined in equation 5.6. This allows the trust-region constraint to be satisfied by simply changing the bound constraints based on the value of δ_k. Hence, this choice of the norm makes it easier to implement the trust-region framework using existing optimization routines capable of handling bound constraints.

5.4 Feedback Control Strategy

In the case of feedback control, the control input depends on the instantaneous state of the system. Therefore use is made of a parameter defined feedback controller of the form

$$\gamma(t) = \mathcal{N}(\alpha, y_1(t), y_2(t), \ldots, y_n(t)). \tag{5.7}$$

Here $y_i(t), i = 1, 2, \ldots, n$ describe the projection of the instantaneous flow field onto a set of n basis functions at time t, and α is a vector of undetermined controller parameters.

For the purpose of illustration, consider the case when a neurocontrol strategy is employed as discussed by Suykens et al. (1995). That is, the function $\mathcal{N}$ is chosen to be a neural network model. In this case, the elements of the undetermined parameter vector α become the weights of the neural network model. More specifically, the controller is characterized using a linear combination of kernels, i.e.,

$$\mathcal{N}(y) = \sum_{i=1}^{n} \alpha_i \sigma(a_i), \quad a_i = \sum_{j=1}^{p} w_{ij} y_j + \aleph_i, \tag{5.8}$$

where α, w and $\aleph$ are model parameters representing the weights and bias terms of the network. $\sigma(y)$ is a transfer function which is typically chosen to be S-shaped i.e. a sigmoid defined by the expression $(1+e^{-y})^{-1}$ or the hyperbolic tangent function. This is traditionally used in the neural network literature to facilitate non-linear modelling (see Bishop (1995)).

Using this parameter defined controller, the reduced order closed loop system can be written as

$$\frac{dy_i}{dt} = a_i + \sum_{j=1}^{N} b_{ij} y_j + \sum_{j=1}^{n} \sum_{k=1}^{n} c_{ijk} y_j y_k +$$

$$d_i \frac{\partial \mathcal{N}}{\partial t} + (e_i + \sum_{j=1}^{n} f_{ij} y_j)\mathcal{N} + g_i \mathcal{N}^2. \tag{5.9}$$

Note that the computation of $\partial \mathcal{N}/\partial t$ involves calculating the derivative of the neural network model with respect to its inputs, i.e., y_i. This is efficiently achieved using procedures described by Bishop (1995). Hence, given the values of the undetermined model parameters α, w and $\aleph$, the evolution of the modal amplitudes of the closed loop response $y_i(t)$ are readily computed using a time marching scheme. To estimate the neural network model parameters, it is proposed to minimize the cost function described in the previous section. Note that this cost function can be computed using the full order Navier-Stokes equations as well as the reduced order model.

It is observed that there are several differences between the proposed approach and the neurocontrol strategy investigated by Gillies (1998) for the same model problem considered here. Gillies trained a neurocontroller by solely employing an approximate system model which was chosen to be a neural network emulating the proper orthogonal decomposition reduced order model. In the case of Gillies (1998) no attempt was made to validate the controller by applying the feedback controller to the full order Navier-Stokes equations. It is likely that the control strategy may fail due to model uncertainties that arise from the use of neural networks to approximately represent

the system dynamics. In order to overcome this, the controller design algorithm has to accomodate model uncertainty.

It is worth noting that if the control parameters are estimated solely on the basis of the approximate cost function, control spillover is highly likely. As a result, the closed loop system may become unstable due to the excitation of higher modes which are neglected in the proper orthogonal decomposition model. To circumvent this, it is suggested that trust-region algorithms can be employed to estimate the controller parameters in equation 5.8. The trust-region framework presented earlier in the context of feedforward control can be readily applied. The only difference is that the cost function is now computed using the closed-loop model of the full order Navier-Stokes equations and the reduced order model. Further studies are require to investigate whether this strategy leads to controllers that are tolerant to modelling uncertainties.

5.5 Computed Results

A selection of numerical studies are presented demonstrating suppression of vortex shedding in the wake of a circular cylinder. Time-dependent boundary conditions within the VCBEM method were validated for the cylinder subject to imposed time-dependent angular velocity. In Chapter 3 it is shown that the Strouhal number and the flow field predicted by the VCBEM method agreed favourably with the values predicted by the finite element scheme of Graham et al. (1999) for Reynolds number, $R_e = 100$ and $R_e = 200$.

Subsequently, the proper orthogonal decomposition reduced order model based on the control function approach was implemented. The approximate model was validated for the case of $\gamma(t) = 2sin(\pi t/3)$ by using the snapshots generated by executing the modified VCBEM full order code. The Figure 5.2 shows the first ten normalized eigen values of covariance matrix for the generated snapshots of modified VCBEM. Figure 5.3 shows that the amplitudes of predicted and projected basis function agree reasonably well. It is found that the first 6 modes capture 99.84 % of the flow energy. From this set of results, it can be observed that the reduced order model agrees reasonably well with solutions derived from the full order Navier-Stokes equations for this particular control input.

After validating the full order and reduced order models as explained in Chapter 4, numerical studies were undertaken to analyze feedforward control of vortex shedding. The control input as defined by the time dependent amplitude of rotation $u(t)$, is

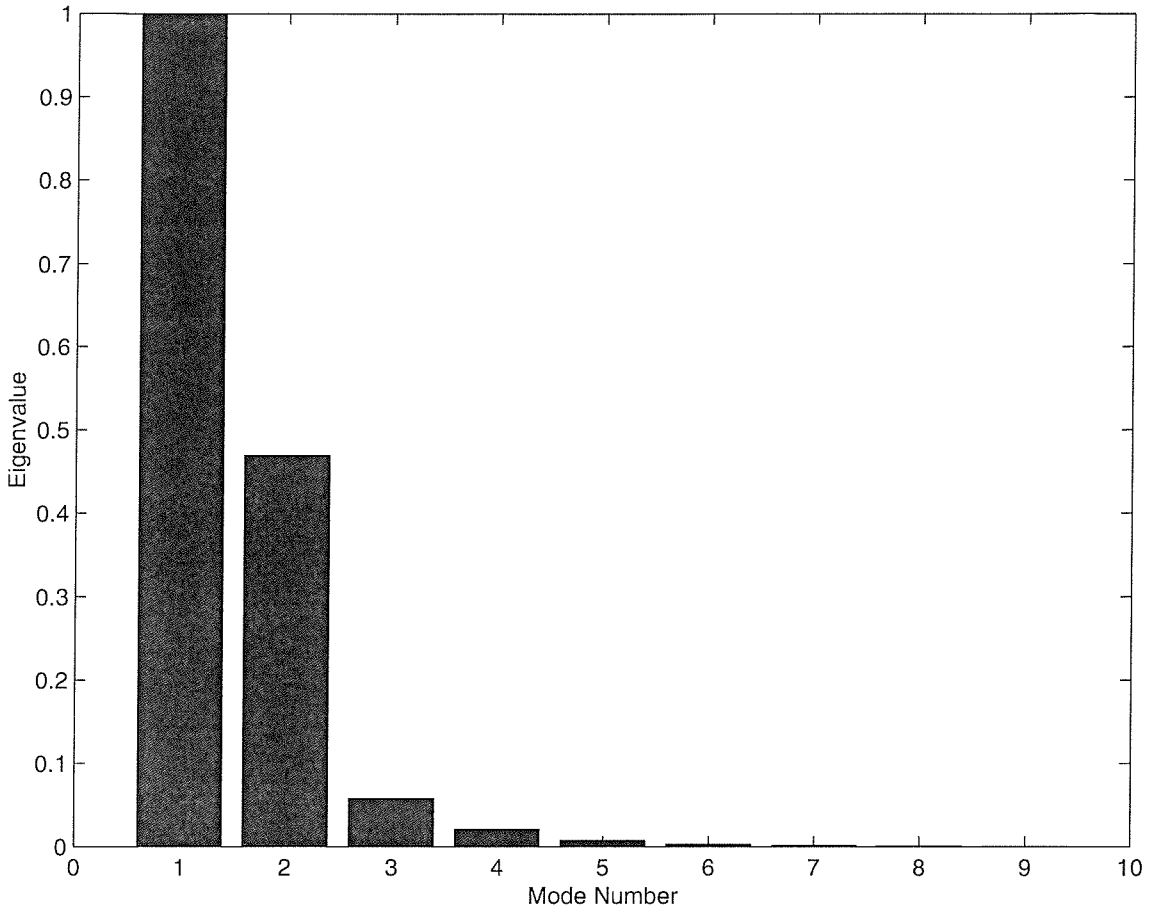

Figure 5.2: Eigenvalues of the correlation matrix.

characterized by the function

$$u(t) = \sum_{i=1}^{m} A_i \sin(2\pi it/T), \tag{5.10}$$

where $A_i, i = 1, 2, \ldots, m$ denote a set of optimization variables.

The number of parameters m and size of the time window T determine the computational cost of the flow simulations. As explained in Chapter 4, the minimum sampling rate for vortex shedding phenomenon governed by the lift signal, is the Nyquist rate, which is the maximum frequency and at least twice the maximum frequency should be selected as the upper limit of the frequency spectrum (Graham et al., 1999, Gillies, 1998, Ravindran, 1999, Homescu et al., 2002). The time window chosen has to be longer than the Karman vortex shedding period (i.e the inverse of the Strouhal frequency) for the development of a robust control (Homescu et al., 2002, Zhijin et al., 2002). When the time window chosen is lesser than that of Karman vortex shedding

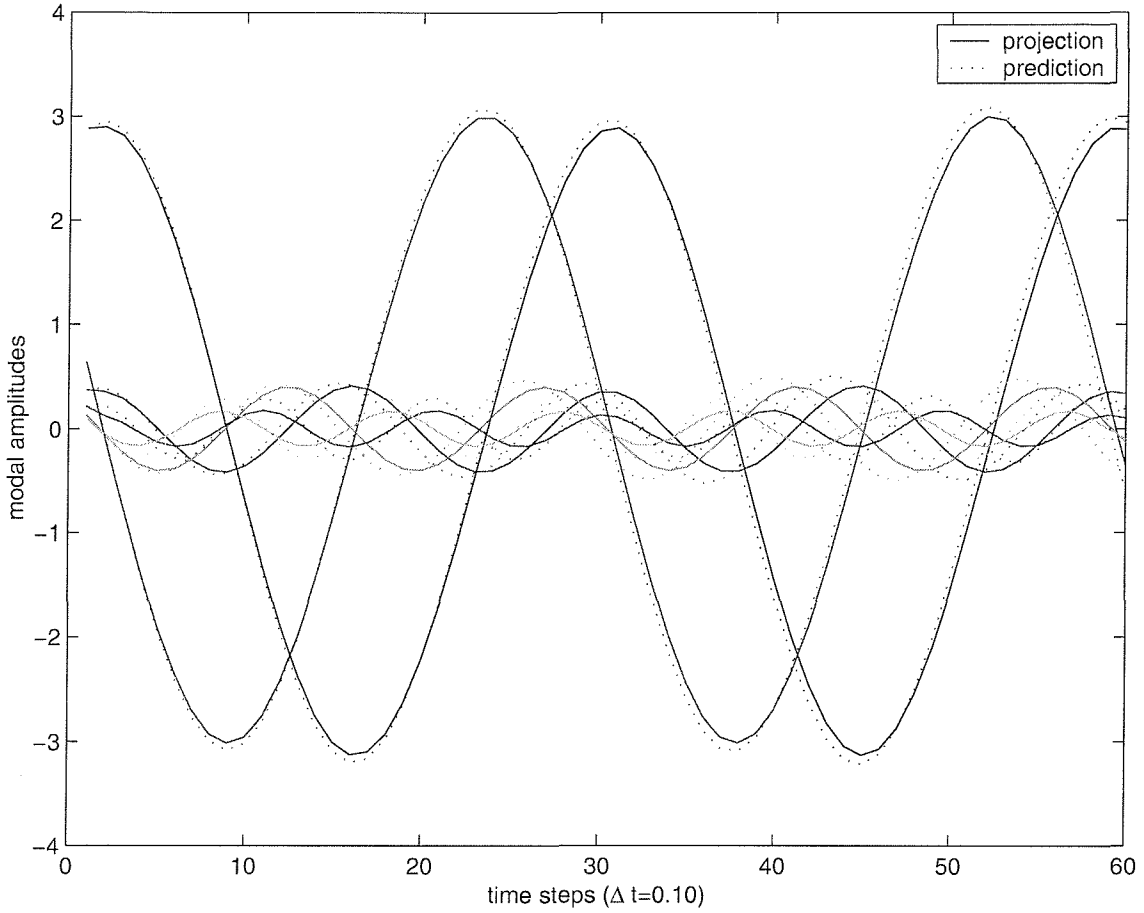

Figure 5.3: Comparison of predicted and projected modal amplitudes for Reynolds number $R_e = 100$ and angular rotation $\gamma = 2\sin(\pi t/3)$.

period, the optimal control parmeters depend on the initial conditions and hence it is a necessary condition for robust control that the time window chosen has to be longer than the Karman vortex shedding period of the flow system. The control parameters will be insensitive to initial conditions when time window chosen is longer than that of Karman vortex shedding period and Zhijin et al. (2002) found the suction/blowing parmeters to be insensitive for this criteria of time window.

In the present study, parameter values $m = 10$ and $T = 6$ were assumed and the time window for achieving control was set at $[0, 6]$ seconds. Note that by increasing m, the flexibility with which the control input is represented can be improved. However, this leads to larger number of optimization variables with an attendant increase in the computational cost. In current simulations, $m = 10$ was found to be a reasonable choice since it provides a reasonably flexible parmeterization of the control input. The control objective was to achieve steady flow throughout the computational domain, with $v_1 = 1.0$ and $v_2 = 0.0$. The initial estimate for the variables A_i is set to zero. The

proper orthogonal decomposition model was constructed using six modes throughout the trust-region iterations.

The proposed strategy is tested for its domain of applicability and the results are presented for two cases:

- Control window at the start of flow.
- Control window at the steady flow with vortex shedding.

5.6 Results: Control Window at Start of Flow

The optimal control input obtained after two trust-region iterations for this case is shown in Figure 5.4. The time histories of the flow field fluctuations (in a mean-square sense, i.e., the normalized least-squared difference between the current and the desired flow fields) for the controlled and uncontrolled flows are compared in Figure 5.5 for $R_e = 100$.

Similar studies were undertaken for the case of $R_e = 200$. The optimal control input obtained after the trust-region iterations, as explained in Figure 5.1, is shown in Figure 5.6. The instantaneous variations in the plot of fluctuations for the controlled and uncontrolled flows are shown in Figure 5.7.

It is observed from this information that in the *time window under consideration*, on average, approximately 51% reduction in the flow unsteadiness is achieved. Homescu et al. (2002) adopted flow tracking as the objective function and He et al. (2000) adopted the drag reduction as cost function. The studies were found to be consistent with experimental results of Tokumaru & Dimotakis (1991). The studies reported that for spinning cylinders at $R_e = 200$ and $R_e = 1000$ show a reduction of 31% and 61% respectively as compared with fixed cylinder. Figures 5.8 and 5.9 for $R_e = 100$ and Figures 5.10 and 5.11 for $R_e = 200$ clearly show the influence of the control strategy on the flow regimes.

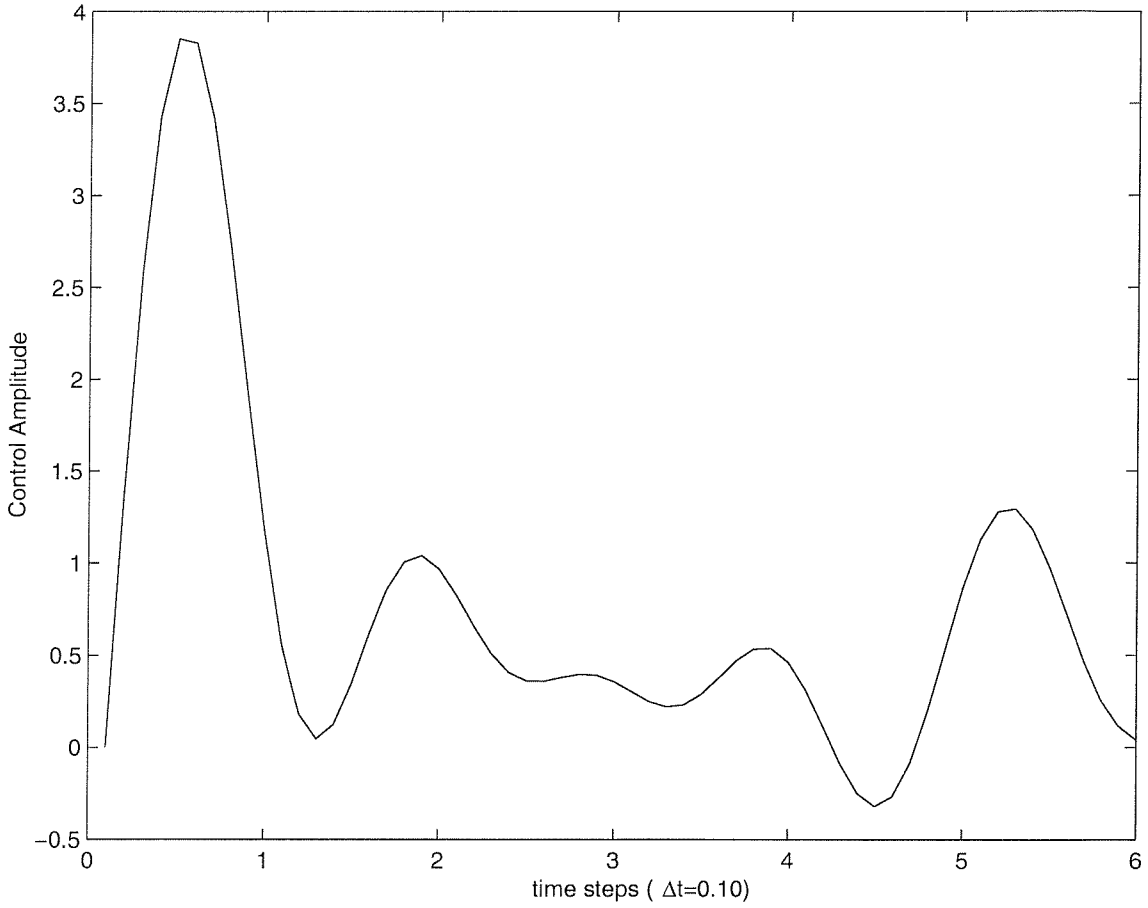

Figure 5.4: Optimal control input for $R_e = 100$ in the time-interval $[0, 6]$ seconds.

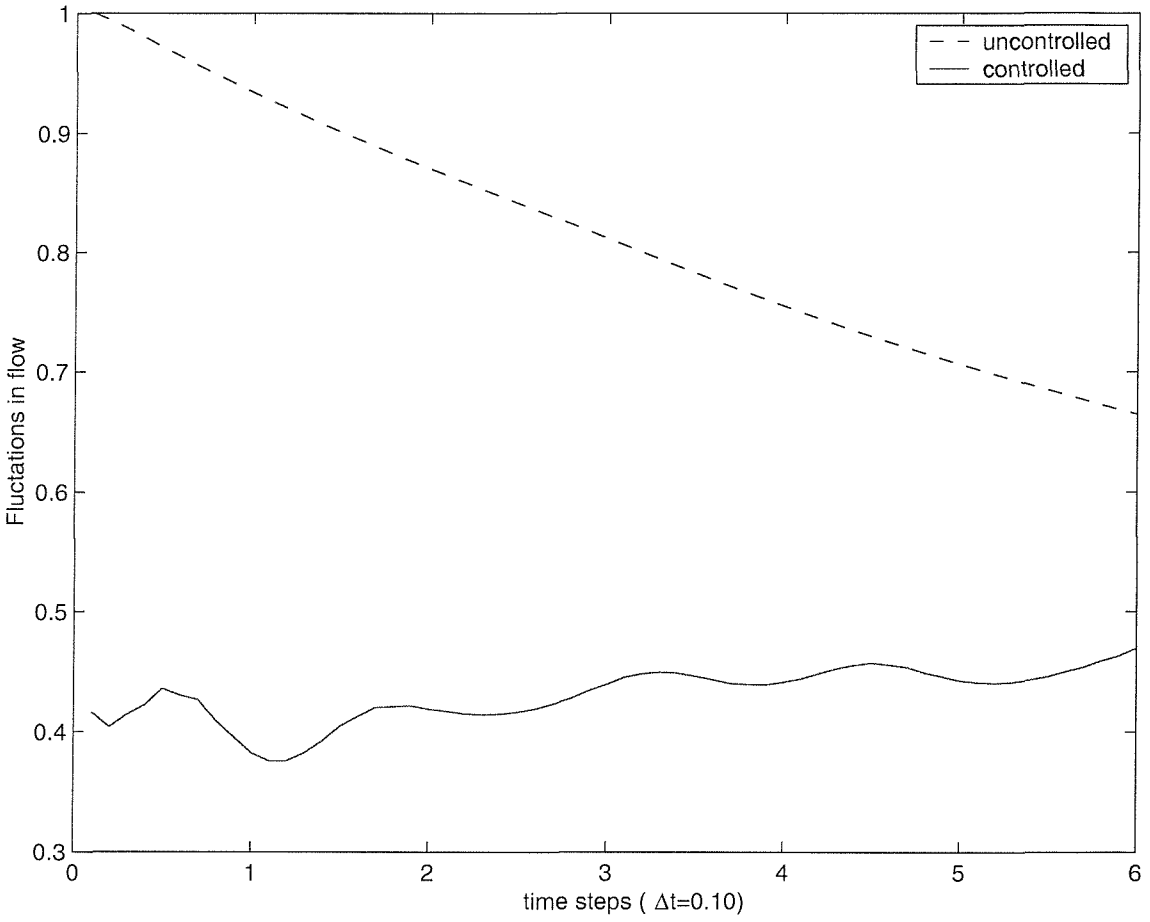

Figure 5.5: Comparison of the time history of flow fluctuations in a mean-square sense for uncontrolled and controlled cases; $R_e = 100$ within the time interval $[0, 6]$ seconds only.

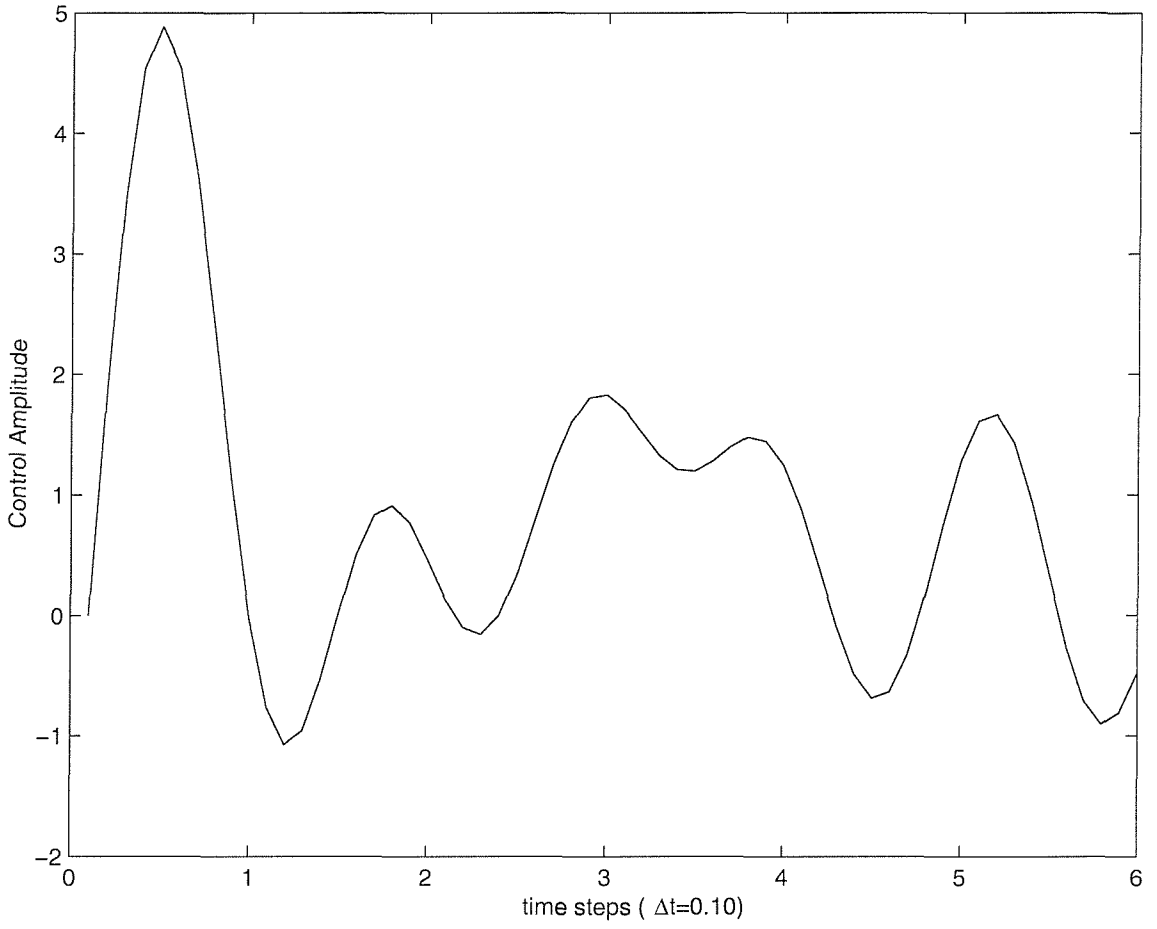

Figure 5.6: Optimal control input for $R_e = 200$ in the time-interval $[0, 6]$ seconds.

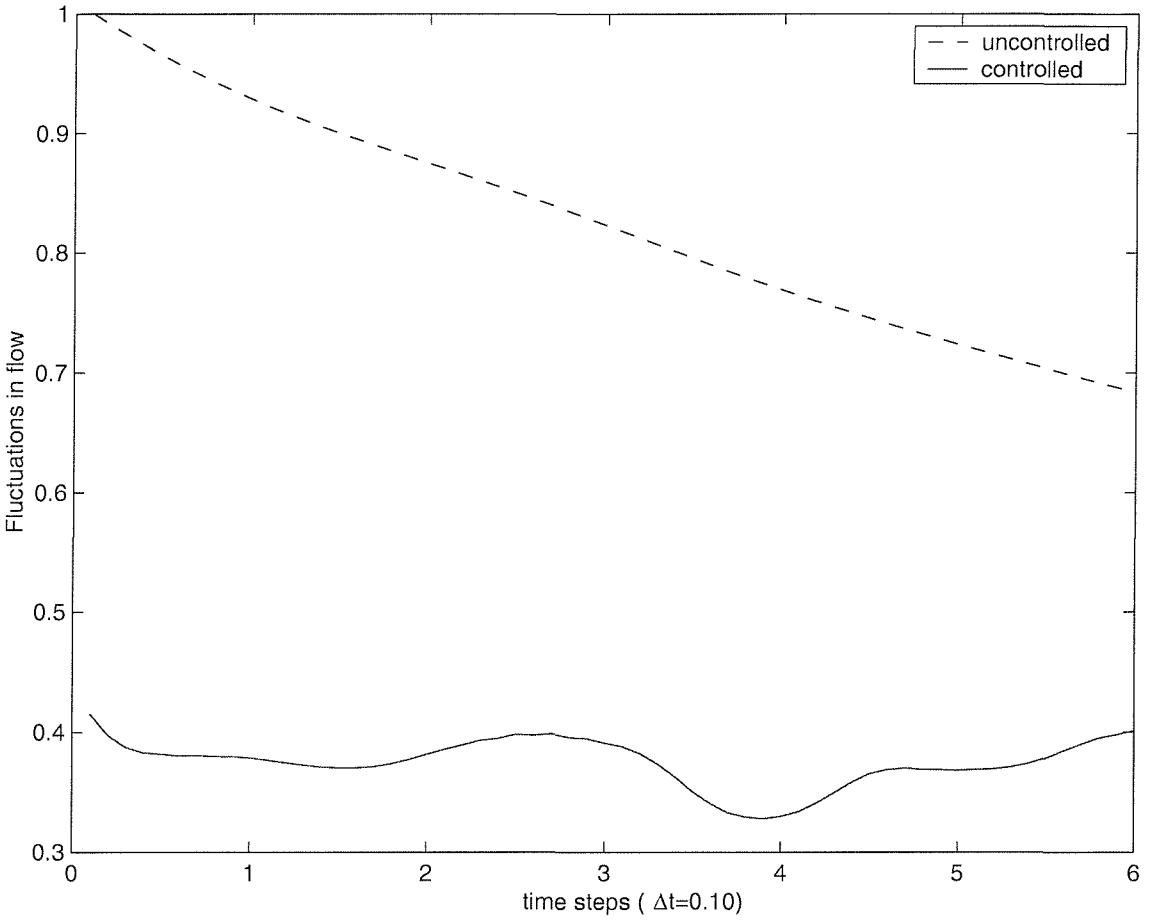

Figure 5.7: Comparison of the time history of flow fluctuations in a mean-square sense for uncontrolled and controlled cases; $R_e = 200$ within the time interval $[0, 6]$ seconds only.

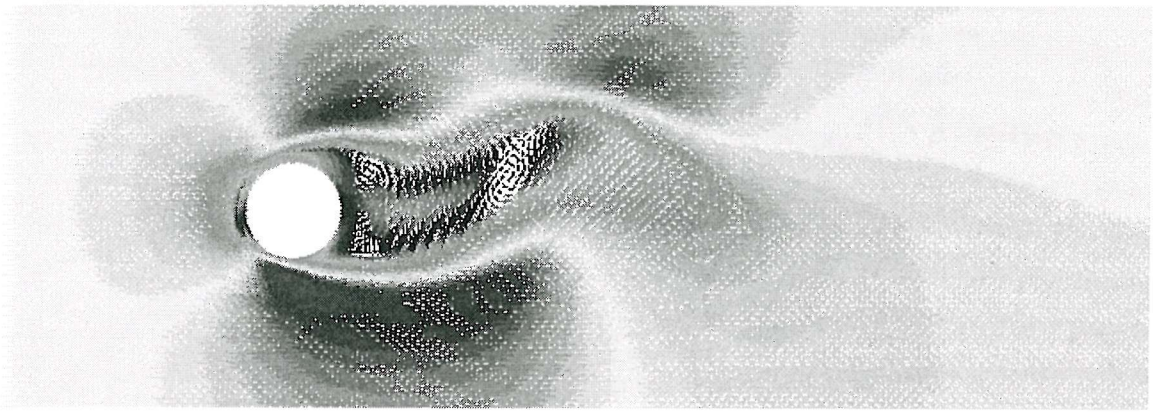

Figure 5.8: Velocity flow field for $R_e = 100$ without control at time $t = 6$ seconds in the time interval $[0, 6]$ seconds.

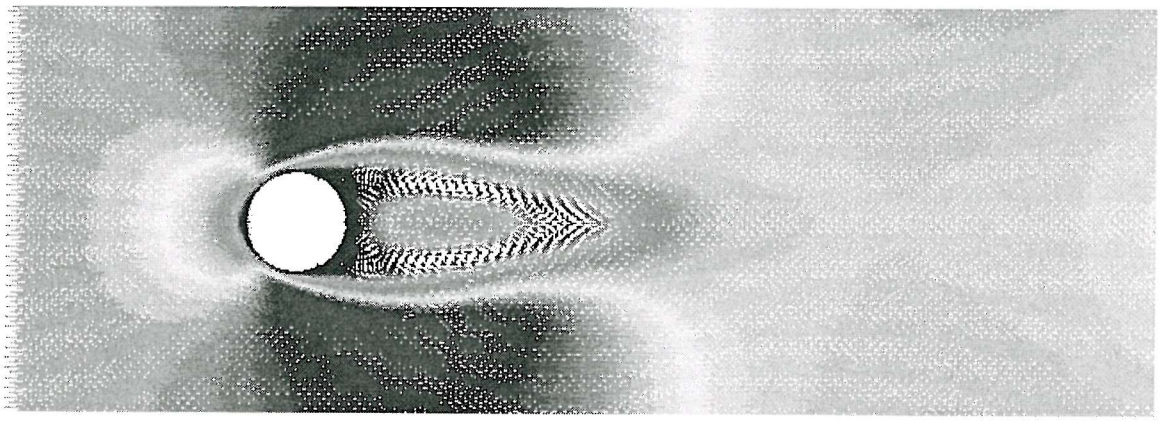

Figure 5.9: Velocity flow field for $R_e = 100$ with control at time $t = 6$ seconds in the time interval $[0, 6]$ seconds.

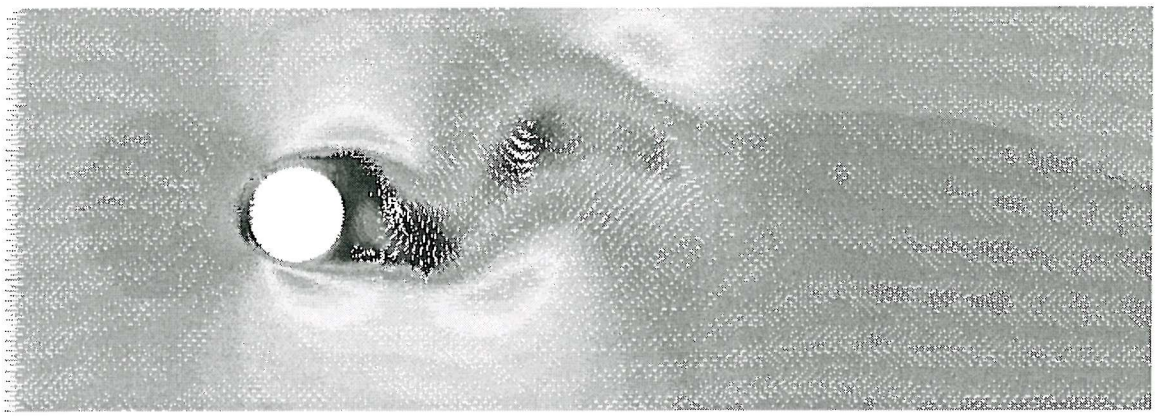

Figure 5.10: Velocity flow field for $R_e = 200$ without control at time $t = 6$ seconds in the time interval $[0, 6]$ seconds.

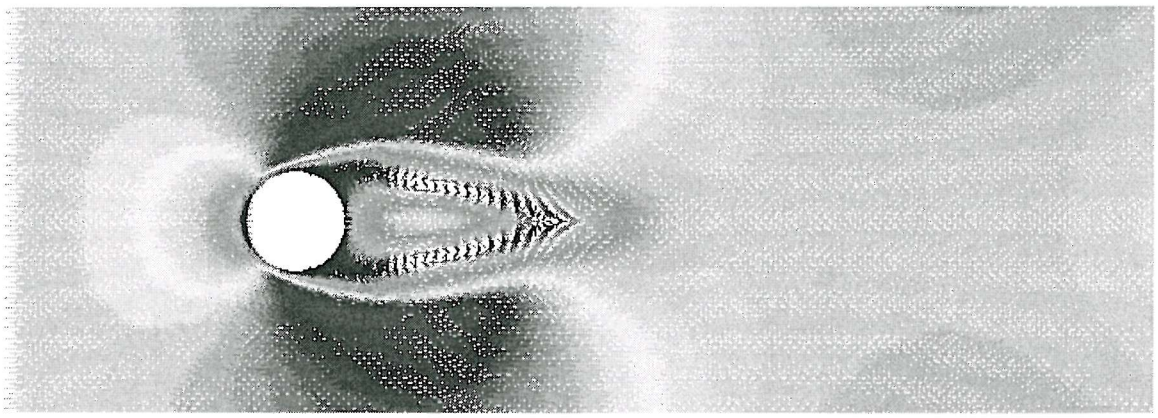

Figure 5.11: Velocity flow field for $R_e = 200$ with control at time $t = 6$ seconds in the time interval $[0, 6]$ seconds.

5.7 Results: Control Window at Steady Flow with Vortex Shedding

Preliminary findings were presented in previous section 5.6 describing a selection of trust-region algorithms interleaving reduced order models and Navier-Stokes equations to reduce the computational cost associated with controller design. This is demonstrated by suppressing Karman vortex shedding in the wake of a circular cylinder by imparting time-dependent angular velocity to the cylinder.

The promising trust region approach as discussed in section 5.6 provides an approximate reduction in the flow unsteadiness of order 50% for the time window $[0, 6]$ seconds adopted from the start of the flow. This is now tested for its applicability to suppress vortex shedding to a steady flow when control window is at the steady state of vortex shedding. Now the control time window is shifted to $[t_0, t_0 + 6]$, where t_0 is the time at the steady state of vortex shedding.

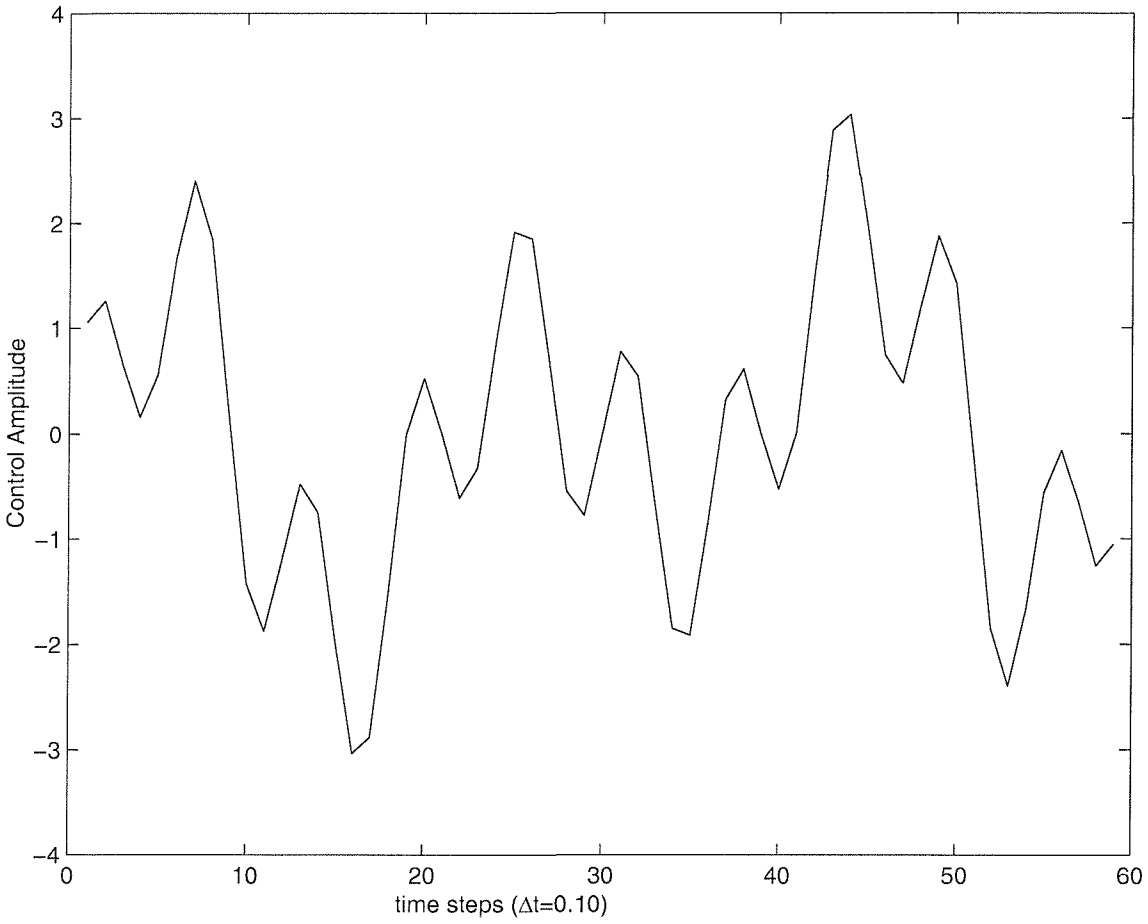

Figure 5.12: Optimal control input for $R_e = 100$ in the time-interval $[t_0, t_0 + 6]$ seconds.

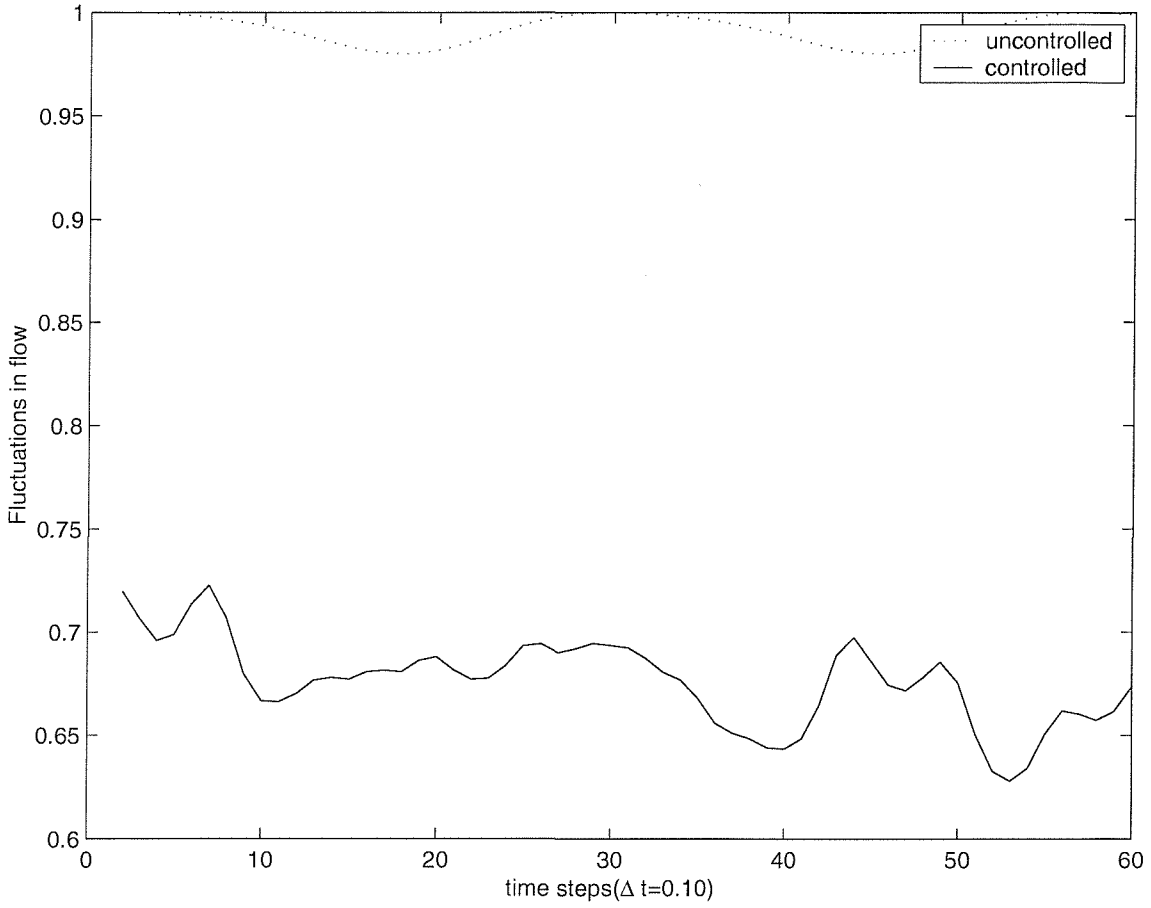

Figure 5.13: Comparison of the time history of flow fluctuations in a mean-square sense for uncontrolled and controlled cases; $R_e = 100$ within the time interval $[t_0, t_0 + 6]$ seconds only.

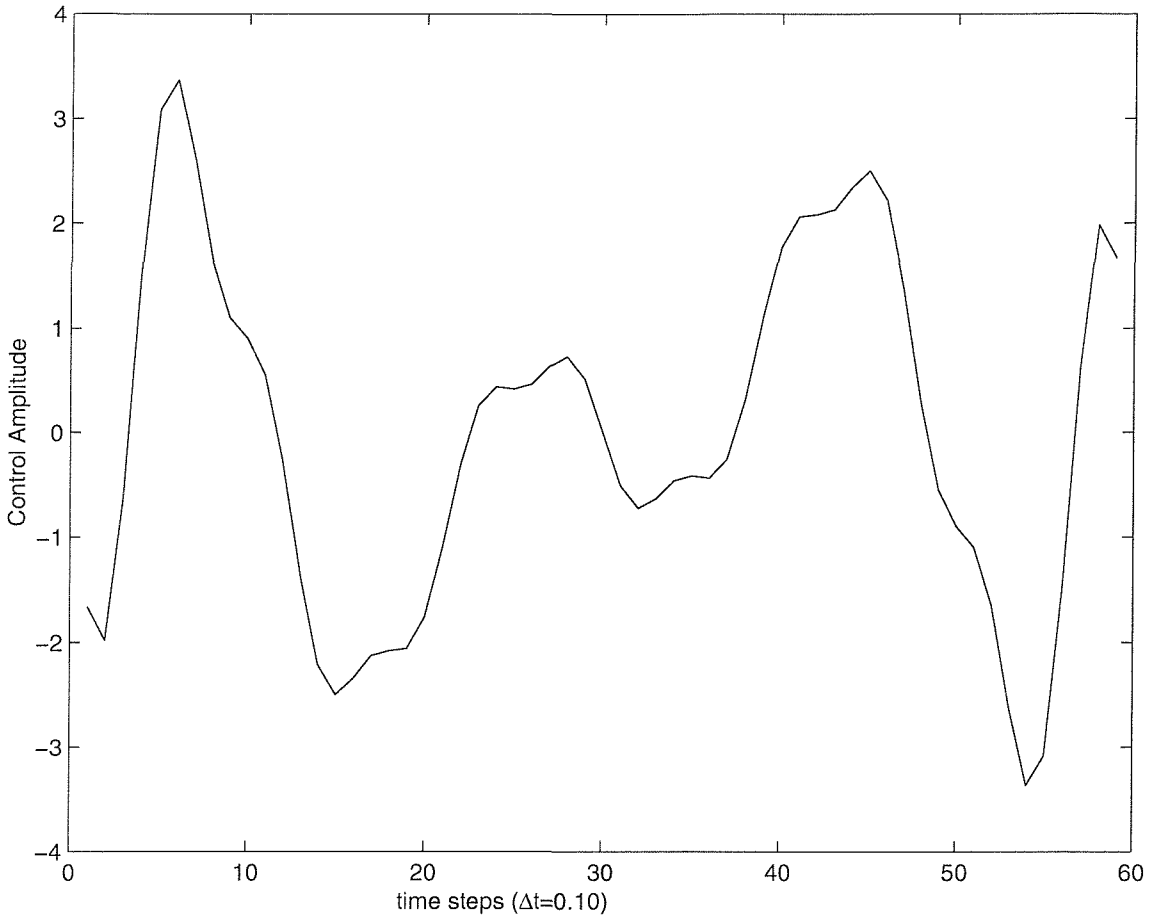

Figure 5.14: Optimal control input for $R_e = 200$ in the time-interval $[t_0, t_0 + 6]$ seconds.

The optimal control input obtained after three trust-region iterations is shown in Figures 5.12 and 5.14. The time histories of the flow field fluctuations (in a mean-square sense, i.e., the normalized least-squared difference between the current and the desired flow field) for the controlled and uncontrolled flows are compared in Figures 5.13 and 5.15) for $R_e = 100$ and $R_e = 200$ respectively.

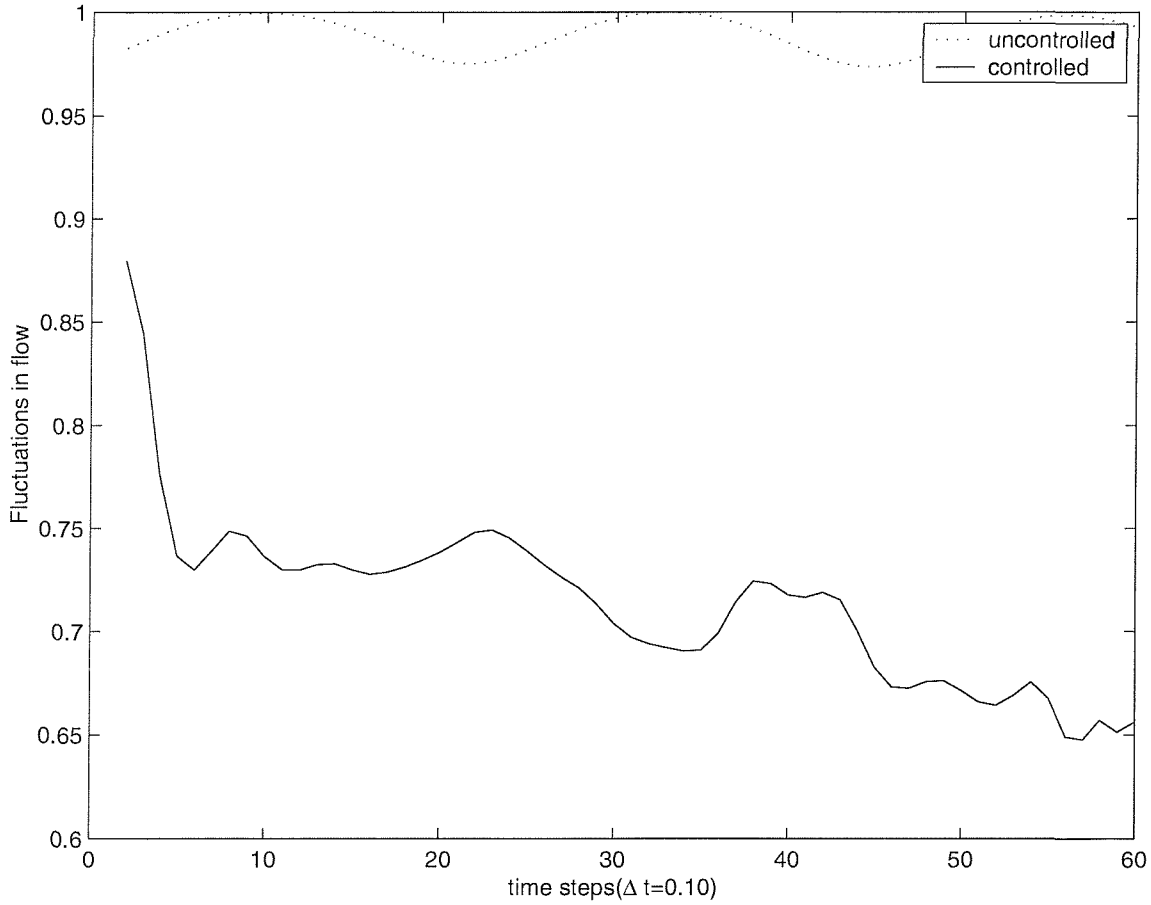

Figure 5.15: Comparison of the time history of flow fluctuations in a mean-square sense for uncontrolled and controlled cases; $R_e = 200$ within the time interval $[t_0, t_0 + 6]$ seconds only.

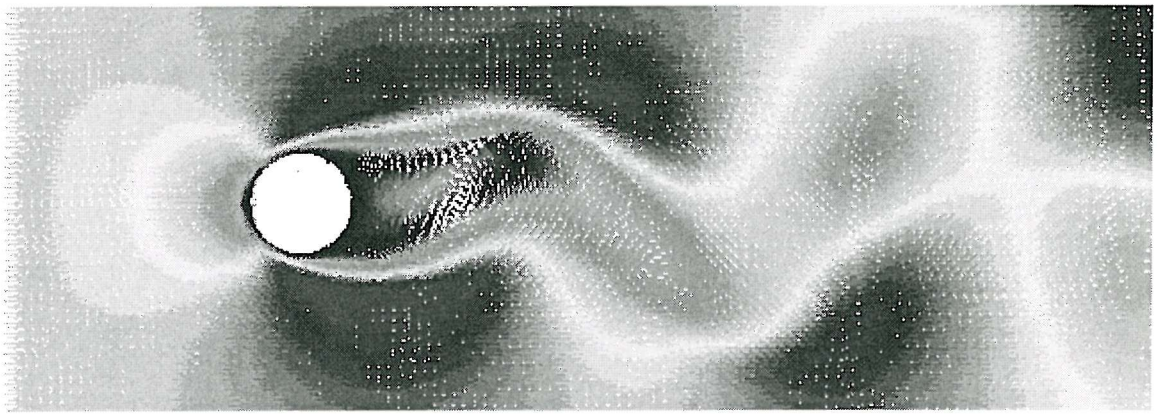

Figure 5.16: Velocity flow field at time $t = t_0 + 6$ seconds for $R_e = 100$ in the time interval $[t_0, t_0 + 6]$ seconds.

Figure 5.17: Velocity flow field at time $t = t_0 + 6$ seconds for $R_e = 100$ with control in the time interval $[t_0, t_0 + 6]$ seconds.

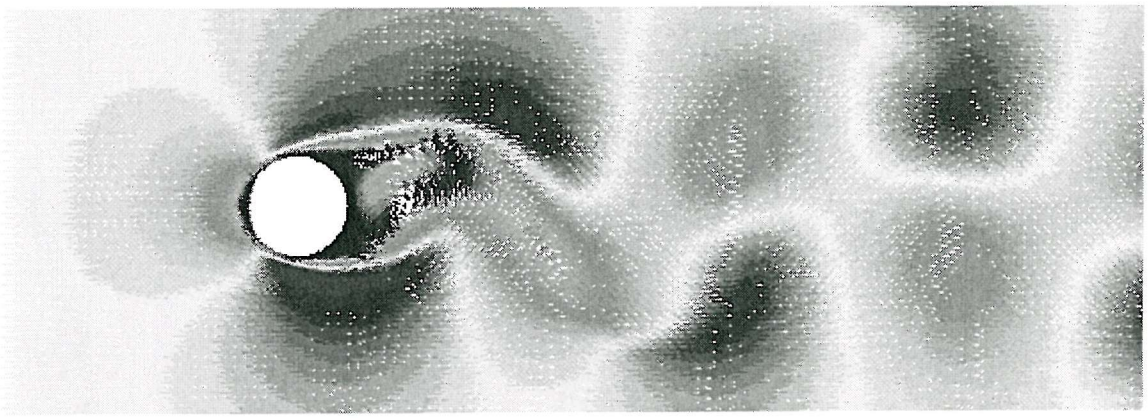

Figure 5.18: Velocity flow field at time $t = t_0 + 6$ seconds for $R_e = 200$ without control in the time interval $[t_0, t_0 + 6]$ seconds.

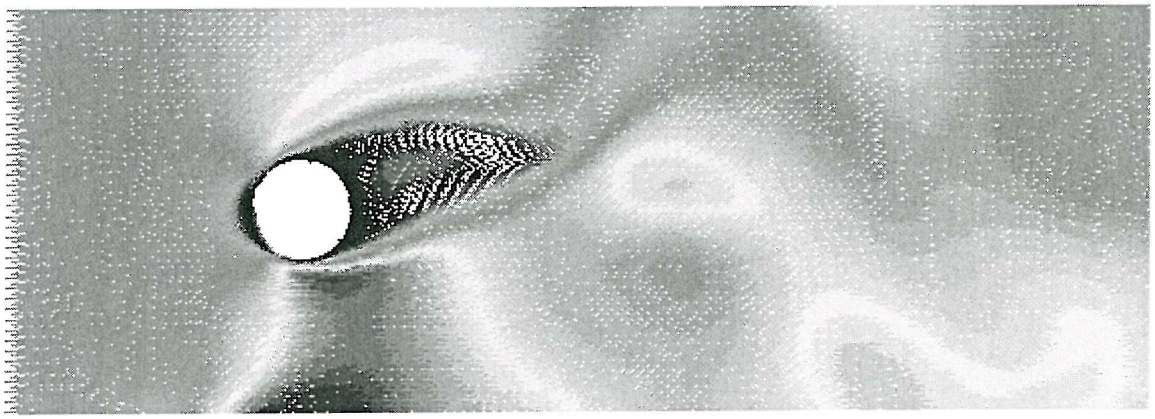

Figure 5.19: Velocity flow field at time $t = t_0 + 6$ seconds for $R_e = 200$ with control in the time interval $[t_0, t_0 + 6]$ seconds.

It is observed that in the *time window under consideration*, on average, approximately 30% reduction in the flow unsteadiness is achieved. Figures 5.16 and 5.17 for $R_e = 100$ and Figures 5.18 and 5.19 for $R_e = 200$ clearly show the infiuence of the control strategy on the flow regimes within the chosen time window. A significant reduction in unsteadiness of vortex shedding is observed with the flow tending to a steady state.

To measure the effect of the control mechanism beyond the time window under consideration, the control was switched off. Simulations showed that the control effect continued upto 3 seconds after switching off.

5.8 Controller Implementation Issues

The efficiency of flow control depends on the effective placement of sensors and actuators. For the problem of unsteady flow around the cylinder, Joseph (1998) obtained the analytical solution of an optimal distributed control and described its spatial structure presuming that one can sense everything and actuate everywhere. If it is assumed that all the modal amplitudes are derivable from the flow field measurements, then by judiciously rotating the cylinder according to the history of time dependent angular velocity the desired state of vortex suppression can be obtained. Faster responses are obtained by imposing larger control angular velocity magnitude. The actual implementation of control action may pose some difficulty because of rigorous change in magnitude of angular rotation. However, the angluar velocity presented in the thesis are of the same order of angular velocity dealt in feedback control studies of Sahjendra et al. (2001).

Figures 5.4, 5.6, 5.12 and 5.14 show the actuation required for controlling the system. The magnitude of optimum angular velocity γ obtained for the system is comparable with control studies of Sahjendra et al. (2001).

Now the problem of implementation of control is to be considered. In the current study it is presumed that the entire flow field is sensed and actuation is the applied time dependent cylinder rotation. In a real flow system it is difficult to sense the entire flow field and hence the arrangement of sensors/actuators has to be studied. Effective implementation of control strategy involves the detailed study and allocation of spatial distribution of sensors/actuators (Gillies, 1998). The assumption of entire flow field being known poses no problem in computation but if the control strategy is to be implemented in an experiment then it is unlikely that the entire flow field could be measured. The velocities at various spatial locations can be obtained by using hot-wire rakes and the work of Roussopoulos (1993) showed that the hot wires for controlling

the flow should be placed within the absolutely unstable region i.e within 5 cylinder diameter. The arrangement of hot wires as control sensors in different streamwise locations increases the range of controllable Reynolds number (Gillies, 1998). From recent studies MEMS is thought of as the solution for the problems which require an array of sensors/actuators (Gad-el Hak, 1994, 1996). The experimental works of Tokumaru & Dimotakis (1991), Fujisawa et al. (2001) describe the details of the setup and implementation. The practical implementation of rotating cylinder as a control device is seen in Jose et al. (2003) for post-stall flow control of sharp-edged wings.

5.9 Conclusions

Preliminary findings are presented describing in a selection of trust-region algorithms interleaving reduced order models and Navier-Stokes equations to reduce the computational cost associated with controller design. This is demonstrated by suppressing Karman vortex shedding in the wake of a circular cylinder by imparting time-dependent angular velocity to the cylinder. The fundamental issues involved in developing a convergent algorithm integrating reduced order models with high fidelity simulation are described, thus providing the motivation for the trust-region approach. A selection of algorithms are presented to enable efficient design of feedforward and feedback controllers to minimize a suitable cost function.

The numerical results presented in section 5.6 demonstrate a reduction in the flow unsteadiness of order 50% through adoption of a feedforward control in the time window $[0, 6]$ seconds for Reynolds number, R_e=100 and R_e=200.

The results presented in section 5.7 indicate that the strategy developed using the trust region algorithm framework can be applied to the domain close to the steady state of vortex shedding and the framework produced a reduction of around 30% in flow unsteadiness. The results obtained are comparable with the studies of He et al. (2000), Homescu et al. (2002). These results provide limited validation for the domain of applicability of the proposed approach for interleaving the full order and reduced order model in a trust region framework. The approach has shown to be viable in the domains tested and has provided results with decrease in the flow unsteadiness objective function. For the problem considered, the reduced order model is around 720 times faster than the full order solver. Hence, the application of a trust region approach to the flow control problem leads to significant savings in the computational cost. The computational cost savings are expected to become more significant when a finer grid is used to solve the full order Navier Stokes equations.

Chapter 6

Conclusions

6.1 Conclusions

The study described in this thesis has achieved the objective of vortex shedding suppression and contains a three tier structure. Firstly, the investigation has further developed and validated VCBEM through application to rotating cylinders in steady flows. Secondly, reduced order modelling techniques to construct low-order models capable of capturing the essential dynamics of flows are examined. Finally, trust-region methods integrated with reduced order models based on proper orthogonal decomposition are adopted to design feedforward and feedback controllers to achieve vortex shedding suppression.

The Viscous Cell Boundary Element Method (VCBEM) is applied as a CFD tool in Chapter 2 to investigate incompressible, uniform viscous fluid flow past two parallel cylinders of equal diameter at a critical gap spacing $g^* = 0.90$ to 1.10. In this critical flow zone an irregular interchange of in-phase and anti-phase wake flows is observed and the switching mechanism between the states is investigated. Numerical studies undertaken at space increments of 0.05, including the central case $g^* = 1.0$, detail the flow characteristics in time and space domains. Probability and power spectral analyses are presented to illustrate the statistical characteristics of the drag and lift flow parameters and vortex shedding patterns assessed through examination of their frequencies.

For parallel cylinders, with spacing $g^* = 0.95$ to 1.05, placed in a uniform viscous flow regime defined by Reynolds number $R_e = 100$ the predicted vortex patterns show dependence on the spacing factor which also relates to the interaction mechanism and vortex shedding frequency. From the evidence presented in section 2.3, for $g^* < 1.0$ the vortex wake is influenced by in-phase vortex shedding whereas for $g^* > 1.0$ anti-phase

vortex shedding is more evident. At the critical value of $g^* = 1.0$, a thorough mixing and amalgamation of vortices occurs with an intermediate Strouhal frequency value. In-phase and anti-phase vortex shedding switching is observed and a less structured wake occurs. This provides indication of a chaotic behaviour but in all cases the statistical measures reveal an ordered system.

The Viscous Cell Boundary Element Method (VCBEM) developed by Tan et al. (1999) is modified in Chapter 3 to study rotating cylinder problems. This has proved successful in reproducing the detailed flow characteristics of experimental observations, correlation with theoretical predictions produced by other methods and experimental measurements of drag and lift coefficients over a range of Reynolds number. The objective has been achieved through a primitive variable formulation of the hybrid approach involving boundary element and finite element methods. The fluid domain is idealized by an unstructured mesh and the relevant boundary conditions applicable on the rotating cylinder are incorporated into the VCBEM code with the development of suitable numerical schemes of study. The presented computed unsteady flow simulations in section 3.4 provide verification and validation of the proposed approach in lieu of other theoretical findings and experimental observations. The developed confidence in the proposed VCBEM approach after validation studies, has led to its extension to the study of twin cylinders in side-by-side and tandem arrangements as discussed in section 3.5. The time-dependent boundary conditions are implemented on the cylinder and are integrated within the VCBEM code. In the case of the side-by-side arrangement a thorough mixing of vortices and high frequency of force in counter rotation is seen as compared to a tighter wake and low frequency force oscillations in the co-rotation case. In the case of the tandem arrangement, thorough mixing of vortices occurs downstream with a diffused wake. The cylinders are attracted to each other due to an interactive suction force and high velocity of flow exists between the cylinders. The behaviour of the cylinders in counter rotation is seen in the vortex shedding patterns downstream, with a shift of the axis path of shedding. The magnitude of the forces are reduced compared to those of the co-rotation case because of the counter effect of forces between the cylinders, but they do follow the same pattern of variation when compared to the co-rotation case for the cylinders along the same axis to the flow.

A proper orthogonal decomposition (POD) method is used to investigate reduced order models (ROM) with reference to a vortex shedding wake exhibited behind circular cylinders as discussed in Chapter 4. The method is found to be very effective in deriving coherent structures of reduced order model to describe vortex shedding processes. A proper orthogonal decomposition method based control function approach

was adopted to derive the reduced order model for a rotating cylinder in a flow field. The rotation of the cylinder was considered as the forcing function and a reduced order model created. This is used to control the vortex shedding wake behind the circular cylinder and a rotation forcing function is used for the control actions in the fluid flow domain. Flow simulations and results were presented for different forcing descriptions.

The nature of covariance matrix forms the criteria for the selection of number of modes required for the reduced order model construction. For the vortex shedding problem governed by the predominant modes the covariance matrix is found to decay rapidly as described in section 4.3. In order to validate the reduced order model, a set of 60 snapshots were computed by executing the full-order code for the case $\gamma(t) = 2\sin \pi t/3$. The eigenvalues of the correlation matrix are computed using these snapshots as the database and it is seen that the first 6 modes capture 99.84 % of the flow energy. The predicted and projected basis function amplitudes are found to be in agreement. It was observed that the reduced order model agreed reasonably well with the full-order model for this particular control input.

An optimal control input can take arbitrary signal form and hence to demonstrate general applicability a reduced order model was tested for an irregular signal input. A parameterized time history of time-dependent boundary conditions is used to study the behaviour of the reduced order model to irregular signal and to test the efficacy of the reduced order model in capturing the unsteady dynamics of the system. It was observed that the reduced order model agrees reasonably well with the full-order model for this parameterized control input as discussed in section 4.8.

A framework describing the trust-region augmented variable-fidelity modelling approach to optimal flow control is presented in section 5.3. A proper orthogonal decomposition technique is adopted to derive the reduced order model of the governing Navier-Stokes equations. The present approach interleaves reduced order model and the full order governing equations in a numerical optimization procedure. The convergence to local optima can be guaranteed theoretically, by controlling the move limits of the optimization process, in the trust-region framework.

Numerical findings are presented in section 5.5 describing a selection of trust-region algorithms interleaving reduced order models and Navier-Stokes equations to reduce the computational cost associated with controller design. This is demonstrated by suppressing Karman vortex shedding in the wake of a circular cylinder by imparting time-dependent angular velocity to the cylinder. The fundamental issues involved in developing a convergent algorithm integrating reduced order models with high-fidelity simulation are described, thus providing the motivation for the trust-region approach. A selection of algorithms are presented in Chapter 5 to enable efficient design of

feedforward and feedback controllers to minimize a suitable cost function.

Numerical studies were conducted in Chapter 5 on the optimal control of flow around a rotating circular cylinder using time-dependent angular velocity as the control input. It demonstrated a reduction in the flow unsteadiness of the order of (30% - 50%), depending upon the domain of applicability of the proposed approach and the control time window being at the steady state of shedding or at the start of flow for a range of Reynolds number defining the flow regime.

6.2 Scope of Future Work

An outline of some of the directions for future research on the topics covered in this thesis is presented below.

- In the current research, the simulations were conducted for the case of $\gamma = 1$ and the results were presented. There were some high lift coefficients reported, especially high values of C_l are found for downstream cylinder in tandem arrangement. Parametric studies of γ will provide the trend of variation of C_l which assesses the performance of the model. Hence, parametric studies need to be conducted to evaluate and validate the modified VCBEM model further to multi-body configuration of cylinders to detail the flow characteristics.

- Present research dealt with twin cylinder co-rotation and counter rotation. The other combinations can be studied and parametric studies can be undertaken for twin cylinder case. Studies can then be extended by using modified VCBEM for varied combinations of co-rotation and counter rotation in multi-body configuration of cylinders.

- The model used in the current study is two-dimensional and applicable for low Reynolds number flow regime. Provision is made in the fundamental solution for the extension to 3-D. Studies can be conducted to develop, evaluate and validate the modified VCBEM model to 3-D analysis. As the dimension of the problem increases the degree of unkowns increase and hence numerical schemes should be deviced to account for the increase in memory requirements.

- The proposed trust region augmented variable fidelity approach has been applied to the flow of single cylinder at start and steady state of vortex shedding and has produced reasonable results. Studies could be undertaken to test and validate the procedure for the complex flows as in twin cylinder case and multi-body configuration of cylinders. As a step towards the extension of proposed approach,

the results of projection and prediction of the control function reduced order model are presented in Figure 6.1, for twin rotating cylinders in co-rotation for side-by-side arrangement with $\gamma = 1.0$ and Reynolds number $R_e = 100$.

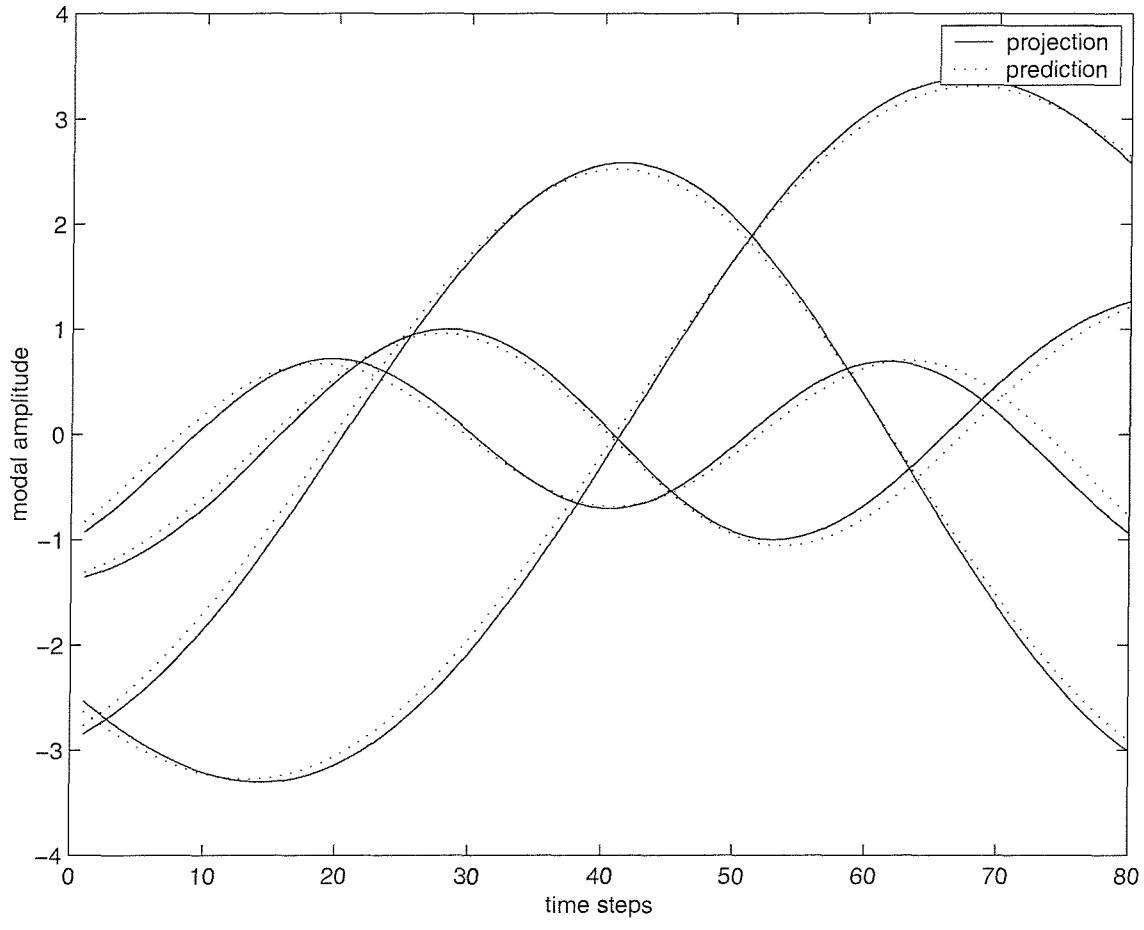

Figure 6.1: Comparison of prediction and projection of modal amplitudes for twin rotating cylinders in co-rotation for an angular velocity of $\gamma = 1.0$ and Reynolds number $R_e = 100$ in side-by-side arrangement

- The issue of how active flow control schemes can be implemented in hardware has not been addressed in the present research. When designing controllers for this class of problems, the problem of optimally placing the sensors and actuators needs to be addressed. Further, constraints may be incorporated into the optimization formulation to ensure that the controller energy requirements are kept within practical limits.

- Numerical studies could be conducted to test and validate the feedback control strategy suggested in this thesis. It is also worth noting that for ensuring the practical applicability of such feedback control schemes, it is necessary to address

the important issue of observer design. Current research assumes that one can sense everything and actuate everywhere, but in a real flow problem it is difficult to sense the entire flow field. Also, issues involving the observer design, when the flow-field measurements are available at limited spatial locations, have to be addressed and the efficacy of the observer needs to tested.

- Circular cylinders in rotation have been studied in the current research. Aspects involving rotation of bodies of different shapes and their varied combinations (i.e. cylinder and ellipse, cylinder and square, etc.) could be studied to detail fluid-structure interaction mechanism.

Bibliography

ABERGEL, F. & TEMAM, R., 1990 *On some control problems in fluid mechanics. Theoretical and Computational Fluid Dynamics* **1**, 303–325.

ALAMDARI, F., EDWARDS, S. C. & HAMMOND, S. P., 1991 *Microclimate performance of an open atrium office building: a case study in thermo-fluid modelling computational fluid dynamics for the environmental and building services engineer-tool or toy?*. 81–92. The Institute of Mechanical Engineers, London.

ALEXANDROV, N., DENNIS, J. E. & LEWIS, R. M., 1997 *A trust region framework for managing the use of approximation models in optimization. NASA/CR-1997-201745* .

ALEXANDROV, N., NEILSEN, E. J., LEWIS, R. M. & ANDERSON, W. K., 2000 *First-order model management with variable-fidelity physics applied to multi element airfoil optimization. AIAA Paper 2000-4886, Oct.* .

ARGYRIS, J. & SCHARPF, D., 1969 *Finite elements in time and space. The Aeronautical Journal of the Royal Aeronautical Society, 73:1041* .

ARIAN, E., FAHL, M. & SACHS, E. W., 2000 *Trust region proper orthogonal decomposition for flow control. NASA/cr-2000-210124, May* .

AUBRY, N., HOLMES, P., LUMLEY, L. J. & STONE, E., 1988 *The dynamics of coherent structures in the wall region of turbulent boundary layer. Journal of Fluid Mechanics* **192**, 115–173.

BABAN, F., SO, R. M. C. & OTUGEN, M. V., 1989 *Unsteady forces on circular cylinders in a cross-flow. Experimental Fluids* **7**, 293–302.

BADR, H., DENNIS, S. & YOUNG, P. J. S., 1989 *Steady and unsteady flow past a rotating circular cylinder at low Reynolds number. Computers and Fluids* **17**(4), 579–609.

BADR, H., COUNTANCEAU, M., DENNIS, S. & MENARD, C., 1990 *Unsteady flow past a rotating circular cylinder at Reynolds numbers 1000 and 10000. Journal of Fluid Mechanics* **220**, 459–484.

BAKEWELL, H. P. & LUMLEY, J. L., 1967 *Viscous sublayer and adjacent wall region in turbulent pipe flow. Physics of Fluids* **10**, 1880–1889.

BARKLA, H. M. & AUCHTERLONIE, L. J., 1971 *The Magnus or Robin effect of rotating spheres. Journal of Fluid Mechanics* **47**(3), 437–447.

BARLTROP, N. D. P. & ADAMS, A. J., 1991 *Dynamics of fixed marine structures (3rd edition).* Butterworth-Heinemann, Oxford.

BATCHELOR, G. K., 1971 *An introduction to fluid dynamics.* Cambridge University Press, Cambridge.

BEARMAN, P. W., 1984 *Vortex shedding from oscillating bluff bodies. Annual review of Fluid Mechanics* **16**, 195–222.

BEARMAN, P. W. & GRAHAM, J. M. R., 1980 *Vortex shedding from bluff bodies in oscillatory flow; a report on euromech 119. Journal of Fluid Mechanics* **99**, 225–245.

BERGGREN, P., 1998 *Numerical solution of a flow control problem: vorticity reduction by dynamic boundary action. SIAM Journal in Control and Optimization* **19**(3), 829–860.

BERKOOZ, G., HOLMES, P. & LUMLEY, J. L., 1993 *The proper orthogonal decomposition in the analysis of turbulent flows. Annual Review of Fluid Mechanics* **25**, 539–575.

BEWLEY, T., 2001 *Flow contol: New challenges for a new renaissance. Progress in aerospace science* **37**(1), 21–58.

BEWLEY, T., TEMAM, R. & ZIANE, M., 2000 *A general framework for robust control in fluid mechanics. Physica D* **138**, 360–392.

BISHOP, C. M., 1995 *Neural networks for pattern recognition.* Oxford University Press, Oxford.

BLEVINS, R. D., 1990 *Flow induced vibration.* Van Nostrand Reinhold, New York.

BOOTH, T. & BISHOP, R., 1973 *The planar motion mechanism.* Admirality Experiment Works, Haslar, UK.

BRAMLEY, R. & SAMEH, A., 1992 *Row projection methods for large nonsymmetric linear systems. SIAM Journal on Scientific and Statistical Computing* **13**(1), 168–193.

BRAMLEY, R., CHIU, K., DIWAN, S., GANNON, D., GOVINDARAJU, M., MUKHI, N., TEMKO, B. & YECHURI, M., 2000 *A component based services architecture for building distributed applications.* In *Proc. 9th IEEE International Symposium on High Performance Distributed Computing*, 283–292. IEEE, Pittsburgh, PA.

BREBBIA, C. A., 1978 *The boundary element methods for engineers.* Pentech Press, London.

BREBBIA, C. A. & WALKER, S., 1980 *The boundary element techniques in engineering.* Newness-Butterworths.

BREBBIA, C. A. & WALKER, S., 1980 *Steady and unsteady potential problems using the boundary element method.* In *Recent Advances in Numerical Methods in Fluids*, edited by Taylor, C. & Morgan, K., 105–124. Prinridge Press Ltd. UK.

BURNS, J. A. & OU, Y.-R., 1993 *Effect of rotation rate on the forces of a rotating cylinder: simulation and control. ICASE Report* 93–11.

BUSH, RICHARD, J., JAGER, M. & BERGMAN, B., 1986 *The application of computational fluid dynamics to aircraft design. AIAA paper 86-2651* .

CALAMOTE, J., 1984 *Effects de la rotation sur le sillage de cylindres tournants.* These de 3eme cycle de Universite Aix-Marseille.

CANUTO, C., HUSSAINI, M. Y., QUARTERONI, A. & ZANG, T. A., 1988 *Spectral methods in fluid dynamics.* New York, Springer-Verlag.

CHAMBERS, D. H., ADRAIN, R. J., MOIN, P., STEWART, D. S. & SUNG, H. J., 1988 *Karhunen-Loeve expansion of Burgers model of turbulence. Physics of Fluids* **31**, 2573–2582.

CHANG, K. & SONG, C., 1990 *Interactive vortex shedding from a pair of circular cylinders in a transeverse arrangement. International Journal for Numerical Methods in Fluids* **11**, 317–329.

CHARRIER, B., 1979 *Etude theorie et experimentale de leffet Magnus destine a la propulsion eolinenne de navires.* These de 3eme cycle Universite de Paris 6.

CHEN, Y., Y-R, O. & PEARLSTEIN, A., 1993 *Development of the wake behind a circular cylinder impulsively started into rotatory and rectilinear motion. Journal of Fluid Mechanics* **253**, 449–484.

CHEN, Y. G., RONG-QUAN, C., ZUO-GANG, C. & QI-XIN, S., 1999 *Solution to unsteady incompressible Navier-Stokes equation using upwind difference based on flux-difference splitting. Marine Design and Research Institute of China,* **3**, 379–392.

CHENG, L. & ARMFIELD, S. W., 1994 *Large eddy simulation of wave and current induced flow over a circular cylinder. Proceeding Boss* **94**, 655–664.

CHOU, M., 1997 *Synchronization of vortex shedding from a cylinder under rotary oscillation. Computers and Fluids* **26**(8), 755–774.

CORTELEZZI, L., 1996 *Non-linear feedback control of the wake past a suction point. Journal of Fluid Mechanics* **327**, 303–324.

COUTANCEAU, M. & MENARD, C., 1985 *Influence of rotation on the near wake development behind an impulsively started circular cylinder. Journal of Fluid Mechanics* **158**, 399–466.

DAVID, C. A., 2001 *Implicit multigrid computation of unsteady flows past cylinders of square cross-section. Computers and Fluids* **30**, 939–960.

DEANE, A. E., KEVREKIDIS, I. G., KARNIADAKIS, G. E. & ORSZAG, S. A., 1991 *Low-dimensional models for complex geometry flows: application to grooved channels and circular cylinders. Physics of Fluids A* **3**(10), 2337–2354.

DENNIS, S., NGUYEN, P. & ROCABIYIK, S., 2000 *The flow induced by a rotationally oscillating and translating circular cylinder. Journal of Fluid Mechanics* **407**, 123–144.

DETEMPLE, L. E. & ECKELMANN, H., 1989 *Phenomenology of Karman vortex streets in oscillatory flow. Experimental Fluids* **7**, 217–227.

DING, Y. & KAWAHARA, M., 2000 *Secondary instabilities of wakes of a circular cylinder using finite element method. International Journal of Computational Fluid Dynamics* **13**(3), 279–312.

DOWELL, E. H., 1980 *A simple method for converting frequency domain aerodynamics to the time domain. NASA Lewis Research Center* .

DOWELL, E. H., 1995 *Eigenmode analysis in unsteady aerodynamics: Reduced order models.* In *Proceedings of the 36th AIAA/ASME/ASCE/AHS/ASC Structures, Structural Dynamics, and Materials Conference.*, 1–13. AIAA, New Orleans, LA Washington.

DUNCAN, W. J., THOM, A. S. & YOUNG, A. D., 1970 *Mechanics of fluids.* American Elsevier Publishing Co.

DUTTO, L. C., HABASHI, W. G. & FORTIN, M., 1997 *An algebraic multilevel parallelizable preconditioner for large scale CFD problems. Computer Methods in Applied Mechanics and Engineering* **149**, 303–318.

EPUREANU, B. I., HALL, K. C. & DOWELL, E. H., 2001 *Reduced-order models of unsteady viscous flows in turbomachinery using viscous-inviscid coupling. Journal of Fluids and Structures* **15**, 255–273.

FARRANT, T., 1998 *The boundary element method applied to viscous and vortex shedding flows around cylinders.* Ph.D Thesis,University of Southampton, Southampton Uk.

FARRANT, T., TAN, M. & PRICE, W. G., 2000 *A cell boundary element method applied to laminar vortex-shedding from arrays of cylinders in various arrangements. Journal of Fluids and Structures* **14**, 375–402.

FARRANT, T., TAN, M. & PRICE, W. G., 2001 *A cell boundary element method applied to laminar vortex-shedding from circular cylinder. Computers and Fluids* **30**, 211–236.

FFOWCS WILLIAMS, J. E. & ZHAO, B. C., 1989 *The active control of vortex shedding. Journal of Fluids Structures* **3**, 115–122.

FREITAS, C. J. & RUNNELS, R., 1999 *Simulation of fluid-structure interaction using patched-overset grids. Journal of Fluids and Structures* **13**, 191–207.

FUJISAWA, N., KAWAJI, Y. & IKEMOTO, K., 2001 *Feedback control of vortex shedding from a circular cylinder by rotational oscillations. Journal of Fluid and Structures* **15**, 23–37.

GAD-EL HAK, M., 1994 *Interactive control of boundary layers: a futuristic overview. AIAA Journal* **32**, 1753–1765.

GAD-EL HAK, M., 1996 *Modern developments in flow control. Applied Mechanics Review* **49**, 365–379.

GAD-EL HAK, M., 2000 *Flow control.* Cambridge University Press.

GERRARD, J. H., 1966 *The mechanism of the formation region of vortices behind bluff bodies. Journal of Fluid Mechanics* **25**, 401–413.

GHATTAS, O. & BARK, J., 1997 *Optimal control of 2-d and 3-d incompressible Navier-Stokes flows. Journal of Computational Physics* **136**, 231–244.

GILLIES, E. A., 1998 *Low-dimensional control of circular cylindrical wake. Journal of Fluid Mechanics* **371**, 157–178.

GOPALKRISHNAN, R., TRIANTAFYLLOU, M. S., TRIANTAFYLLOU, G. S. & BARRET, D., 1994 *Active vorticity control in a shear flow using a flapping foil. Journal of Fluid Mechanics* **274**, 1–21.

GRAHAM, W. R., PERAIRE, J. & TANG, K. Y., 1999 *Optimal control of vortex shedding using low-order models. part 1 and 2. International Journal for Numerical Methods in Engineering* **44**(7), 945–990.

GREITZER, E. M., 1976 *Surge and rotating stall in axial flow compressors. part1: theoretical compression system model. ASME Journal of Engineering for Power* **98**, 190–198.

GRESHO, P., LEE, R. & SANI, R., 1980 *On the time dependent solution of the incompressible Navier-Stokes equations in two and three dimensions.* In *Recent Advances in Numerical Methods in Fluids*, edited by Taylor, C. & Morgan, K., 27–79. Prinridge Press Ltd. UK.

GRIFFIN, M. E., DIWAKER, R., ANDERSON, J. D. & JONES, E., 1978 *Computational fluid dynamics applied to flows in an internal combustion engine.* In *AIAA 16th Aerospace Sciences Meeting*, 78–57. AIAA Paper.

GUNZBURGER, M. D. & MANSERVISI, S., 1999 *The velocity tracking problem for Navier-Stokes flows with bounded distributed control. SIAM Journal of Control and Optimization* **37**, 1913–45.

HALL, K. C., 1994 *Eigenanalysis of unsteady flows about airfolis, cascades, and wings. AIAA Journal* **32**, 2426–2432.

HATTON, S. A., 1999 *Update on the design of steel catenary riser systems. In deep and ultra-deep water. Offshore Technology.* In *Society of Underwater Technology.* University of Newcastle, UK.

HE, J. W., GLOWINSKI, R., METCALFE, R., NORDLANDER, A. & PERIAUX, J., 2000 *Active control and drag optimization for flow past a circular cylinder 1: Oscillatory cylinder. Journal of Computational Physics* **163**(1), 83–117.

HENDERSON, R. D., 1995 *Details of the drag curve near the onset of vortex shedding. Physics of Fluids A* **7**(9).

HIRSCH, C., 1988 *Numerical Computation of internal and external flows.* John Wiley and Sons, Chichester, England.

HOMESCU, C., NAVON, I. M. & LI, Z., 2002 *Suppression of vortex shedding for flow around a circular cylinder using optimal control. International Journal of Numerical Methods in Fluids* **38**(1), 43–69.

HUERRE, P. & MONKEWITZ, P. A., 1990 *Local and global instabilities in spatially developing flows. Annual Review of Fluid Mechanics* **22**, 473–537.

INGHAM, D. B. & TANG, T., 1990 *A numerical investigation into the steady flow past a rotating circular cylinder at low and intermediate Reynolds number. Journal of Computational Physics* **87**(91).

JAMESON, A., SCHMIDT, W. & TURKEL, E., 1981 *Numerical solutions of the Euler equations by finite volume methods using Runge-Kutta time stepping schemes. AIAA paper 81-1259* .

JOHN, A. D. J., 1995 *Computational fluid dynamics.* McGraw-Hill Inc.

JOSE, R., PAVLOS, P. V., DEMETRI, P. T. & MATTHEW, D. Z., 2003 *Post-Stall flow control of sharp-edged wings via unsteady blowing. AIAA paper 2003-62* .

JOSEPH, L., 1998 *Optimal control of unsteady stokes flow around acylinder and the sensor/actuator placement problem. NASA CR 1998-207680* .

JOSESH, K. & ALLEN, P., 2001 *Low-Speed aerodynamics.* Cambridge University Press.

KARHUNEN, K., 1946 *Zur Spektral Theorie Stochasticer Prozesse. Ann. Acad. Sci. Fennicae SIAM (review)* **34**(4), 561–580.

KARNIADAKIS, G. E. & TRIANTAFYLLOU, G. S., 1989 *Frequency selection and asymptotic states in laminar wakes. Journal of Fluid Mechanics* **199**, 441–454.

KESSELMANN, C., 1999 *The Grid: Blueprint for a New Computing Infrastructure.* Morgan Kaufmann Publishers USA.

KIRBY, M. & SIROVICH, L., 1990 *Application of the Karhunen-Loeve procedure for characterization of human faces. IEEE Transactions on Pattern Analysis and Machine Intelligence* **12**(1), 103–108.

KOCH, W., 1985 *Local instability characteristics and frequency determination of self-excited wake flows. Journal of Sound and Vibration* **58**, 11–29.

KOCH, W., 1986 *Direct resonances in Orr-Sommerfeld problems.. Acta Mechanica* **58**, 11–29.

KOTHARI, A. P. & ANDERSON JR, J. D., 1985 *Flows over Reynolds number airfoils-compressible Navier-Stokes numerical solutions. AIAA paper 85-0107* .

LEWIT, M., 1992 *Active control of dipole sound from cylinders.* In *Proc. DAGA*, 421–431. DAGA, Berlin.

LI, J., CHAMBAREL, A., DONNEAUD, M. & MARTIN, R., 1991 *Numerical study of laminar flow past one and two cylinders. Computers and Fluids* **19**(2), 155–170.

LIN, J. C., 1996 *Controlled motion of a cylinder through a free surface; effect of depth of penetration. Journal of Fluids and Structures* **10**, 309–317.

LINGG, G. P. & SHIH, T. M., 1999 *Numerical study on the vortex motion patterns around a rotating cylinder and their critical characters. International Journal for Numerical Methods in Fluids* **29**, 229–248.

LIU, Z. C., ADRIAN, R. J. & HANRATTY, P., 1994 *Reynolds number similarity of orthogonal decomposition of the outer layer of turbulent wall flow. Physics of Fluids* **6**, 2815–2819.

LOEVE, M., 1945 *Functiona aleatoire de second ordre. Compte Rend. Acad. Sci., Paris* p. 220.

LUMLEY, J. L., 1967 *The structure of inhomogenous turbulence.* In *Atmospheric Turbulence and Radio wave Propagation*, edited by A.M.Yaglom & V.I.Tatarski, 166–178. Nauka, Moscow.

LUMLEY, J. L., 1971 *Stochastic tools in turbulence.* Academic Press, New York.

MAHAJAN, A. J., DOWELL, E. H. & BLISS, D. B., 1991 *Eigenvalue calculation procedure for Euler/Navier-Stokes solvers with application to flows over airfolis. Journal of Computational Physics* **97**, 398–413.

MAHIR, N. & ROCKWELL, D., 1996 *Vortex formation from a forced system of two cylinders. Part-2 side-by-side arrangement. Journal of Fluids and Structures* **10**, 491–500.

MAIR, W. A. & MAULL, D. J., 1971 *Bluff bodies and vortex shedding - a report on Euro-Mech 17. Journal of Fluid Mechanics* **45**, 209–224.

MAMPAEY, F. & XU, Z. A., 1992 *An experimental and simulation study of a mould filling combined with heat transfer.* In *Computational Fluid Dynamics*, 421–428. Elsevier, Amsterdam.

MATSUNAGA, K., MIJATA, H ANDAOKI, K. & ZHU, M., 1992 *Finite-Difference simulation of 3D vortical flows past road vehicles.* Vehicle Aerodynamics, SAE special Publication 908.

MEIJERINK, J. A. & VAN DER VORST, H. A., 1977 *An iterative solution method for linear systems of which the coefficient matrix is a symmetric M-matrix. Mathematics of Computation* **31**, 148–162.

MITTAL, S., 2001 *Control of flow past bluff bodies using rotating control cylinders. Journal of Fluids and Structures* **15**, 291–326.

MITTAL, S., KUMAR, V. & RAGHUVANSHI, A., 1991 *Unsteady incompressible flow past two cylinders in tandem and staggered arrangements. International Journal of Numerical Methods in Fluids* **25**, 1315–1344.

MODI, V. J., MOKHTARIAN, F. & YOKOMIZO, T., 1990 *Effect of moving surfaces on the airfoil boundary-layer control. Journal of Aircraft* **27**, 42–50.

MOIN, P. & BEWLEY, T., 1994 *Feedback control of turbulence. Applied Mechanics Review* **47**, 3–13.

MONKEWITZ, P. A., 1989 *Feedback control of global oscillations in fluid systems. AIAA paper 89-0991* .

MORISON, J., O'BRIEN, M., JOHNSON, J. & SCHAAF, S., 1950 *The force excerted by surface waves on piles. Petroleum Transcations* **189**, 149–154.

NAIR, M. T., SENGUPTA TAPAN, K. & CHAUHAN UMENDRA, S., 1998 *Flow past rotating cylinders at high Reynolds numbers using higher order upwind scheme. Computers and Fluids* **27**(1), 47–70.

NG, C. W. & KO, N. W. M., 1995 *Flow interaction behind two circular cylinders of equal diameter - a numerical study. Journal of Wind Engineering and Industrial Aerodynamics* **54/55**, 277–287.

NOOR, A. K., 1994 *Recent advances and applications of reduction methods. Applied Mechanics Reviews* **47**, 125–145.

ORTEL, J. H., 1990 *Wakes behind blunt bodies. Annual Review of Fluid Mechanics* **22**, 539–564.

OU, Y.-R., 1996 *Mathematical modelling and numerical simulation in external flow control.* In *Flow control*, edited by Gunzburger, M., 218–253. Springer-Verlag.

PARK, C.-W. & LEE, S.-J., 2000 *Free end effects on the near wake flow structure behind a finite circular cylinder. Journal of Wind Engineering* **88**, 231–246.

PARK, D. S., LADD, D. M. & HENDRICKS, E. W., 1992 *Feedback control of Karman vortex shedding.* In *Symposium on Active Control of Noise and Vibration.* ASME, Anaheim CA.

PARK, D. S., LADD, D. M. & HENDRICKS, E. W., 1994 *Feedback control of Karman vortex shedding behind a cylinder at low Reynolds numbers. Physics of Fluids* **6**, 2390–2405.

PERSILLON, H., BRAZA, M. & JIN, G., 1995 *Prediction of transition features in the flow past a circular cylinder in three-dimensions.* In *Proceedings of 5th International Offshore and Polar Engineering Conference*, 597–602. International Society of Offshore and Polar Engineers.

PETERSON, L. D. & CRAWLEY, E. F., 1988 *Improved exponential time series approximation of unsteady aerodynamic operators. Journal of Aircraft* **25**, 121–127.

POHLEN, L. J. & MUELLER, T. J., 1986 *Boundary layer characteristics of the Miley Airfoil at low Reynolds numbers. Journal of Aircraft* **21**(9), 658–664.

PRANDTL, L. & TIETJENS, O. G., 1934 *Applied hydro and aeromechanics, Translated by Den Hartog, J P in 1957.* Dover, New York.

PREISENDORFER, R., 1988 *Principal component analysis in meteorology and oceanography.* Elsevier, Amsterdam.

RAVI, A. B., NAIR, P. B., TAN, M. & PRICE, W. G., 2002 *Optimal feedforward and feedback control of vortex shedding using trust region algorithms.* In *AIAA First Flow Conference AIAA-2002-3076*. AIAA, Missiouri.

RAVI, A. B., TAN, M. & PRICE, W. G., Under review *An analysis of a two cylinder-fluid interaction at critical gap spacing by a cell boundary element method. Journal of Fluids and Structures* .

RAVINDRAN, S. S., 1999 *Proper orthogonal decomposition in optimal control of fluids. NASA TM 1999-209113* .

RAVINDRAN, S. S. & ITO, K., 1998 *A reduced order method for simulation and control of fluid flows. Journal of Computational Physics* **143**(2), 403–425.

RICHARDS, R. J., 1979 *An Introduction to dynamics and control.* Longman group limited, London.

ROBINSON, S. K., 1991 *Coherent motions in the turbulent boundary layer. Annual Review of Fluid Mechanics* **23**, 601–639.

ROCKWELL, D., 1998 *Vortex-body intercations. Annual Review of Fluid Mechanics* **30**, 199–229.

RODRIGUEZ, J. F., RENAUD, J. E. & WATSON, L. T., 1998 *Convergence of trust region augmented Lagrangian methods using variable fidelity approximation data. Structural Optimization* **15**(3-4), 141–156.

ROMANOWSKI, M. C., 1996 *Reduced order unsteady aerodynamic and aeroelastic models using Karhunen-Loeve eigenmodes.* In *Proceedings of the Sixth Symposium on Multidisciplinary Analysis and Optimization paper 96-3981*. AIAA, Bellevue, WA.

ROUSE, HUNTER & INCE, S., 1957 *History of hydraulics*. Iowa Institute of Hydraulic Research Iowa.

ROUSSOPOULOS, K., 1993 *Feedback control of vortex shedding at low Reynolds number. Journal of Fluid Mechanics* **248**, 267–296.

SAHJENDRA, N. S., JAMES, H. M., GREOGRY, A. A., SIVA, B. & JAMES, K. H., 2001 *Optimal feedback control of vortex shedding using proper orthogonal decomposition models. Jouranl of fluid engineering* **123**, 612–618.

SAINSBURY, P. & KING, D., 1971 *The flow induced oscillations of marine structures. Proc. Institution of Civil Engineers* **49**, 269–302.

SARPKAYA, T. & ISAACSON, M., 1990 *Mechanics of wave forces on offshore structures*. Van Nostrand Reinhold, New York.

SAYERS, A. T., 1979 *Lift coefficient and flow visualization on a leading edge rotating cylinder rudder. International Journal of Mechanical and Electrical Engineering* **7**(75).

SCHLICTHING, H., 1932 *Concerning the orgin of turbulence in a rotating cylinder. Math.-Phys.* **2**, 160–198.

SHAW, C. T., 1988 *Predicting vehicle aerodynamics using computational fluid dynamics- a users perspective. Research in Automotive Aerodynamics, SAE special Publication 747* 119–132.

SHAW, S. W. & PIERRE, C., 1993 *Normal modes of vibration for non-linear vibratory systems. Journal of Sound and Vibration* **164**, 85–124.

SHAW, S. W. & PIERRE, C., 1994 *Normal modes of vibration for non-linear continuous systems. Journal of Sound and Vibration* **169**, 319–347.

SIROVICH, L., 1987 *Turbulence and the dynamics of coherent structures parts 1-3. Quarterly of Applied Mathematics Oct.* **45**(3), 561–590.

SRITHARAN, S., 1992 *An optimal control problem in exterior hydrodynamics. Proceedings of the Royal Society of Edinburgh* **121**(A), 5–32.

SRITHARAN, S., OU, Y.-R., PARK, D. S., LADD, D. M. & HENDRICKS, E. W., 1996 *Optimal control of viscous flow past a cylinder: mathematical theory, computation and experiment Parts 1-2. Actual problems of aviation and aerospace systems. Russ-Am Sci J* **1-2**, (5–15)–(7–18).

STEGER, J. L., DOUGHERTY, F. C. & BENEK, J. A., 1983 *A chimera grid scheme. Advances in grid generation, FED ASME, New York* **15**, 39–48.

STEIJSIGER, C., LANKHORST, A. M. & ROMAN, Y. R., 1992 *Influence of gas phase reactions on the deposition rate of silicon carbide from the precursors methyltrichlorosilane and hydrogen. Numerical Methods in Engineering, Amsterdam* 857–864.

STIEFEL, E. L., 1963 *An introduction to numerical mathematics.* Academic Press.

STOCKS, N. G., SHAW, C. T. & KING, G. P., 1996 *Dynamical characterization of the spatio-temporal structures of a bluff body. Journal of Fluids and Structures* **10**, 491–500.

STONE, E. & CUTLER, A., 1996 *Introduction to archetypal analysis of spatio-temporal dynamics. Physica D* **96**, 110–131.

SUYKENS, J. A. K., VANDEWALLE, J. P. L. & DE MOOR, B. L. R., 1995 *Artificial Neural networks for Modelling and Control of Non-Linear Systems.* Kluwer Academic Publishers, Boston.

SWANSON, W. M., 1961 *The magnus effect: a summary of investigation to date. Transaction ASME D: Journal of Basic Engineering* 461–470.

SZEPESSY, S. & BEARMAN, P. W., 1992 *Aspect ratio and end plate effects on vortex shedding from a circular cylinder. Journal of Fluid Mechanics* **234**, 191–217.

TAN, M., FARRANT, T. & PRICE, W. G., 1999 *A cell boundary element method for viscous laminar flow solutions. Proceedings of Royal Society of London* **A**(455), 4277–4304.

TAN, M., UZUNOGLU, B., PRICE, W. G. & ROGERS, E., 2000 *Reduced models for statistically stationary and nonstationary flows. AIAA paper No. 2000-2558* .

TANG, T. & INGHAM, D. B., 1991 *On steady flow past a rotating circular cylinder at Reynolds numbers 60 and 100. Computers and Fluids* **19**(2), 217–230.

TENNANT, J. S., JOHNSON, W. S. & KROTHAPALLI, A., 1976 *Rotating cylinder for circulation control on an airfoil. Journal of Hydronautics* **10**, 102–105.

TOKATY, G. A. & FOULIS, G. T., 1971 *A history and philosophy of fluid mechanics.* Henley-on-Thames, England.

TOKUMARU, T. & DIMOTAKIS, P., 1991 *Rotary oscillation control of a cylinder wake. Journal of Fluid Mechanics* **224**, 77–90.

TOORMAN, E. A. & BERLAMONT, J. E., 1992 *Free surface flow of a dense natural cohesive sediment suspension.* In *Computational Fluid Dynamics*, 1005–1011. Elsevier, Amsterdam.

TOSAKA, N. & KAKUDA, K., 1988 *The generalised BEM for nonlinear problems.* In *Boundary Elements X. Proceedings of the 10th International Conference Boundary Element Methods.* Computational Mechanics Publications, Southampton.

TOWNSEND, A. A., 1961 *Equilibrium layers and wall turbulence. Journal of Fluid Mechanics* **11**, 97–120.

TOWNSEND, A. A., 1970 *Entrainment and the structure of turbulent flow. Journal of Fluid Mechanics* **41**, 13–46.

TRITTON, D. J., 1960 *Experiments on the flow past a circular cylinder at low Reyonlds number. Journal of Fluid Mechanics* **6**, 547–567.

UDEA, T. & DOWELL, E. H., 1984 *Flutter analysis using nonlinear aerodynamic forces. Journal of Aircraft* **21**, 101–109.

UZUNOGLU, B., TAN, M. & PRICE, W. G., 2001 *Low Reynolds number flow around an oscillating circular cylinder using a viscous cell boundary element method. International Journal of Numerical Methods in Engineering* **50**, 2317–2338.

VAN DE VOSSE, F., SEGAL, A., VAN STEENHOVEN, A. A. & JANSEEN, J., 1986 *A finite element approximation of the unsteady two dimensional Navier-Stokes equations. International Journal of Numerical Methods in Fluids* **6**, 427–443.

VERSTEEG, H. K. & MALALASEKERA, W., 1998 *An introduction to computational fluid dynamics The finite volume method.* Longman, England.

WHITEHEAD, D. S., 1959 *The vibration of cascade blades treated by actuator disk methods. Proceedings of the Institution of Mechanical Engineers* **173**, 555–563.

WILLIAMSON, C. H. K., 1985 *Evolution of a single wake behind a pair of bluff bodies. Journal of Fluid Mechanics* **155**, 141–174.

WILLIAMSON, C. H. K., 1991 *2-D and 3-D aspects of the wake of a cylinder, and their realtion to wake computations. Lectures in Applied Mathematics* **28**, 719–751.

WILLIAMSON, C. H. K., 1996 *Vortex dynamics in the cylinder wake. Annual Review of Fluid Mechanics* **28**, 477–539.

ZHANG, H. & ZHANG, X., 1997 *Flow structure analysis around an oscillating circular cylinder at low KC number; a numerical study. Computers and Fluids* **26**, 83–106.

ZHIJIN, L., NAVON, I. M., HUSSAINI, M. Y. & LE DIMET, F.-X., 2002 *Optimal control of cylinder wakes via suction and blowing (to appear). Computers and Fluids*

.

ZHOU, C. Y. & GRAHAM, J. M. R., 2000 *A numerical study of cylinders in waves and currents. Journal of Fluids and Structures* **14**, 403–428.

ZHU, C., BYRD, R. H., LU, P. & NOCEDAL, J., 1997 *Algorithm 778: L-BFGS-B, fortran routines for large scale bound constrained optimization. ACM Transactions on Mathematical Software* **23**(4), 550–560.

ZIENKIEWICZ, O. C., 1977 *The Finite Element Method.* McGraw-Hill, London.

ZIENKIEWICZ, O. C. & MORGAN, K., 1982 *Finite elements and approximation.* Wiley.

ZIENKIEWICZ, O. C., SZMELTER, J. & PERAIRE, J., 1990 *Compressible and incompressible flow; an algorithum for all seasons. Computer Methods in Applied Mechanics and Engineering* **78**, 105–121.